OPG's DEEP GEOLOGIC

REPOSITORY

FOR LOW & INTERMEDIATE LEVEL WASTE

Supporting Technical Report

Phase I Long Term Climate Change Study

November 30, 2008

Prepared by:
W.R. Peltier
Department of Physics
University of Toronto

OPG 00216-REP-01300-00004-R00

OPG'S DEEP GEOLOGIC

REPOSITORY

FOR LOW & INTERMEDIATE LEVEL WASTE

Supporting Technical Report

Phase I Long Term Climate Change Study

November 30, 2008

Prepared by:
W.R. Peltier
Department of Physics
University of Toronto

OPG 00216-REP-01300-00004-R00

DOCUMENT HISTORY

Title:	Phase I Long-Term Climate Change Study	
Subtitle:	OPG's Deep Geological Repository for Low and Intermediate Level Waste	
Client:	Ontario Power Generation Inc.	
Document Number:	OPG 00216-REP-01300-00004-R00	
Revision Number:	0	**Date:** November 30, 2008
Prepared by:	W.R. Peltier	

Approved by: Robert Leech **Accepted by:** Mark Jensen

EXECUTIVE SUMMARY

Impacts upon a Canadian repository for Low and Intermediate Level Waste (L&ILW) due to long timescale changes in the climate of the Earth should take into account the possibility that the Canadian landscape could be subjected to a further glaciation event similar to those that have recurred over the past million years of Earth history. Although the current and increasing inventory of radiatively active trace gases in the atmosphere may make such an event unlikely in the immediate future (next few centuries), because a proposed repository must remain secure for timescales in excess of 10^5 years, the possibility of such a further occurrence cannot be excluded. This Supporting Technical Report was prepared as part of Phase I DGR Geosynthesis activities to derive a design basis glaciation scenario as relevant to understanding groundwater system evolution and the future performance of the proposed Deep Geologic Repository for Low and Intermediate Level Radioactive Waste within the Paleozoic sedimentary sequence beneath Bruce site, near Tiverton, Ontario.

In this Report a review is first provided of what is currently known concerning the geologically recent history of Long Term Climate Change as background to the detailed analysis of the conditions that would be expected to develop at and below the surface of the Earth if the Canadian land mass were to be reglaciated. As a model of such a reglaciation event we employ the results delivered by an appropriately calibrated model of the most recent of such events that occurred in the Late Quaternary period of Earth history. The physical model employed for the purpose of this analysis is the University of Toronto Glacial Systems Model (UofT GSM), a model that has been exercised in a wide range of peer reviewed publications in the open scientific literature and which may be assumed to define the current state-of-the-art in this field of science.

The analyses that have been performed using this model for the purpose of contributing to the development of the required future glacial event predictions are explicitly based upon the fact that it is impossible to provide a unique description of the detailed characteristics of such an event. Rather the perspective adopted is based upon the use of Bayesian methods to examine the range of models that would be compatible with the constraints that can be brought to bear upon the detailed characteristics of the most recent North American glaciation event of the Late Quaternary ice-age. It is thereby shown that the spread of model characteristics is rather broad, sufficiently broad, it is believed, to encompass the characteristics of any similar event that could occur in the future.

The numerous characteristics of the glaciation process that are relevant to the understanding of repository performance include both mechanical properties such as the time dependence of the thickness of glacial ice that could develop over the site and the normal stress regime associated with the weight of this load. Similarly relevant is the evolution of the temperature at the base of the ice-sheet, a characteristic of the glaciation process that turns out to be somewhat counterintuitive as times of thickest ice-cover are associated with the warmest basal temperatures, a consequence of the degree of thermal insulation provided by thick ice and the continuing flow of heat from the Earth's interior into the ice-sheet base. The sub-surface thermal regime is also important to repository performance, in particular the depth to which frozen ground (permafrost) may extend when the surface temperature is below freezing. This issue is important not only in the regions that are episodically ice-covered but also in exterior regions where the influence of permafrost may be even more extreme. In regions within which the base of the ice-sheet is temperate, i.e. having temperatures above the freezing point, meltwater is continually generated by the outflow of geothermal heat and the rate of such generation is crucial to understanding the extent to which such meltwater may be forced to infiltrate into the subsurface and thus impact sub-surface hydrology.

The Report therefore also includes a Bayesian analysis of the basal rates of meltwater production as well as detailed results on the filling of any proglacial lakes that would be expected to develop at the hypothetical repository site, especially during the process of deglaciation during which the rate of freshwater production is increased. The final data set provided from this Bayesian analysis of the expected impacts of long term climate change upon a repository for L&ILW involves the time dependence of the depression and uplift of the crust at the location of the hypothetical site. Such vertical motions are due to the process of glacial isostatic adjustment (GIA) that involves the visco-elastic response of the Earth to the time-dependent surface mass load associated with the glaciation and deglaciation process.

It is expected that the range of plausible models derived on the basis of the Bayesian methodology is sufficiently broad to encompass the conditions that would be expected at any location in this general region. Because southern Ontario is located near what was the southern edge of the Laurentide ice-sheet during its sequence of Late Quaternary expansions, it is a region of strong temporal variability in the above described characteristics of the glaciation process. An important message that is contained in this Report concerns the importance of incorporating this fact into the analysis of the prediction of future glaciation events at the proposed repository site.

CONTENTS

LIST OF TABLES

LIST OF FIGURES

APPENDICES

Appendix A: Continental scale maps of the evolution of several properties of the glaciation process for models 9921 and 9930. These properties include (Appendix A1) ice thickness, (Appendix A2) basal temperature, (Appendix A3) permafrost depth and (Appendix A4) crustal deflection due to the glacial isostatic adjustment process.

Appendix B: A CD archive of the time series discussed in Report Section 4.3.

1. INTRODUCTION

In assessing the safety case for a repository for low and intermediate level waste (L&ILW) to be excavated at any site within the territory of Canada, one is obliged to face the fact that this northern portion of the North American continent has been subjected to a series of intense continental scale glaciation and deglaciation events over the past million years of Earth history. This process has been characterized by a dominant timescale of 100,000 years and is understood to have occurred in response to small amplitude changes in the effective intensity of the Sun due to variations in the geometry of Earth's orbit around the Sun. These variations in orbital geometry are caused in turn by the gravitational attraction of the Earth by the other planets in this solar system. At each of the maxima of North American ice-sheet extent, the thickness of glacial ice over Canada has approached 4 km in the most heavily glaciated regions and the southern boundary of ice-sheet extent has been located near the current US-Canada border except in the south-eastern-most sector where ice-cover has extended well south of the Great Lakes and into upstate New York.

Over Southern Ontario, maximum ice-thicknesses would have exceeded 2.5 km during the time of most southerly ice-sheet advance. For the purpose of assessment of future glaciation events on a repository for L&ILW in this region, it is important to understand past time dependent conditions in this region during the Late Quaternary glacial events. This is a consequence of the fact that each 100,000 year glacial cycle includes multiple episodes of local advance and retreat. Since Ontario is located near the southern margin of glacial extent, it is a region of particularly intense variability. Since this variability has the potential to severely impact the sub-surface hydrological regime, it is important that adequate attention be paid to the development of an understanding of the degree of non-uniqueness that must be associated with any attempt to characterize the boundary conditions that such a repository would be subjected to in the event that a future episode of glaciation should occur.

This Report is based upon the application of a model of continental scale glaciation events that have occurred in response to changes in the effective strength of the Sun due to changing orbital geometry. The model is referred to in the open scientific literature as the University of Toronto Glacial Systems Model (UofT GSM) and has been under continuous development for the past two decades. It is employed herein to develop a description of a re-glaciation of the North American continent as a means of assessing the impact that such an event could have upon repository performance. The model employed for this purpose is unique in the research literature of this field for several reasons, the most important of which for present purposes is that it is equipped with the numerical apparatus required to calibrate it against a wide range of observational constraints using a statistically powerful Bayesian methodology. This model has its origins in the early work of Hyde and Peltier (1985), Deblonde and Peltier (1991, 1993), Deblonde et al. (1993) and Tarasov and Peltier (1997, 1999). The most recent developments of this structure, as described in Tarasov and Peltier (2006, 2007), are highly relevant to the applications to be described in this Report, especially that by Tarasov and Peltier (2007) in which a detailed discussion of improvement to the methods employed to compute the evolution of permafrost extent and depth during a glacial cycle is provided.

In the main body of this Report to follow, Section 2.1 provides a background discussion of current understanding of long term climate change, a discussion that focuses upon the most recent million years of Earth history. In Section 2.2, the issue of the mechanism of glacial inception is then discussed in which the focus is upon the interplay between the primary orbital mechanism and the way in which this mechanism may be abetted or impeded by variations in

the concentrations of atmospheric greenhouse gases. Section 2.3 provides a brief discussion of expectations of climate change over the next century based upon the recently published AR4 Report of the Intergovernmental Panel on Climate Change. In Section 3, the currently most advanced configuration of the UofT GSM is described. Section 3.1 provides an overview of the model while Section 3.2 focuses upon the most recent advance in the manner in which predictions of permafrost extent and depth are produced. This section ends with a description of the Bayesian calibration procedure that is employed to characterize the degree of non-uniqueness of model predictions. Section 4 presents the primary new results of this study of long timescale climate change on repository performance. Section 4.1 discusses the criteria on the basis of which a sub-set of model predictions has been selected as a basis for the analysis of uniqueness. Section 4.2 discusses this subset of the complete ensemble of model results from a continental scale perspective whereas Section 4.3 presents the time series for the site that has been selected for analysis in this Report. The conclusions of the Report are summarized in Section 5. Time series data for the repository location are provided on a CD that is included in Appendix B.

2. LONG TERM CLIMATE CHANGE: A REVIEW OF THE CURRENT STATE OF UNDERSTANDING

One of the most dramatic advances in Earth scientific research during the past three decades has occurred as a consequence of the application of new methods to the understanding of isotopic and trace gas data collected from deep sea sedimentary cores from the ocean basins and deep ice-cores from the ice-sheets on Greenland and Antarctica, respectively. This research has enabled the discovery of the ultimate cause of the Late Quaternary ice-ages and thereby demonstrated the highly non-linear nature of the planet's climate system. These advances are briefly reviewed in what follows in order to set the stage for a discussion of ice-age influences upon repository performance.

2.1 Late Quaternary Climate History

Over the past million years of Earth history, climate variability has been dominated by the cyclic expansion of northern hemisphere land ice cover. The evidence of this process is most clearly visible in isotopic data from deep sea sedimentary cores raised from the floors of all ocean basins from locations where the sedimentation rate is sufficiently high and not subjected to disturbance by turbidity current and other effects. Mass spectrometric measurements of the down-core relative concentrations of $^{16}0$ and $^{18}0$ on the tests of foraminifera provide a high quality proxy, referred to as $\delta^{18}0$, for the amount of land ice that existed on the continents (e.g., Shackleton, 1967) at the time in the past, represented by the depth in the core, at which the measurement is made. This quantity is defined as:

$$\delta^{18}0 = \left[\frac{\left[{}^{18}0/{}^{16}0\right]}{\left[{}^{18}0/{}^{16}0\right]_{stnd}} - 1 \right] , \qquad (1)$$

in which the reference standard is usually taken to be SMOW (Standard Mean Ocean Water). $\delta^{18}0$ provides a proxy for continental ice volume because the processes whereby water is removed from the oceans to build continental ice-sheets are processes that fractionate mass. Water that is anomalously rich in $H_2{}^{16}0$ is preferentially taken from the oceans in the processes of evaporation and subsequent precipitation during which massive continental ice-sheets are constructed. Figure

1 illustrates such deep sea $\delta^{18}0$ data with a record from Ocean Drilling Project (ODP) site 677 from the Panama Basin off the north-west coast of the South American continent. This record is probably the most famous in the global archive, being of exceptionally high resolution and having been put on a calendar year timescale by the application of a methodology for orbital tuning (e.g., see Peltier 2007 for a recent discussion of this procedure as originally applied to this data set). This analysis was extended to a large set of such deep-sea $\delta^{18}0$ records in Shackleton (2000) who showed that it implied the existence of a significant error in the radiometric dating of the Brunhes-Matuyama boundary, the time in Earth history when the last reversal in the polarity of the Earth's magnetic field occurred. The implied 50,000 year error in the age of this important control point was subsequently confirmed by Baksi (1992) through the application of step-heating $^{39}Ar/^{40}Ar$ radiometric dating, a methodology not subject to the errors inherent to the K/Ar method that had been employed to obtain the original 730,000 year age for the B-M transition. The fact that the correct 780,000 year age of this event was determining on the basis of the assumption that the growth and decay of continental ice-sheets were driven by orbitally induced variations in solar insolation is probably the most direct proof available that the Late Quaternary ice-age has been controlled by this so-called Milankovitch (1920) effect.

Inspection of Figure 1 will show that the $\delta^{18}0$ record in ODP core 677 changes character markedly in mid-Pleistocene time at approximately 900,000 years before present (e.g., see Deblonde and Peltier 1991 for a detailed statistical analysis of this mid-Pleistocene climate transition). This is illustrated by the contrast in the power spectra of the $\delta^{18}0$ record for the first and last million years of this 2 million year record (Figure 1b). After the transition, the variability in continental ice-volume is dominated by a rather sharp spectral line corresponding to a period near 100,000 years. Prior to the transition, however, this timescale is essentially absent. Also shown on Figure 1 is the time series (Figure 1c) and associated power spectrum (Figure 1d) for summer-time solar insolation at 65°North latitude over the same range of time. Inspection of these data make it clear that there is essentially no power in the orbital insolation forcing at the timescale of 100,000 years that dominates the climate system response subsequent to the mid-Pleistocene transition. However, the spectral line at 41,000 years period and the cluster of three lines at 19,000, 21,000 and 23,000 years are present in both segments of the record.

The origins of the timescales present in the astronomical forcing of the Pleistocene climate variability signal are made clear in Figure 2 where the primary geometrical properties of Earth's orbit around the Sun are sketched. The timescale of 41,000 years is associated with the temporal variability in orbital obliquity, that is the timescale of variability of the tilt of the spin axis with respect to the plane of the ecliptic. At present this angle is approximately 23.5 degrees but this varies as a consequence of gravitational n-body effects by a degree or so to both higher and lower tilts as the orbit evolves. On the other hand, the triplet of spectral lines at high frequency arise from the eccentricity modulation of the impact of the precession of the equinoxes on received insolation. Because the dominantly 100,000 year periodic variation of orbital eccentricity simply modulates the amplitude of the precessional effect, there is no power in the insolation forcing at this period. This will be evident from the formula for the variation of summer seasonal insolation that is presented on Figure 2. The effect of this modulation is to "split" what would otherwise be a "singlet" in precessional forcing, that would otherwise appear at the precession period near 22,000 years, in three distinct spectral lines. The fact that there is no power in the variations of solar insolation that are responsible for ice-age occurrence at the 100,000 year period that characterizes the variability of orbital eccentricity, yet the ice volume expression of the response of the climate system to this forcing is dominantly at this period, has profound implications. Specifically, this discrepancy implies that the climate system is fundamentally nonlinear, a property of physical systems that implies an ability to respond to stimulus in a way that is out of proportion to the strength of the stimulus itself.

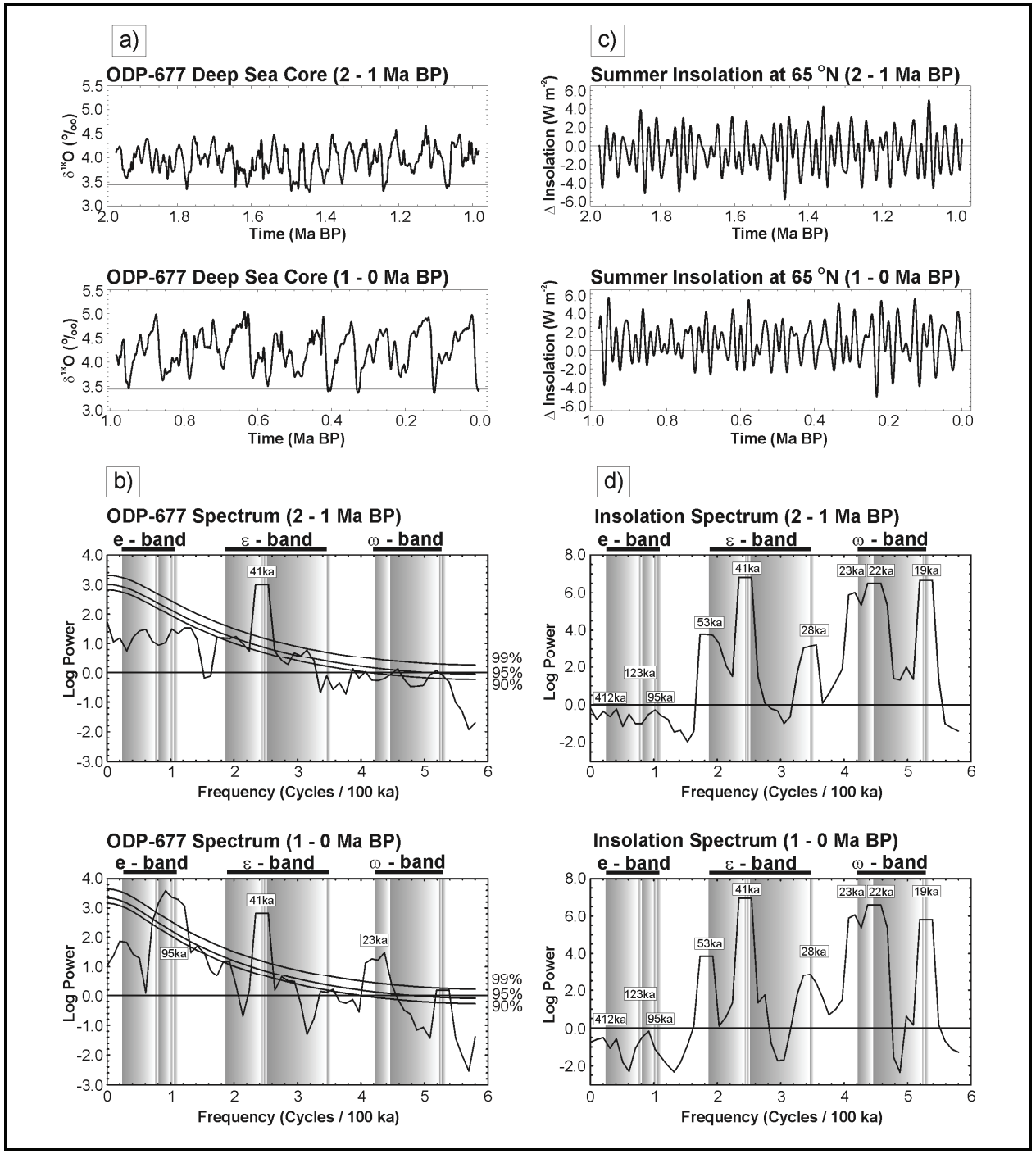

Figure 1. (a) Time series and (b) the power spectrum of the $\delta 1^{80}$ record from the ODP-677 core that was raised from the Panama Basin off the northwest coast of the South American continent. (c) the time series and (d) the power spectrum of the summer insolation signal at 65°N latitude for the first and second million years of the Pleistocene epoch of Earth history.

The 90%, 95%, and 99% confidence level curves are also shown in (b). Also marked on each of the power spectra are the locations of the eccentricity "e" band, the obliquity "ε" band and the precession "ω" bands in temporal frequency.

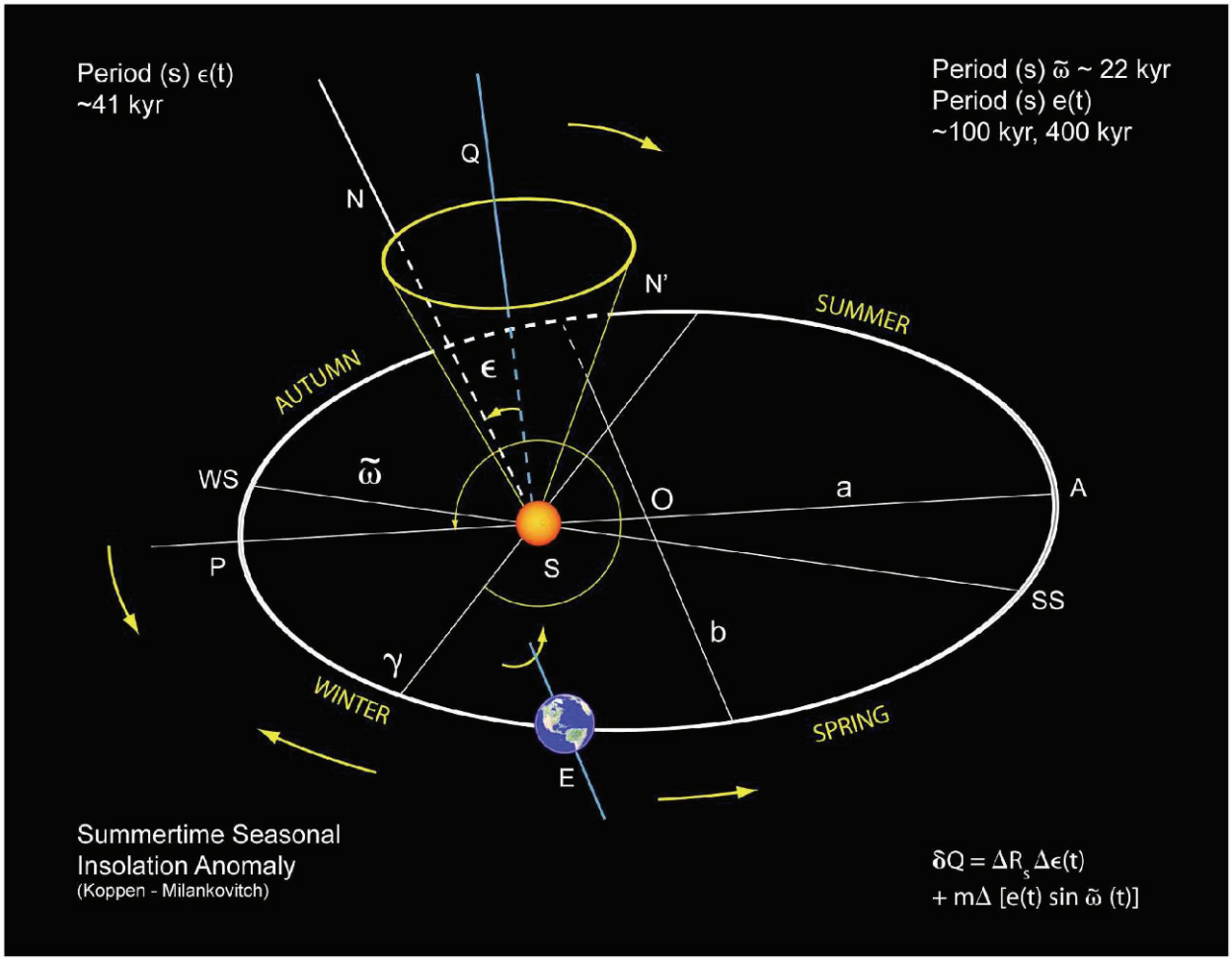

Figure 2. Elements of the Earth's Orbit

The Sun "S" is represented by the ellipse PEAP, "P" being the perihelion and "A" the aphelion. The eccentricity of the ellipse "e" is defined by the ratio $\sqrt{(a^2 - b^2)}/a$, "a" being the semi-major and "b" the semi-minor axes of the ellipse. "WS" and "SS" are the current winter and summer solstices respectively and γ is the vernal equinox. The line "SQ" is perpendicular to the plane of the ecliptic and obliquity ε is the angle between "SQ" and the Earth's axis of rotation, "SN". $\omega = \pi + \psi$ is the longitude of the perihelion relative to the moving vernal equinox γ. The motion of γ is the annual general precession in longitude ψ which describes the absolute motion of γ along the earth's orbit relative to the fixed stars. The longitude of perihelion π is measured from the reference vernal equinox and describes the motion of the perihelion relative to the fixed stars. Also shown on this figure is the formula for the summertime seasonal insolation anomaly that was suggested by Milankovitch as being responsible for ice-age occurrence.

The most direct measure of the mass of water that has been transferred from the oceans to land ice on the continents during a typical 100,000 year cycle of the Late Quaternary period is provided by measures of the variation in sea level that have occurred during the most recent of these events. Figure 3 shows the results of the most recently published analysis of this aspect of the phenomenon, from the paper of Peltier and Fairbanks (2006). This record of relative sea level history is from the island of Barbados in the Caribbean Sea and is based upon U/Th dated coral samples, the most important species of which is the species *Acropora Palmata* which lives within 5 m of sea level in the modern ecology. This species is represented by the data points on Figure 3 with the shortest attached error bars. Also of interest in this new data set are the data associated with the species *Montastrea Annularis* that appear on Figure 3 attached to the error basis of intermediate length. The analysis of the complete data set described in Peltier and Fairbanks (2006) demonstrates that the variation of ice-equivalent mean sea level through the most recent glacial-interglacial transition has been very close to 120 m, the estimate usually derived on the basis of benthic oxygen isotopic measurements from deep-sea sedimentary cores (e.g., Shackleton, 2000). The competing estimate of the LGM eustatic lowstand of the sea represented by the color coded crosses (Lambeck and Chappell, 2001) suggest a much greater sea level depression at LGM of ~ 140 m but this estimate is entirely ruled out by the extended Barbados data set of Peltier and Fairbanks (2006). The inset to Figure 3 compares the prediction of the ice equivalent eustatic sea level history of the ICE-5G (VM2) model of Peltier (2004) with the complete last glacial cycle of sea level history of Waelbroeck et al. (2002) that was deduced on the basis of temperature corrected benthic oxygen isotopic measurements. This comparison demonstrates that the ICE-5G (VM2) model accurately satisfies the constraints on global ice volume provided by sea level measurements over the last glacial cycle.

Figure 4 compares the detailed properties of this ice volume history model in disaggregated form. The figure not only displays the total of the contributions from all deglaciating areas but also the contributions from each of the main ice-covered regions. These disaggregated results are shown for both an earlier ICE-4G (VM2) model (Figure 4a) and for the more recent ICE-5G (VM2) model (Figure 4b). The observational rationale for the significant shift in continental ice-sheet mass from northwestern Europe to North America is described in Peltier (2002a) and Peltier (2004), with the more recent model being characterized by a net contribution to global sea level rise of approximately 80 m from the North American continent. This is to be contrasted with the 61.5 m contribution that was characteristic of the precursor ICE-4G (VM2) model. This is a primary characteristic of the North American glaciation process that will have to be reconciled by any acceptable model of the process.

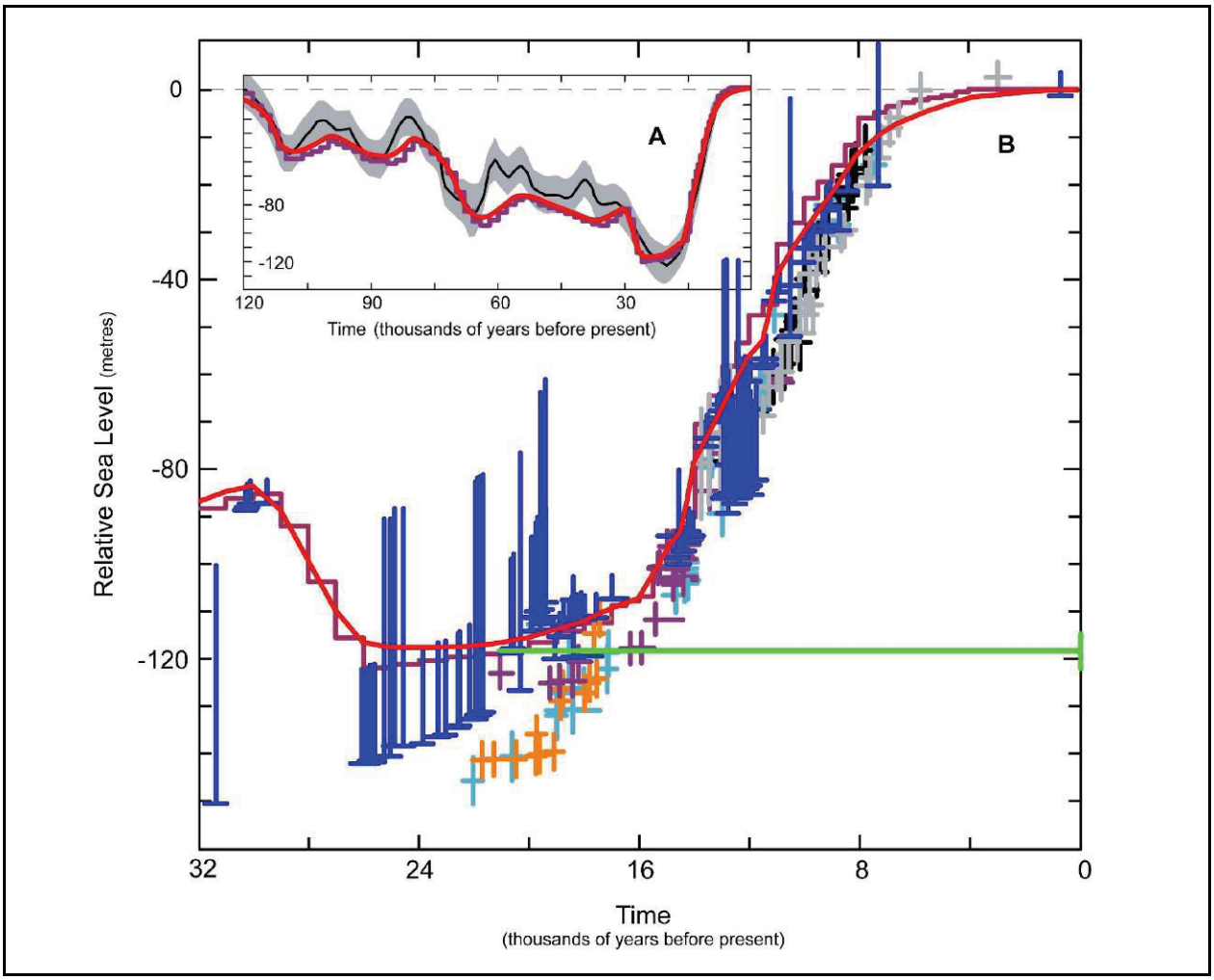

Figure 3. Comparison Between Eustatic Ice-Equivalent Sea-Level History Estimate and the Coral-Derived Record from the Island of Barbados in the Caribbean Sea

This figure compares the eustatic ice-equivalent sea-level history estimate provided by the coral-derived record from the island of Barbados in the Caribbean Sea, shown by the blue symbols, with the estimate of the same characterization of the most recent deglaciation event provided by Lambeck and Chappell (2001). The prediction of the ICE-5G(VM2) model for the Barbados location over the same range of time is denoted by the red curve. The color coding of the Lambeck and Chappell estimates, which are shown as the crosses, is as follows: cyan (Barbados), orange (Bonaparte Gulf), black (Huon Penninsula), grey (Tahiti), purple (Sunda Shelf). As discussed in detail in Peltier and Fairbanks (2006), it will be noted that the data from both Barbados and Bonaparte Gulf are plotted 20m below the depth from which the samples were actually recovered. The inset to the figure shows the reconstruction of eustatic sea level history for the entire last glacial cycle of Waelbroeck et al. (2002) based upon benthic deep sea core oxygen isotopic data corrected for contamination due to the change in the temperature of the abyssal ocean. The prediction of the history of sea-level change over the same period using the ICE-5G(VM2) model of Peltier (2004) is shown by the red curve.

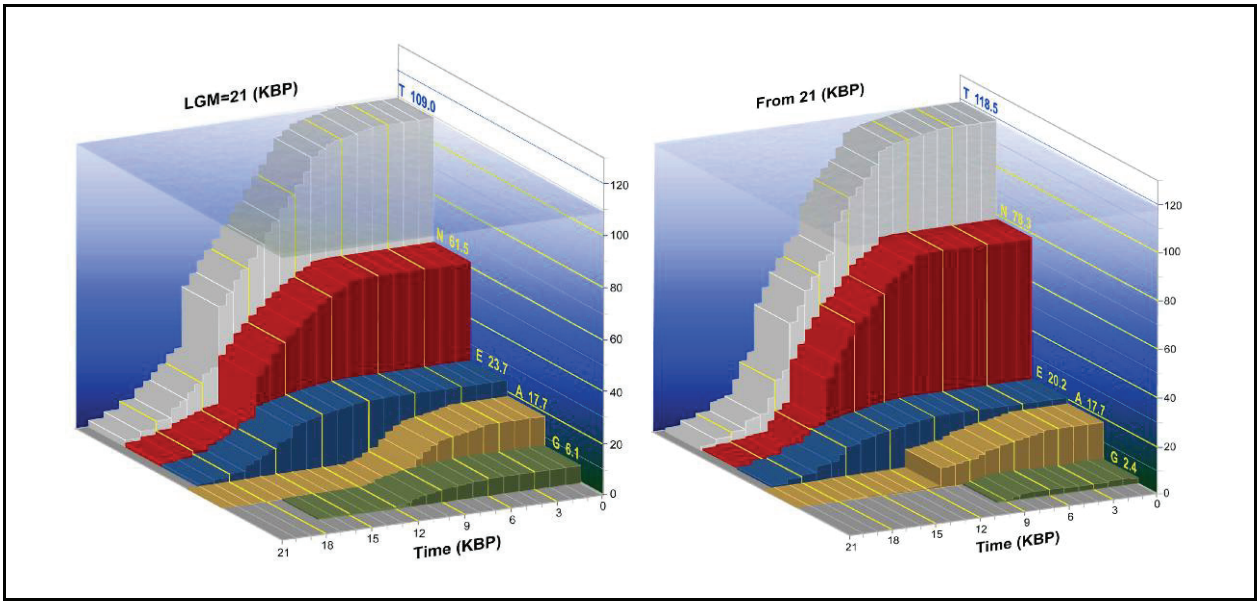

Figure 4. Eustatic Sea-Level Curves for the ICE-4G and ICE-5G Models of the Last Deglaciation Event of the Late Quaternary Ice-Age

For each model the total eustatic variation is shown together with the contributions from each of the main centres of glaciation that contributed to the deglaciation process. These regions are denoted by "N" for North America, "E" for Eurasia, "A" for Antarctica and "G" for Greenland. It is important to note that the North American ice sheet is considerably more massive in the ICE-5G model than it was in ICE-4G. Also important is the fact that Antarctica is assumed to have begun to deglaciate rather abruptly at the time of meltwater pulse 1b in the Fairbanks record that occurred at the end of the Younger-Dryas cooling event at approximately 11,500 years ago.

2.2 How North American Ice-Sheets have Nucleated in the Past

The past decade has seen very significant advances in our understanding of the detailed spatio-temporal processes that have led to the development of continental scale glaciation events during the last half of the Pleistocene epoch of Earth history. Although it has been clear since publication of the seminal paper by Hays, Imbrie and Shackleton (1976) that orbital insolation variations were the ultimate cause of these singular events in Earth history, there are many subtle influences that contribute to the precise way in which individual events have occurred and many of these continue to be actively debated.

Figure 5 (from Vettoretti and Peltier, 2004) has been constructed in an attempt to describe variation of Arctic insolation integrated over the spherical annulus from 65°N to 80°N gain further insight into the complexity of this process. The five parts of this figure respectively show time series of oceanographic $\delta^{18}0$ in (a), of atmospheric CO_2 concentration measured in air bubbles in Antarctic ice-cores (b), the variation of orbital obliquity (c), the variation of eccentricity modulated precession (d) and finally in (e) the variation of Arctic insolation integrated over the spherical annulus from 65°N to 80°N gain further insight into the complexity of this process.

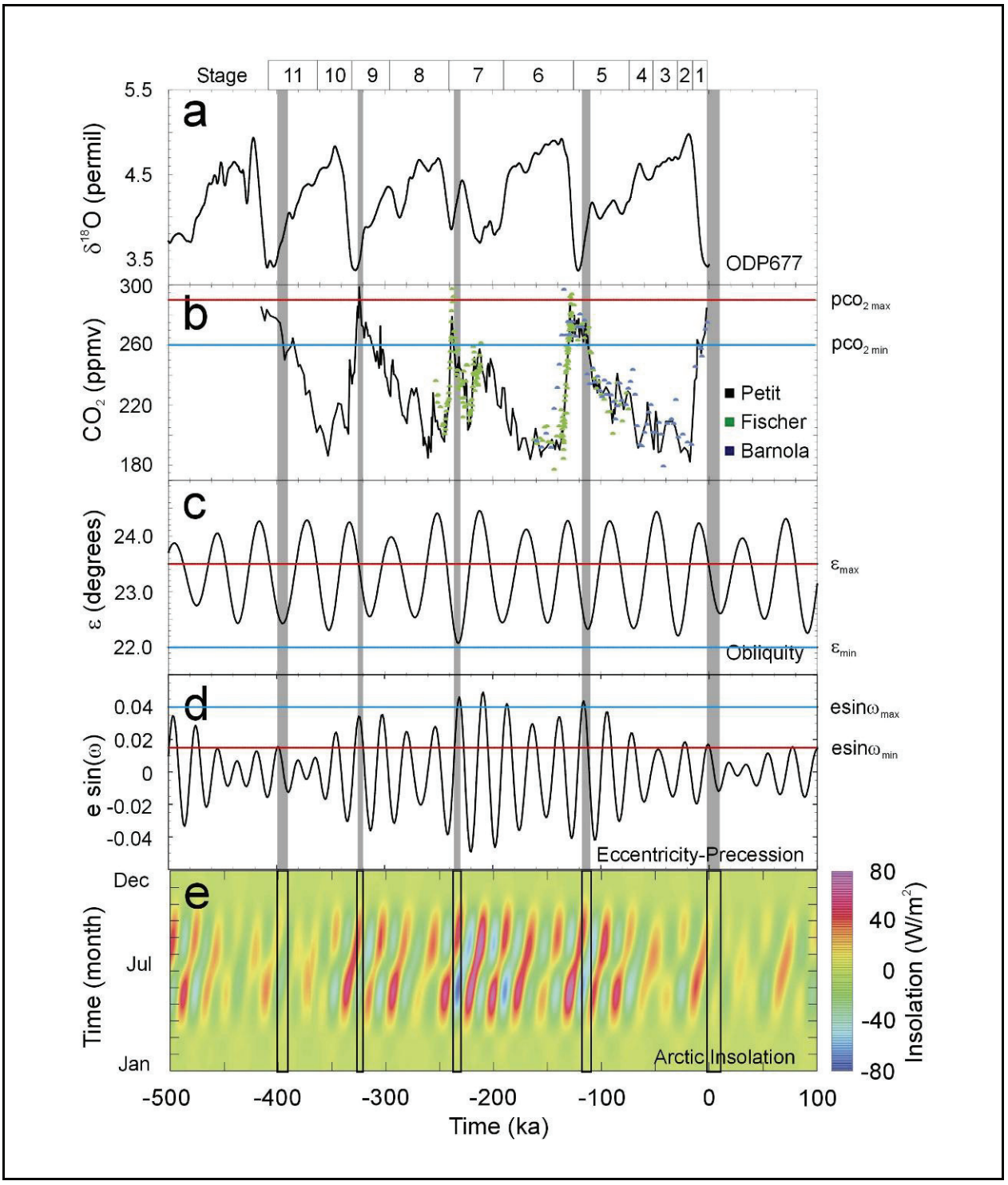

Figure 5. **(a) The last 500,000 years of $\delta^{18}O$ (per mil) isotope record from ODP-677 and (b) the CO_2 record (in ppmv) from the Vostok, Antarctica ice core. (c) shows the variation of orbital obliquity in degrees, (d) shows the orbital variation of $e\sin\omega$ and (e) the insolation (in W/m^2) from 500,000 years before present to 100,000 years beyond the present. All of these data are time correlated and the numbers of the conventional Marine oxygen isotopic stages are indicated**

at the top of the figure. The vertical stipled grey regions represent past interglacial periods during which Northern hemisphere ice sheet growth was initiated. The next most probable period of glacial inception is also indicated. The two values for each of CO_2, obliquity and the product of eccentricity and precession are displayed with red and blue lines to indicate whether they favour relatively warm or relatively cold conditions for glacial inception.

All five (5) time series (Figure 5) are shown time synchronously for the past 500,000 years of Earth history during which five cycles of global glaciation deglaciation have occurred. The vertical grey strips on this figure that cross-cut the five time series represent past interglacial periods during which northern hemisphere ice-sheet initiation events occurred. Notable is the fact that these events have inevitably corresponded to times of minimum high latitude summer insolation. Also shown on this figure by the horizontal red and blue lines, on the middle three (3) of these time series, are the ranges of atmospheric pCO_2, orbital obliquity and orbital e sin(ω) within which past inception events have occurred.

A preliminary detailed study of the glacial inception process was published in Vettoretti and Peltier (2003a,b) in which the mixed-layer ocean coupled atmospheric general circulation model of the Canadian Climate Centre was employed to investigate the issue as to whether modern AGCM's were capable of predicting the inception of glaciation if the only modification to the model from a modern configuration was to switch the orbital insolation regime to one that corresponded to the most recent such event that occurred approximately 116,000 years ago. That analysis demonstrated that orbital insolation variations alone appeared to be sufficient to initiate the process in the sense that perennial snow cover was predicted to develop over the high elevation regions of Baffin Island and over the Queen Elizabeth Islands of Canada due solely to the change in insolation regime. When summer insolation is sufficiently low, the snow that has fallen in the previous winter is able to survive the summer melt season. In such circumstances, successive annual snowfalls accumulate and are gradually transformed into a sheet of ice that is able to flow over the landscape under the action of the force of gravitation.

In Vettoretti and Peltier (2004) this initial analysis was further extended to include the influence of variations in atmospheric CO_2 concentration. A sensitivity study was performed using the same version of the CCCma model employed in the initial study in which obliquity ε, e sin(ω) and CO_2 concentration were varied across the extrema of these quantities shown on Figure 5 to cover the range of these quantities that had been characteristic of past inception events. Figure 6 illustrates the variation of the insolation anomaly across the extremes of both ε and e sin(θ), a sequence that demonstrates very clearly that it is a combination of low orbital obliquity ε and high eccentricity e that is most conducive to the development of an intense negative anomaly in summertime seasonal insulation.

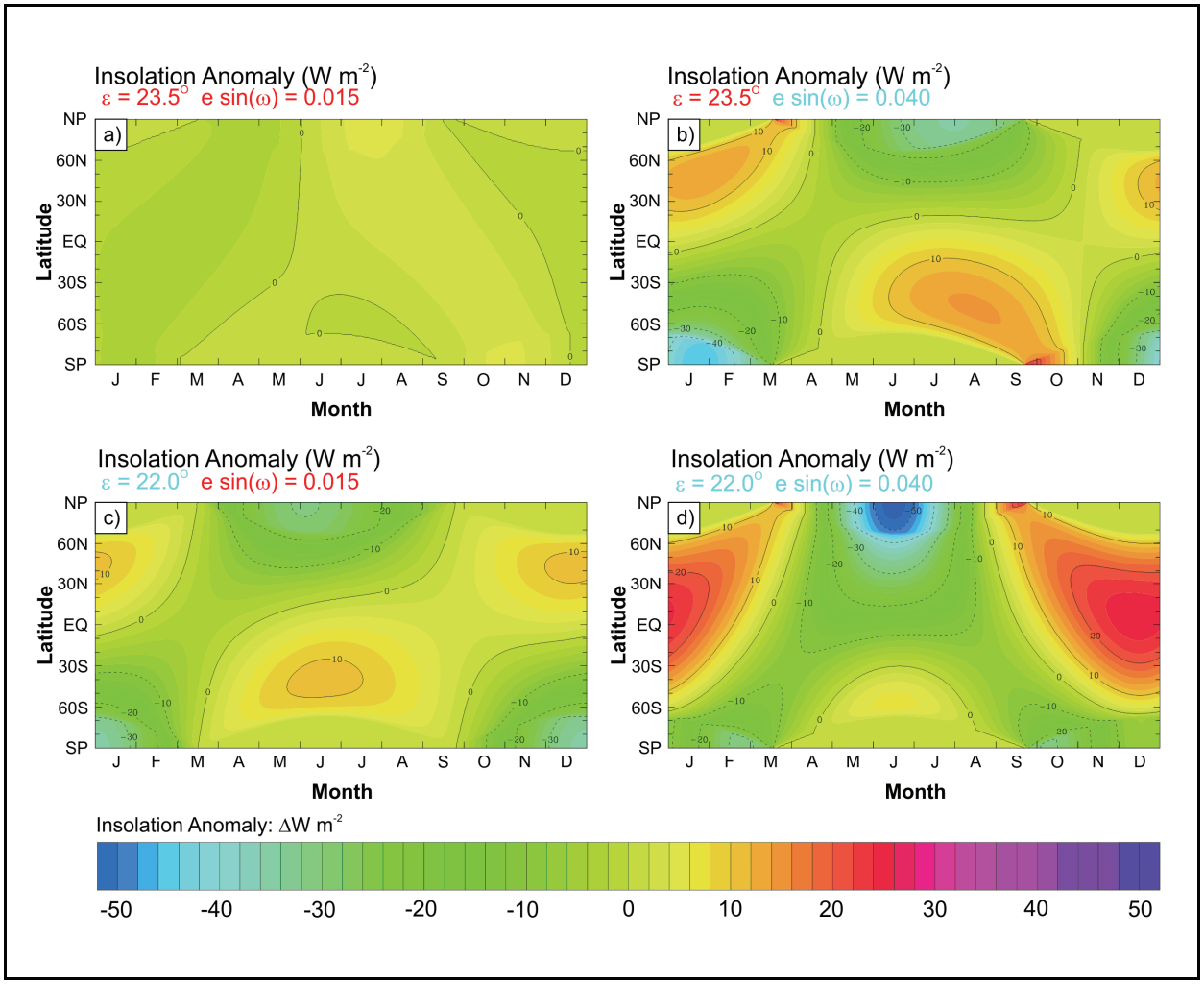

Figure 6. Changes relative to modern of the daily insolation at the top of the atmosphere, measured in W/m^2 as a function of time of year and latitude for the four different orbital configurations employed for an analysis of glacial inception.

When this sequence of orbital insolation anomalies is applied to the AOGCM and the snow accumulation rates monitored that are delivered by the model, then the results obtained from the version of the Canadian model designed by Vettoretti and Peltier (2004) are shown on Figures 7a and 7b for atmospheric CO_2 concentrations of 290 and 260 ppmv respectively. On these figures the snow accumulation rates are given in m/kyr. Inspection of these results demonstrates that under warm orbit (high ε, low e sinω) conditions no snow accumulation is predicted anywhere over North America, only on the northern tip of Greenland is this suggested to be important. Since Greenland is already heavily glaciated this result is not unexpected. When either e sin(ω) or ε but not both are shifted to a cold summer orbit condition there is the onset of some very modest perennial snow cover over Ellesmere Island but not elsewhere. However, when both parameters are shifted to the cold orbit extremum shown on Figure 5 a very significant expansion of arctic perennial snow cover occurs, either at pCO_2 = 290 ppmv or at pCO_2 = 260 ppmv.

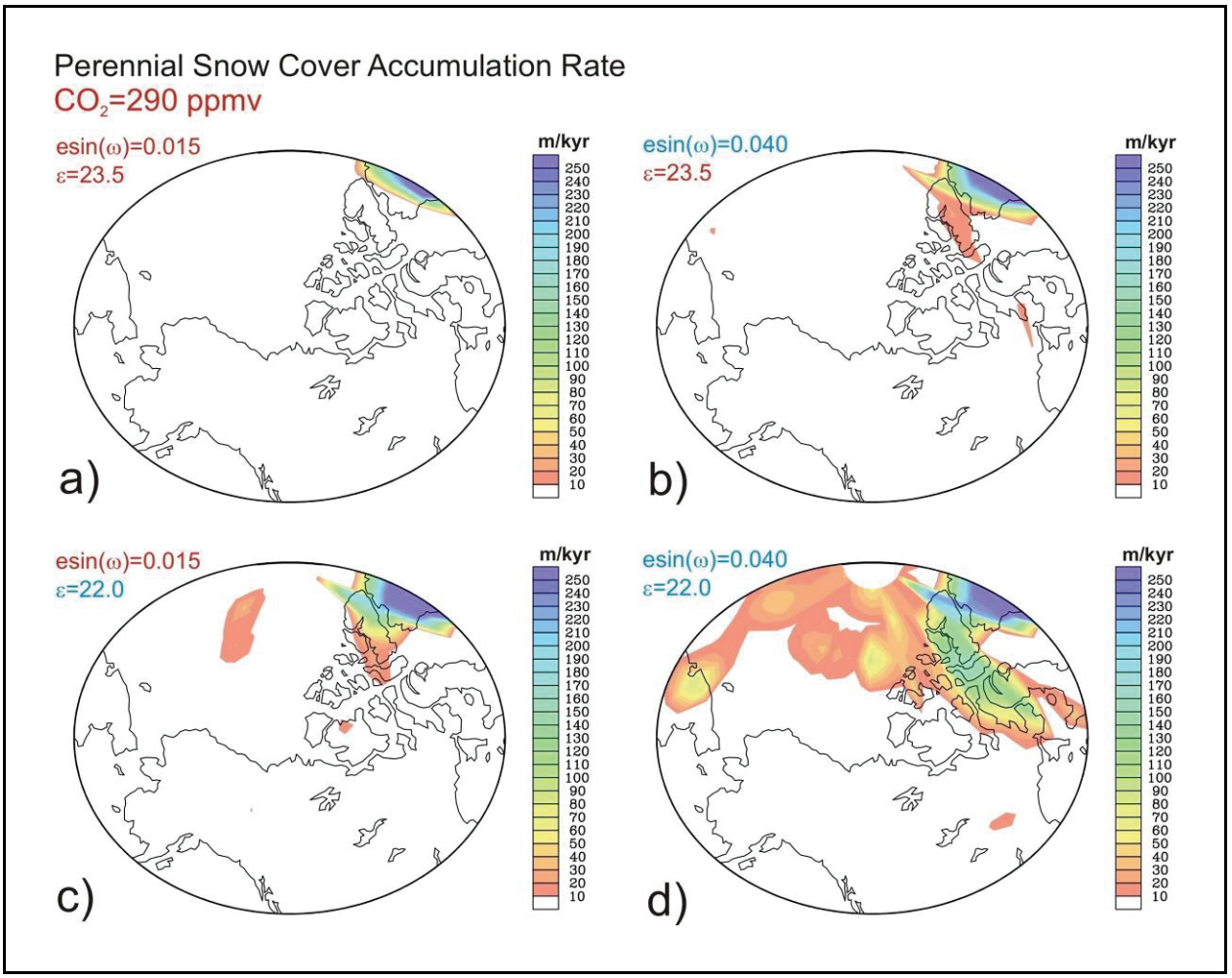

Figure 7a. Arctic polar perennial snow accumulation rate for the set of four orbital configurations under an atmospheric CO_2 concentration of 290 ppmv. Accumulation rates are in m/kyr. The coloured values of obliquity, eccentricity-precession and CO_2 concentration are intended to indicate whether the contribution of this factor is decrease (warm conditions) or to increase (cold conditions) the propensity for glacial inception.

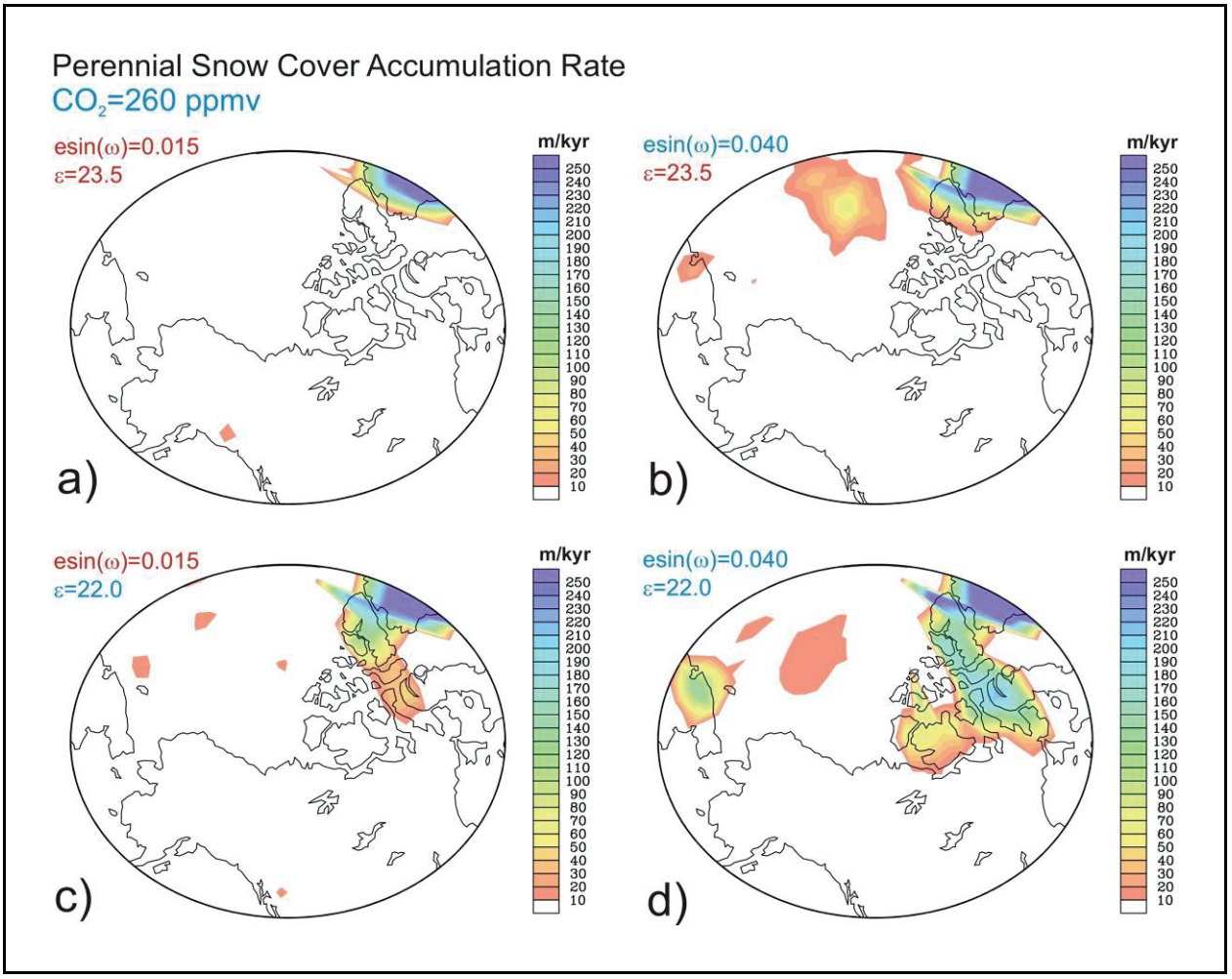

Figure 7b. Same as Figure 7a but for a CO_2 concentration of 260 ppmv.

Figure 8 shows snow accumulation time series from a 40 year integration for each of the distinct computations performed in this sensitivity study and for two different regions in the Canadian Arctic, respectively Ellesmere Island (84°N, 71°W) and the Canadian Arctic archipelago (76°N, 86°W). These results demonstrate the greater sensitivity of the higher latitude location of Ellesmere Island to the conditions that favour the onset of continental glaciation.

Based upon these climate sensitivity results it will be clear that the results of the application of modern AOGM technology agree with the Milankovitch hypothesis that orbital insolation variations, acting alone, are sufficient to have initiated the expansion different regions in the Canadian Arctic, respectively Ellesmere Island (84°N, 71°W) and the Canadian Arctic archipelago (76°N, 86°W). These results demonstrate the greater sensitivity of the higher latitude location of Ellesmere Island to the conditions that favour the onset of continental glaciation.

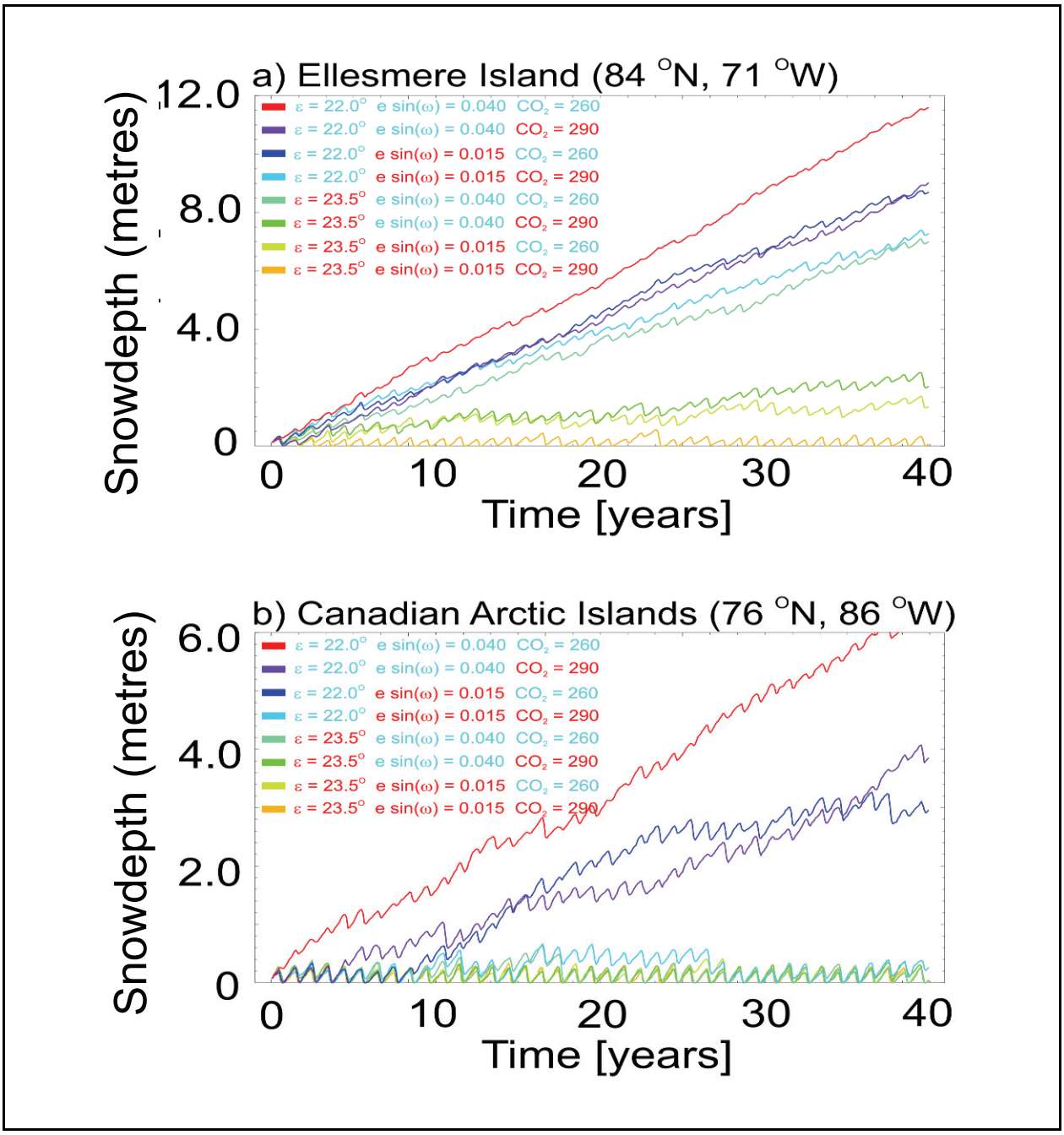

Figure 8. Time series of snow accumulation in metres for the eight sensitivity experiments over a 40 year period for two locations, respectively Ellesmere Island and the Canadian Arctic Islands. The coloured values of obliquity, eccentricity precession and CO_2 are intended to indicate whether this contribution to the forcing is towards warming or cooling during glacial inception.

Based upon these climate sensitivity results it will be clear that the results of the application of modern AOGM technology agree with the Milankovitch hypothesis that orbital insolation

invariations, acting alone, are sufficient to have initiated the expansion of continental scale ice-sheets over the Late Pleistocene. Inspection of part (e) of Figure 5 furthermore demonstrates that conditions will not be favourable for the next advance of continental scale glaciation for approximately 60,000 years. In this sense the present interglacial period is expected to be as prolonged as was that corresponding to Oxygen Isotope Stage 11 (see top of Figure 5 for the time intervals corresponding to the conventionally numbered oxygen isotope stages).

2.3 The Next Century

For the next century of Earth history, as described most recently in the Fourth Assessment Report of the Intergovernmental Panel on Climate Change (IPCC, AR4), the Earth system is committed to considerable warming of its mean surface temperature as a consequence of increasing greenhouse gas concentrations. No matter what steps the international community might take to decrease the anthropogenic emissions of greenhouse gases the warming trajectory will not be affected for the next three decades or more. However, the decisions being made today that may shift the system onto a different trace-gas trajectory will have an important impact upon the warming that occurs by the end of this century. This warming, which is strongly enhanced in the Arctic due to the process of polar amplification, would of course act so as to strongly inhibit the onset of another glacial cycle of Late Pleistocene type if atmospheric trace gas concentrations remained elevated ~ 60,000 years hence when the next opportunity for glacial onset occurs. Of course there is no guarantee as to whether the current excess of atmospheric CO_2 will not long since have ameliorated. Because we cannot predict precisely whether or when a next glaciation cycle might begin, it is clearly imperative that this possibility be taken fully into account when assessing the safety case for a L&ILW repository that is excavated at depth.

3. MODELING THE ONSET AND DEMISE OF CONTINENTAL ICE-SHEETS

Although modern coupled atmosphere-ocean climate models are able to properly predict the onset of the continental scale glaciation events that have been a recurrent feature of the most recent million years of Earth history, such models are extremely expensive to integrate. Not only are extremely powerful “super” computers required to perform such integrations but the “wall-clock” time required to complete an integration of even a few thousand years can run to a month or considerably more depending upon the spatial resolution at which the integration is performed. It is therefore impossible with existing computational resources to integrate such a model over the 100,000 year period of a typical glacial cycle in such a way as to include a fully coupled ice-sheet into the model. This being the case, special strategies are required in order to finesse this technical difficulty and the design of such strategies is at the current state-of-the-art in this area of science. Although it is expected that fully coupled ice-sheet-climate models will be amenable to direct analysis in the course of the coming decade, for the purpose of this report we will be obliged to rely upon a more sophisticated strategy, one that involves making up for the lack of a self-consistent climate forcing to apply to the ice-sheet model by applying a number of observational constraints that pertain to the most recent glacial cycle. In following this course we are of course assuming that a next glacial cycle will be similar to those that have occurred previously. The model that we will employ in our analyses is described in the next sub-section of this report.

3.1 The University of Toronto Glacial Systems Model (UofT GSM)

This model is in many respects a standard model of continental scale ice-dynamics in that it is based upon the "shallow-ice" approximation which derives from the assumption that the thickness of the ice-sheet is very much smaller than a characteristic horizontal length scale. Subject to this approximation the continuum mechanical equations for the conservation of mass, momentum and internal energy are reduced to the form of a set of non-linear coupled diffusion equations in (effectively) two space-dimensions that may be applied within limited areas on the surface of the spherical Earth. A detailed description of the derivation of this set of coupled equations is described in Huybrechts (1986). The numerical implementation of the UofT GSM version of this structure is described in Deblonde and Peltier (1991, 1993) and Deblonde, Peltier and Hyde (1993) and more recently in Tarasov and Peltier (1997, 1999, 2002, 2004, 2005, 2006). In this model, the time dependence of ice-thickness "H" is described by the vertically integrated equation of mass conservation as:

$$\frac{\partial H(\underline{r})}{\partial t} = -\underline{\nabla}_h \bullet \int_{z_b}^{h} \underline{V}(\underline{r})\, dz + G\left(\underline{r}, T(\underline{r}, t)\right) \tag{2}$$

in which G is the temperature dependent net surface and basal mass-balance and H is the space and time dependent ice-thickness. The horizontal velocity within the ice is represented by the vertical integration of the constitutive equation for strain rate $\dot{e}_{ij}$ as a function of stress τ_{ij} within the ice. This may be written in the general form;

$$\dot{e}_{ij} = f\, A(T^P)\, \tau_p^{n-1}\, \tau_{ij} \tag{3}$$

in which T^p is the absolute temperature relative to the pressure melting point of ice, τ_p is the effective shear stress or the second invariant of the stress tensor, A is the temperature dependent coefficient of the flow law and f is an acceleration factor that must be introduced to account for the influence of anisotropy of the fabric of the ice and/or the presence of impurities which act to accelerate the flow rate above the rates that would exist in the absence of these effects. By integrating equation (3) in the vertical, the following relation is obtained for the horizontal velocity:

$$\underline{V}(z) - \underline{V}(h) = -2(\rho_i g)^n \left[\underline{\nabla}(H+h) \bullet \underline{\nabla}(H+h)^{\frac{n-1}{2}}\, \underline{\nabla}(H+h) \int_h^z f A(T^P)(H+h-z)^n\, dz \right] \tag{4}$$

The flow law enhancement factor f in (3) is fixed to the value 6.5 on the basis of fits of this model to the existing profile of the Greenland ice-sheet (Tarasov and Peltier 2002, 2003). To obtain the vertical average of (4) that is needed in (2) we simply integrate (4) in the vertical and divide by the local ice-thickness. The net effect of this shallow ice treatment of the cryodynamics is that the influence of longitudinal stresses upon the flow of ice is entirely neglected. Equation (2) has the form of a nonlinear diffusion equation on the surface of the sphere.

Because the temperature of the ice is critical to the understanding of its flow rate via (3) and to the crucial issue of basal melting and meltwater production, it is imperative that the temperature field within the ice be accurately modeled together which ice-flow. In the UofT GSM the temperature of the ice is described by the evolution equation:

$$\rho_i C_i (T(\underline{r})) \frac{\partial T(\underline{r})}{\partial t} = \frac{\partial}{\partial z}\left(k_i (T(\underline{r})) \frac{\partial T(\underline{r})}{\partial z} \right) - \rho_i C_i \underline{V} \bullet \underline{\nabla} (T(\underline{5})) + Q_d (\underline{r}) \qquad (5)$$

This describes the impact upon thermal evolution of the ice due to three dimensional advection, vertical diffusion and heat generation by shear heating Q_d. Additional heating due to sliding of the ice over its bed is also introduced through the lower boundary condition. This lower boundary condition also involves coupling to a model of the thermal evolution of the bed of the ice-sheet which is the means whereby the model is able to track the development and evolution of permafrost both under the ice-sheet and in the peripheral region. This characteristic of the glaciation process is especially important in the present context and so is described in detail in the following subsection of the report. Other aspects of the boundary conditions are described in the following sub-sub-sections.

3.1.1 Modeling the Net Mass Balance of an Evolving Ice-Sheet

The function $G(\underline{r}, t)$ in equation (2) represents the net mass balance of the ice-sheet and as such is responsible for driving its evolution over the landscape. The UofT GSM computes the net mass balance as the difference between accumulation and ablation. Under normal conditions a continental scale ice-sheet accretes mass in its interior at high elevation and loses it by ablation at lower elevation at its margin. The elevation at which accumulation is balanced by ablation is referred to as the height of the equilibrium line. The computation of accumulation in the interior is straight forward as it is simply equal to the rate at which snow accumulates. The computation of the ablation rate below the equilibrium line is very much more complicated. In the UofT GSM this is computed using the Positive Degree Day (PDD) method with temperature dependent coefficients derived from energy balance computations (Braithwaite 1995). Details of the computation are provided in Tarasov and Peltier (2002). The influence of surface refreezing is captured by taking into account both capillary retention and latent heating as in Janssens and Huybrechts (2000). The snow fraction is computed using a normal statistical model to determine the monthly fraction of hourly temperatures below 2°C.

When the ice-sheet evolves so as to abut the ocean, ablation will generally occur via calving of the ice during which icebergs are released into the ocean due to the flow of ice in the across-shelf direction. The algorithm employed in the UofT GSM to describe the ablation of ice at an ocean abutting terminus requires either that the water depth exceed 600 m or that all of the following condition are satisfied: (1) the sea surface temperature (SST) exceeds a critical minimum value T_{Cmn}, (2) the ice thickness in the grid element is less than 10% above the maximum buoyant thickness (H_{flot}), (3) an adjacent ice free grid element has a water depth less than 30 m, and (4) there exists an ice free regional drainage outlet. This set of conditions attempts to capture the influence of sea ice blockage of drainage channels as well as to

incorporate current buoyancy control theories of calving for temperate tide-water glaciers (e.g., Vieli et al. 2001, Van der Veen, 2002). When all of these conditions are met, the UofT GSM computes the calving velocity as:

$$U_C = U_{Cmx} \bullet n_{edge} \,.\, \min\left\{1, \left[\frac{1.1\, H_{flot} - H}{0.25\, H_{flot}}\right]^2\right\}$$

$$\bullet \min\left\{1, \left[\exp\left(\frac{T_s - T_{Cmx}}{T_{Cmx} - T_{Cmn}}\right) - \exp(-1)\right] / (1 - \exp(-1))\right\} \qquad (6)$$

The model takes account of the number of grid-box edges (n_{edge}) which meet the calving conditions and employs the high temperature point (T_{Cmx}) and the maximum calving velocity (U_{Cmx}) as ensemble parameters to be randomly sampled in the process of the Bayesian calibration process to be discussed in what follows.

3.1.2 Modeling the Dynamical Processes at the Base of the Ice-Sheet

When the base of the ice sheet approaches the pressure melting point, ice-sheet motion may be enhanced due either to sliding at the base or to the deformation of sub-glacial sediments (e.g., Piotrowski et al., 2002). In order to avoid an excess of assumptions concerning the importance of till deformation, the viscosity of a underlying till layer is taken to be an ensemble parameter. The representation for the basal velocity of ice moving over deforming till is determined subject to the following assumptions: (1) the effective pressure at the till-ice interface is zero, (2) the shear stress of the till surface is equal to that of the basal ice, (3) the till layer is unfrozen whenever the basal ice is at the pressure melting point, (4) the thickness of the till is large enough that the shear stress reaches the yield stress of the till, and (5) the till is Coulomb plastic. Under these conditions the basal velocity of the ice above the till is given by:

$$u(z_b) = f_b(x,y) \bullet \frac{1}{n+1} \bullet \tau^{n+1} \bullet \frac{\mu_o^{-u}}{(\rho_t - \rho_w)\tan\varphi} (2D_o)^{n-1} \qquad (7)$$

In (7) the UofT GSM takes the till deformation parameters to be the following: (1) till deformation exponent n = 1.25, (2) sediment angle of internal friction $\varphi = 22^o$, (3) density of till $\rho_t = 2390$ kg/m^3, (4) Newtonian reference deformation rate $D_o = 7.9^{-7}$ s^{-1}. See Jenson et al. (1996) for a discussion of all of these parameters. In the ensemble analysis that is basic to the Bayesian calibration of the model we will assume the till viscosity μ_o to vary from a lower bound constrained by the model time step of 1.1×10^9 Pa s to an upper bound of 4.5×10^{10} Pa s. In order to represent the portion of the surface covered by sediment, the UofT GSM employs the sediment thickness map of Laske and Masters (1997).

As opposed to this enhancement of the motion by till deformation, the model represents the sliding process by employing a Weertman (1957) sliding law with a stress exponent of three and a moderate sliding parameter. Since the model does not incorporate explicit ice shelf dynamics, a strong linear sliding law is smoothly introduced whenever ice approaches buoyant support with a sliding parameter of 0.07 P_a^{-1} m yr^{-1}. In order to enhance numerical stability and to allow for the existence of sub-grid-scale heterogeneity, all basal sliding and sediment deformation are turned on smoothly from a temperature 0.25°C below the pressure melting point.

3.1.3 Modeling the Glacial Isostatic Adjustment Process

The response of the solid Earth to variations in surface mass load is computed using the linear visco-elastic field theory for a Maxwell visco-elastic model of the Earth originally developed in Peltier (1974, 1976). In this theory the radial displacement of the bedrocks surface ΔR, is computed on the basis of the three dimensional convolution integral:

$$\Delta R(\theta, \lambda, t) = \int_{-\infty}^{t} dt' \iint_{\Omega} d\Omega' \; L(\theta', \lambda', t') \; GF_{\Delta R}(\delta, t - t') \tag{8}$$

in which the Green function $FG_{\Delta R}$ was first determined in Peltier (1974). Required inputs to the construction of this Green function include a model of the radial elastic structure of the planet which consists of depth profiles of density and the elastic Lamé parameters and a model of the depth dependence of mantle viscosity. The radial elastic structure employed in this component of the UofT GSM is that of the PREM model of Dziewonski and Anderson (1981), whereas for most of the purposes of this report the radial viscosity structure will be taken to be that of the VM2 model of Peltier (1996). The convolution integral (8) is evaluated using the "full spectral" methodology of Peltier (1976) with the ocean component of the surface load approximated as eustatic. The computation of the bedrock response is asynchronously coupled to the thermo-mechanical model of ice-sheet evolution with a time step of 100 years. Runs of the fully coupled model begin at 122,000 years before present during the Eemian interglacial and continue through a complete 100,000 year cycle of glaciation and deglaciation.

3.1.4 Modeling the Climate Forcing that Controls Ice-Sheet Evolution

Because the surface mass balance function "G" in equation (2) depends critically upon the surface climate variables of temperature and precipitation and because our ability to directly model the evolution of climate over an ice-age cycle is extremely limited, the UofT GSM employs a combination of detailed modeling results and observational constraints to finesse this crucial model component. In order to represent the variation of climate through the ice-age cycle, the model employs a northern hemisphere glacial index I(t) based upon the GRIP $\delta^{18}0$ record from the Summit, Greenland ice-core as a means of interpolating between LGM and modern climate fields produced on the basis of atmospheric general circulation model reconstructions of climate state. The general circulation model results are constructed on the

basis of composites produced from the computations performed in the context of the Paleoclimate Modeling Intercomparison Project (PMIP) as discussed in Pinot et al. (1999). The glacial index "I" used to perform the required interpolation is defined as:

$$I(t) = \frac{\left(\delta^{18}0(t) - \delta^{18}0(o) + \lambda_\delta \left[h_{GRIP}(t) - h_{GRIP}(o)\right]\right)}{\left(\delta^{18}0\,(LGM) - \delta^{18}0(o) + \lambda_\delta \left[h_{GRIP}(LGM) - h_{GRIP}(o)\right]\right)} \tag{9}$$

When t=o (the present day) then I(t) ≡ o, whereas when t = LGM then I(t) ≡ 1. This index therefore measures the "degree of glaciation". We employ it to determine a time dependent temperature field by assuming that surface temperature variations through the ice-age cycle may be computed from the expression:

$$T(\theta,\lambda,t) = T_{obs}(\theta,\lambda,o) + \left[T_{PMIP}(\theta,\lambda,LGM) - T_{PMIP}(\theta,\lambda,o)\right] I(t) - \beta\left[h(\theta,\lambda,t) - h(\theta,\lambda,o\right] \tag{10}$$

in which β is the atmospheric temperature lapse rate which is assumed to be constant. The field T_{obs} is taken to be that corresponding to modern climatology and is based upon the 14 year mean (1982-1995) of re-analysed monthly mean temperature fields (Kalnay et al., 1996). The paleo-precipitation field is similarly based upon the exponential nature of the dependence of saturation vapour pressure upon temperatures. We therefore interpolate between the present day observed climatological field represented by the data set of Legates and Willmot (1990) and the LGM field from the PMIP ensemble of LGM runs as:

$$P(\theta,\lambda,t) = RP_{sm}(\theta,\lambda,t) \bullet P(\theta,\lambda,o)\left[\frac{fP_w(\theta,\lambda,t)\, f_p\, P(\theta\lambda, 21)}{P(\theta,\lambda,o)}\right] I(t)^{f_n P_{dexp}} \tag{11}$$

In (11) the "ensemble phase factor" denoted $f_n P_{dexp}$ is introduced as a means of parameterizing some of the uncertainty associated with the transition from interglacial to glacial atmospheric states whereas the factor f_p is a global scale factor for the ensemble as a whole. The two remaining scale parameters $R P_{sm}(\theta, \lambda, t)$ and $f P_w(\theta, \lambda, t)$ are employed to enable us to introduce regional enhancements or diminutions of precipitation in the period from 30 kyr BP to 10.6 kyr BP, additional degrees of freedom that were found necessary to enable the model to match geophysical inferences pertinent to this period of time. The 30 kyr BP timing of the initiation of these modifications is introduced to enable the model to produce accord with the glaciological inferences of a significant expansion of glaciation in the Keewatin/Alberta sector that is believed to have occurred at this time (Dyke et al., 2002, 2003). The necessity of making such an ad hoc correction derives from the fact that the LGM fields were obtained from GCM runs in which there existed no "Keewatin Dome" in their topographic conditions as these runs were based upon the use of the ICE-4G (VM2) paleotopography of Peltier (1994) rather than the ICE-5G (VM2) model results that have replaced these earlier data sets. The existence of this dome would have significantly altered the precipitation regime of the ice-complex.

The use of a single climate index based upon the $\delta^{18}0$ record from the Summit, Greenland GRIP ice core together with the additional climate related control variables enumerated above is still insufficient to adequately constrain model predictions. In order to more strongly constrain the system we therefore impose an additional requirement that the glaciation history predicted should be one for which the time dependent position of the ice-sheet margins during the deglaciation phase of the 100,000 year cycle match the sequence of radio-carbon dated positions that have been mapped by Dyke et al. (2002, 2003). His data set is shown on Figure 9 for an illustrative sequence of times during the retreat phase of the ice-sheet. During the glaciation phase of the cycle, of course, no such constraints are available.

3.2 Permafrost Evolution Through a Glacial Cycle

As mentioned in the introduction to this report, the issue of permafrost formation during a cycle of glacial advance and retreat is a critical determinant of the extent to which water generated by the melting of a continental scale ice-sheet may infiltrate the subsurface. It is therefore important from the perspective of developing the safety case for a deep geologic repository that this process be considered in detail. The description of the revised methodology employed in the UofT GSM to model permafrost evolution in what follows is based upon that in Tarasov and Peltier (2007).

The present day depth distribution of permafrost over the north polar continents is a reflection of the history as well as the present characteristics of surface thermodynamic forcing. Over the majority of the Canadian landscape this was often decoupled from the overlying regional climate by the presence of thick accumulations of land ice. The impact of this decoupling is, however, poorly constrained, in large part due to the limited number of direct measurements resulting from the general inaccessibility of the regions where permafrost now exists. The present and future depth extent of permafrost throughout Arctic Canada is therefore equally ill constrained. In order to adequately predict the expected impact of on-going global warming on permafrost degradation, an extremely important issue for Canada, we require a model that is demonstrably able to explain both its past evolution and present state.

Model based analyses that employ three-dimensional thermo-mechanically coupled ice-sheet models and constrained climate chronologies offer a means of analyzing and predicting past and present sub-surface temperature fields and thus permafrost depth. Although there have been a few model studies that have examined the evolution of ice-sheets across the North American continent (e.g., Tarasov and Peltier, 1999; Marshall et al., 2000; Marshall and Clark, 2002; Bauder et al., 2005) the results obtained have been poorly constrained due to inadequately understood climate forcings, insufficiently accurate representation of ice-streams and ice-calving into the ocean and the lack of data/model integration. The results to be described in this report, based upon the Bayesian methodology reviewed in the next sub-section, and which include the description of permafrost evolution, are unique in the literature of this subject in that they are based upon formal analyses of the uniqueness of model predictions. In the particular case of permafrost it is also the case that no previous analysis has taken into account the significant thermal offsets for ice-free ground temperature forcing due to seasonal snow cover and to the difference between thawed and frozen ground thermal conductivities (Smith and Riceborough, 2002).

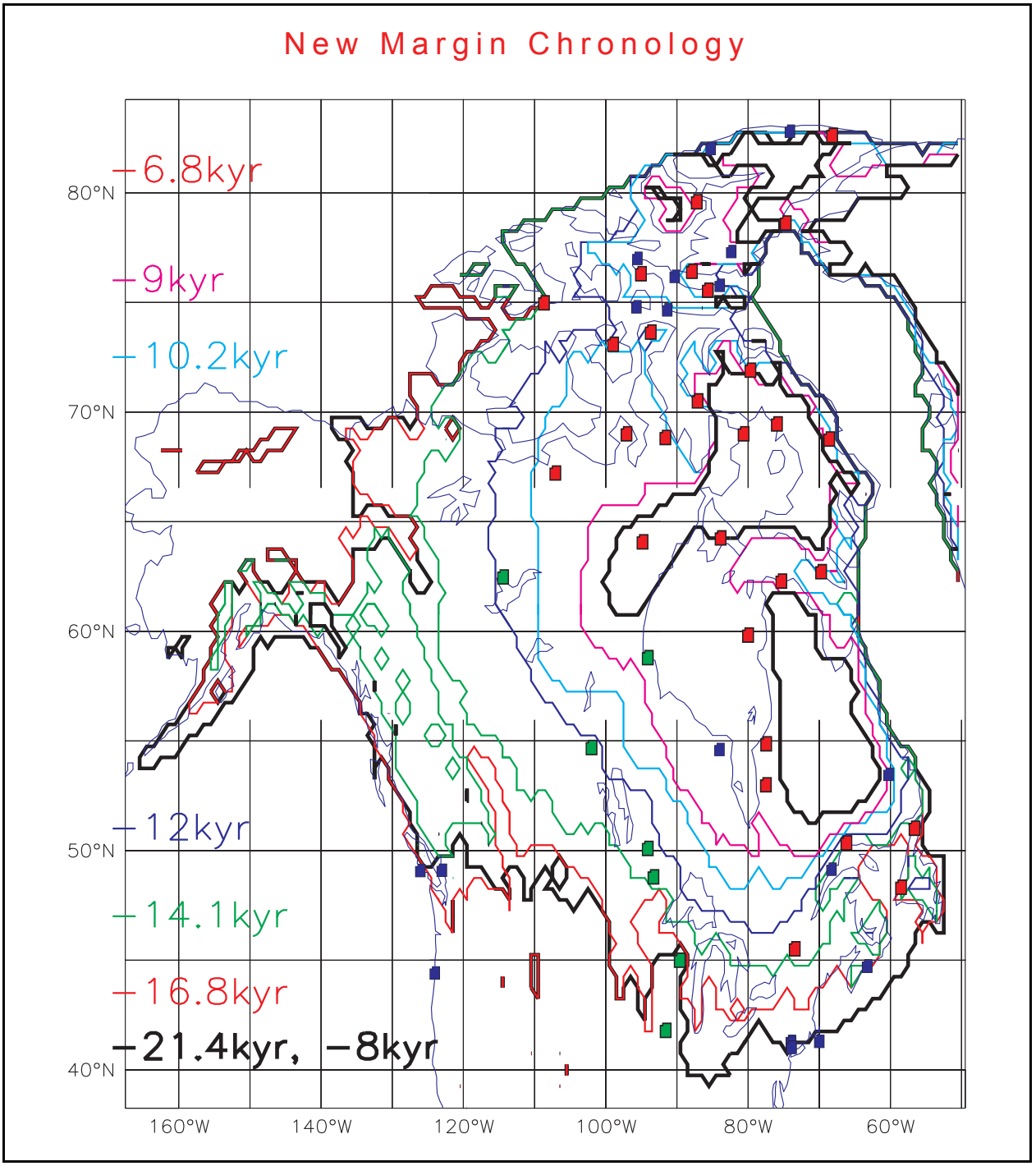

Figure 9. **Time dependent positions of the margin of the Laurentide Ice Sheet from Last Glacial Maximum to the early Holocene based upon the results reported in Dyke et al. (2002). These retreat isochrons are critical to constraining the ice-sheet evolution over this period of time. The locations denoted by the green squares are those for which gravity or vertical displacement rate data are available. Those denoted by red and blue squares are those from which primary and secondary relative sea level data are available, respectively.**

The depth and spatial extent of permafrost over time has important implications for sub-glacial and peri-glacial landform development, sub-glacial hydrology and the evolution of the ice-sheets themselves. Previous studies (e.g., Clark, 1994; Licciardi et al., 1998; Tarasov and Peltier, 2004) have demonstrated that fast flow processes have played a critical role in the evolution of the North American ice-sheet complex. Fast ice-flow due to basal decoupling generally requires warm basal conditions. However, fast flow over sediment also depends on adequate basal water pressure for which permafrost could play an important role in sub-glacial drainage. Based upon ensemble results with a glaciological model, Marshall and Clark (2002) concluded that only 20%-40% of the Laurentide ice-sheet was warm based at LGM but with a much higher fraction during deglaciation. On this basis they suggested that the transition to wide-spread warm-based sub-glacial conditions played a critical role in glacial terminations while cold basal conditions were required for ice-sheet growth. However, the ensemble employed in that analysis was subject to limited constraints as evidenced by the approximately 100 m eustatic equivalent sea-level fall at LGM for the model run for which detailed chronologies were provided. Such a large sea level contribution would leave little more than 20 m eustatic rise to be accounted for by the remaining ice-sheets in the system (Peltier and Fairbanks, 2006). This remainder is only half of that characteristic of the ICE-5G reconstruction (Peltier, 2004) that was based upon the inversion of relative sea level (RSL) data. The models of the glacial cycle developed herein are models that have been designed so as to satisfy this constraint on ice-complex mass as well as other equally important observables.

Insofar as the important permafrost component of the models is concerned, the sub-glacial temperature field is computed at each grid point using a one-dimensional bed-thermal model that is based solely upon the process of vertical diffusion and which spans a depth of 3 km. This simple local model is therefore based upon the partial differential equation:

$$\rho_b \, C_b \, \frac{\partial T}{\partial t} = k_b \, \frac{\partial^2 T}{\partial z^2} \tag{12}$$

in which the bedrock density ρ_b is assumed equal to the mean value for the lithosphere of 3300 kg m^{-3}. The values of the thermal conductivity of the subsurface k_b and the effective heat capacity C_b are poorly constrained due to the strong dependence of these parameters upon bed composition, water content and the impact of freezing. Base model calculations will employ a value for k_b of 3 $Wm^{-1}\,{}^{o}K^{-1,}$ as in the EISMINT II model inter-comparison project. The effective heat capacity of the bed C_b must include a term to account for the impact of the latent heat of fusion L (e.g., Ling and Zhang 2004; Bauder et al., 2005; Mottaghy and Rath, 2006) as:

$$C_b = C_n + L \frac{\partial \alpha_r}{\partial T} \tag{13}$$

in which α_r is the volumetric unfrozen water content. In the analyses that have led to the results to be reported in the next section, α_r is represented as a piecewise constant function with a maximum sediment porosity value of 0.3 at the pressure melting point and a value of zero at 2°C below the pressure melting point in order to ensure linear stability and to optimize energy conservation. The depth of the sediment cover over the landscape upon which glaciation is occurring is important and this is taken to be provided by the map of Laske and Masters (1997).

Bedrock heat capacity C_r is taken to be equal to 1000 kJ kg^{-1} $^oK^{-1}$ as in the EISMINT II protocols (Payne et al., 2000) and the bedrock beneath the sediment cover is taken to be non-porous.

The boundary conditions applied in constructing solutions to the bed-thermal model are the following:

$$T(z=o) = T_{ground} \quad \text{if no ice cover} \tag{14a}$$

$$T(z=o) = T_{base} \quad \text{if ice cover present} \tag{14b}$$

$$-k_b \frac{\partial T}{\partial z}(z=3\,km) = G_f(x,y) \tag{14c}$$

In equation (14c) the deep geothermal heat flux $G_f(x,y)$ is assumed to be provided by the digital heat flow map of Pollack et al. (1993). It is important to understand that there are significant thermal offsets at the ground surface due to the insulating effects of seasonal snow-cover. This is the most important factor after air temperature in determining the southern limit of continuous permafrost (Smith and Riceborough, 2002). The difference in thermal conductivity between wet and dry ground also produces an offset across the active layer. In order to account for these offsets for ice-free-land, a quadratic parameterization for the near surface ground temperature is employed, T_{ground}, as a function of the air temperature. We take this from Smith and Riceborough (2002) whose analysis is based upon their application of Canadian climate station data for air temperature and snowfall and leads to the parameterization:

$$T_{ground} = T_{air} - 1^oC \qquad T_{air} > 4.118\ ^oC \tag{15a}$$

$$T_{ground} = T_{air} \qquad T_{air} < -17\ ^oC \tag{15b}$$

$$T_{ground} = 1.2\ ^oC + A_{ts} \cdot T_{air} - B_{ts} \bullet T_{air}^2, \text{ otherwise} \tag{15c}$$

The ratio of thawed to frozen ground thermal conductivities in this parameterization is conservatively assumed to be 0.6 for regions with sediment cover. For regions that are free of surface sediment, a unit ratio of thermal conductivities is assumed, and the parameterization then takes the form:

$$T_{ground} = T_{air}, \qquad T < -17.14^oC \text{ or } T > 7.375^oC \tag{16a}$$

$$T_{ground} = 3.51751\ ^oC + A_{tr} \bullet T_{air} - B_{tr}\ T_{air}^2, \text{ otherwise} \tag{16b}$$

Sediment free grid cells are identified according to the till map used to constrain the occurrence of fast flow due to sediment deformation and that also have minimum thicknesses of sediment according to the global sediment map of Laske and Masters (1997).

The above described bed thermal model is coupled implicitly to the ice thermodynamics computation and employs 20 vertical levels with layer thickness increasing exponentially with increasing depth. Permafrost depth is then determined by linear interpolation between grid cells to infer the depth of the 0°C isotherm relative to the pressure melting point of ice (assuming hydrostatic pressure throughout and zero pore-water pressure).

3.3 Bayesian "Large Ensemble" Analyses of North American Continental Ice-Sheet Evolution

The methodology that is employed to construct probabilistically accurate models of the evolution of the North American ice-sheet complex and its surrounding and sub-glacial permafrost is fundamentally Bayesian by design. That is to say, we seek to fully explore the range of model evolutionary histories that are compatible with the available constraints and the errors on these constraints. We refer to this process as Bayesian calibration. Of course the most important element of this methodology is the deterministic model of continental ice-sheet evolution itself. However, this model has the large number of parameters, many of which are quite well known (Table 1), but many of which, that we will refer to as "ensemble parameters", are known or expected only to lie within a given range on a-priori grounds (Table 2).

Table 1. Model Parameters

Definition	Parameter	Value
earth radius	r_e	6370 km
earth mass	m_e	5.976×10^{24} kg
lithospheric thickness	L_e	100 km
latent heat of fusion	L	3.35×10^5 J kg^{-1}
ice density	ρ_i	910 kg m^{-3}
ice specific heat capacity	$c_i(T)$	(152.5 + 7.122.T) J kg^{-1} K^{-1}
ice thermal conductivity	$k_i(T)$	9.828.exp(-0.0057.T) W m^{-1} K^{-1}
bedrock density	ρ_b	3300 kg m^{-3}
bedrock specific heat capacity	c_b	1000 J kg^{-1} °C^{-1}
bedrock thermal conductivity	kb	3 W m^{-1} °C^{-1}
standard deviation, PDD model	σ	5.2°C
standard deviation, accumulation model	σ_p	σ – 1°C
number of ice thermodynamic levels	nz_i	65
number of bed thermodynamic levels	nz_b	5
longitudinal ISM grid resolution	Δφ	1.0^o
latitudinal ISM grid resolution	Δθ	0.5^o

Table 1. Model Parameters

Definition	Parameter	Value
Weertman sliding law rate factor	k_s	$2. \times 10^{-13}$ Pa^{-3} m^2 yr^{-1}
Glen flow law constant, T < - 10°C	B_{gc}	1.14×10^{-5} Pa^3 yr^{-1}
Glen flow law constant, T > -10°	B_{gw}	5.47×10^{10} Pa^3 yr^{-1}
Flow law enhancement factor	E	6.5
creep activation energy of ice, T < -10°C	Qc	6×10^4 $Jmol^{-1}$
creep activation energy of ice, T > -10°C	Qc	1.39×10^5 $Jmol^{-1}$
Glen flow law exponent	n	3

Table 2. Ensemble Parameters

Definition	Parameter	Range
till viscosity	μ_O	$1.1 \times 10^9 \rightarrow 4.5 \times 10^{10}$ Pa s
maximum calving velocity	U_{Cmx}	0.4 → 2.6 km/yr
high-temperature calving cut-in	T_{Chi}	-18 → 0°C
regional northwestern maximum calving velocity	U_{CNWmx}	0.2 → 1.8 km/yr
global LGM precipitation scale factor	f P	0.8 → 1.8
Western Canada precipitation factor	f P_W	1.0 → 3.5
South Central precipitation enhancement factor	RP_{SM}	1.8 → 3.4
Precipitation phase factor	fn P dexp	0.4 → 1.6
pre –30kyr desert-elevation cutoff	desO	0.7 → 2.1 km
post –30kyr western desert-elevation cutoff	desW	2.5 → 4.5 km
post –30kyr north-western desert-elevation cutoff	desNW	0. → 2. km
post –30kyr north-central desert-elevation cutoff	desNC	0. → 2. km
post –30kyr central desert-elevation cutoff	desC	0. → 2.2 km
post –30kyr remainder desert-elevation cutoff	des2	1.4 → 2.4 km
2 LGM precipitation-evaporation EOF components	fPEOF[2]	150% of PMIP range
global LGM temperature scale factor	fnT	0.8 → 1.3
3 LGM temperature EOF components	fTEOF[3]	150% of PMIP range

The sequence of steps involved in the Bayesian calibration the UofT GSM is illustrated on Figure 10. The first step in this process involves the computation of a very large “ensemble” of full glacial cycle integrations. In this step each successive member of the ensemble is determined by randomly selecting values for the parameters listed in Table 2 from within the a-priori specified range of each. The results from the ensemble of integrations so produced, which includes on the order of 1000 members, are employed in the second step of the analysis procedure to “train” a neural network. Once trained, this neural network can be employed as a statistical emulator capable of producing results that mimic those produced by the complete

UofT GSM. With the statistical emulator it is possible to construct a very large data set of results consisting of the equivalent of a million or more individual integrations of the GSM. The third step in the complete Bayesian training procedure involves the application of Markov Chain Monte Carlo methods to place error bars on the parameters of the GSM which lead to successful fits to the observational constraints. This entire procedure is pursued iteratively, eventually resulting in an ensemble of successful models that may differ from one another significantly because of the "trade-offs" that are allowed between the various parameters of the model.

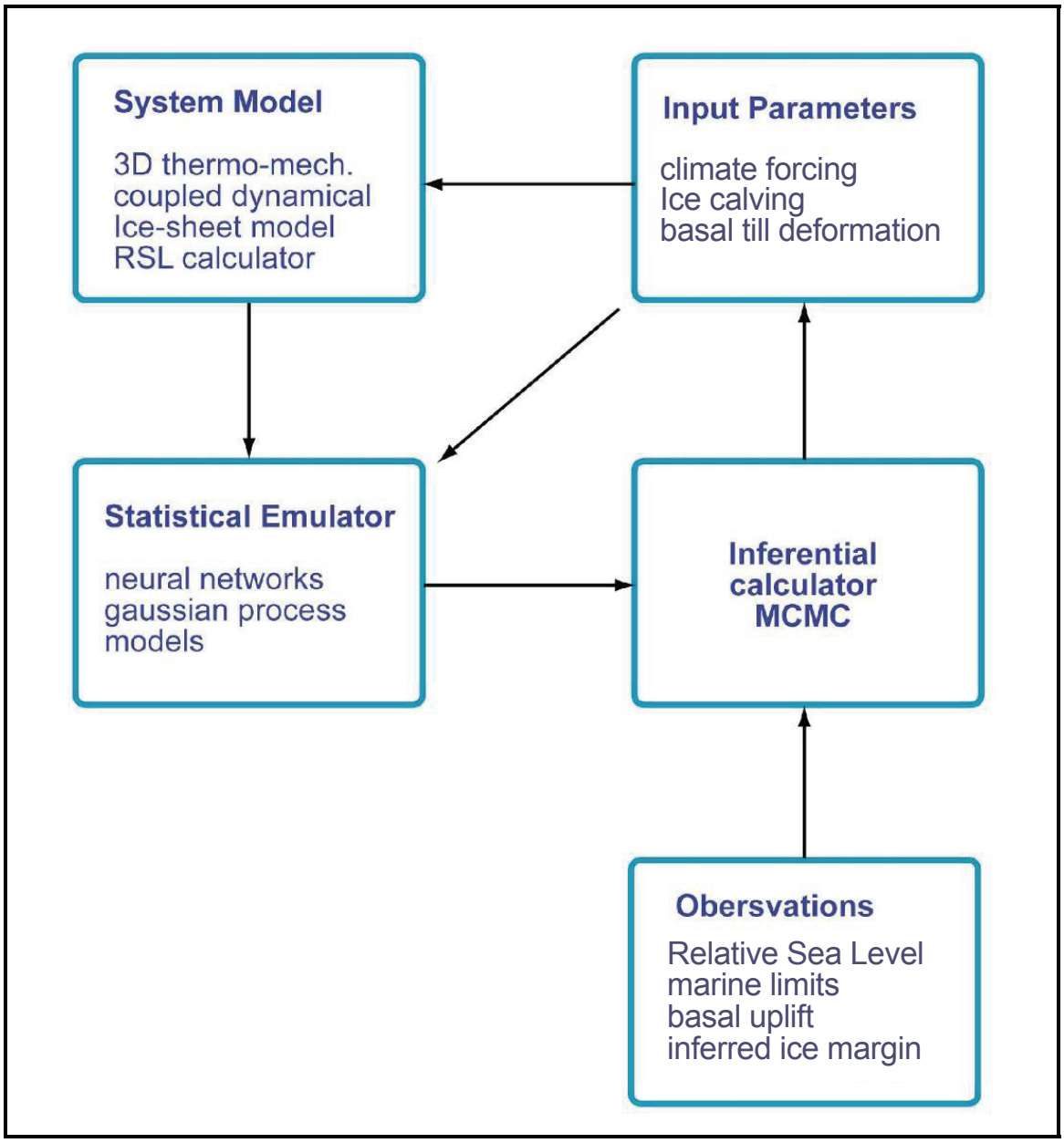

Figure 10. Illustration of the data flow involved in a complete Bayesian calibration of the glacial systems model of Laurentide Ice Sheet evolution. (See the text for a discussion of the details)

4. DATA SETS FOR THE ANALYSIS OF L&ILW REPOSITORY PERFORMANCE

4.1 Choosing the Set of Representative Models from the Ensemble

The data set of model results to be discussed in the next section of this report consists of examples of both the continental scale characteristics of representative models as well as time series of the evolution of a number of specific model predictions at a particular target location. This report focuses upon the description of eight (8) models that span the apparent range of model characteristics that provide acceptable fits to the totality of the observational constraints. These eight (8) models are assigned individual numbers as follows:

9828 – VM2 - from Tarasov and Peltier (2007)
9880 – VM2 - from Tarasov and Peltier (2007)
9921 – VM2 - highest resolution permafrost – new
9930 – VM2 - highest resolution permafrost – new
9834 – VM4_1 - replicate of a T/P (2007) run with new viscosity
9857 – VM4_1 - replicate of a T/P (2007) run with new viscosity
9904 – VM4_1 - replicate of a T/P (2007) run with new viscosity
9940 – VM4_1 - highest resolution permafrost – new

The first four (4) members of this set of eight models have been optimized on the basis of the assumption of a radial profile of mantle viscosity denoted VM2 whereas the final four have been optimized on the basis of a profile denoted VM4_1. These profiles are illustrated on Figure 11 and have been inferred on the basis of fits to characteristics of ^{14}C dated relative sea level histories that are relatively insensitive to the details of glacial history (i.e., see Peltier 2004 for detailed discussion of the solution of the inverse problem for mantle viscosity that delivered the VM2 model). Model VM4_1 differs from model VM2 only in the viscosity of the upper part of the lower mantle where VM4_1 is slightly "softer" than VM2 meaning that the GIA process will be characterized by a slightly shorter relaxation time than in the VM2 model. The models with numbers in the range 9921-9940 employ the highest resolution bed/permafrost model and include strong ice volume constraints in the MCMC sampling at -49 kyrs and -30 kyrs based upon the Peltier and Fairbanks (2006) sea level record from the island of Barbados. The older runs numbered 9801-9920 are from the ensemble published in Tarasov and Peltier (2007) except that the set now includes a VM4_1 replicate. These analyses did not employ pre-LGM ice volume constraints in the MCMC sampling.

The relative quality of the individual models in the set of eight may be described by a quantitative measure of misfit to a range of different constraints. Among the most important of these constraints are the following:

1. The entire relative sea level data base of A.S. Dyke for the North American continent.
2. The data base on the height of the marine limit at sites surrounding Hudson Bay, also from A.S. Dyke of the Geological Survey of Canada.
3. Observations of the present day rate of uplift of the crust at Yellowknife and from the sequence of absolute gravity measurement sites that extend from Churchill across the Canadian border into Iowa as discussed in Lambert et al. (2001).
4. The magnitude of the margin forcing of precipitation required to enable the model to fit the time-dependent margin chronology of A.S. Dyke et al. (2002).

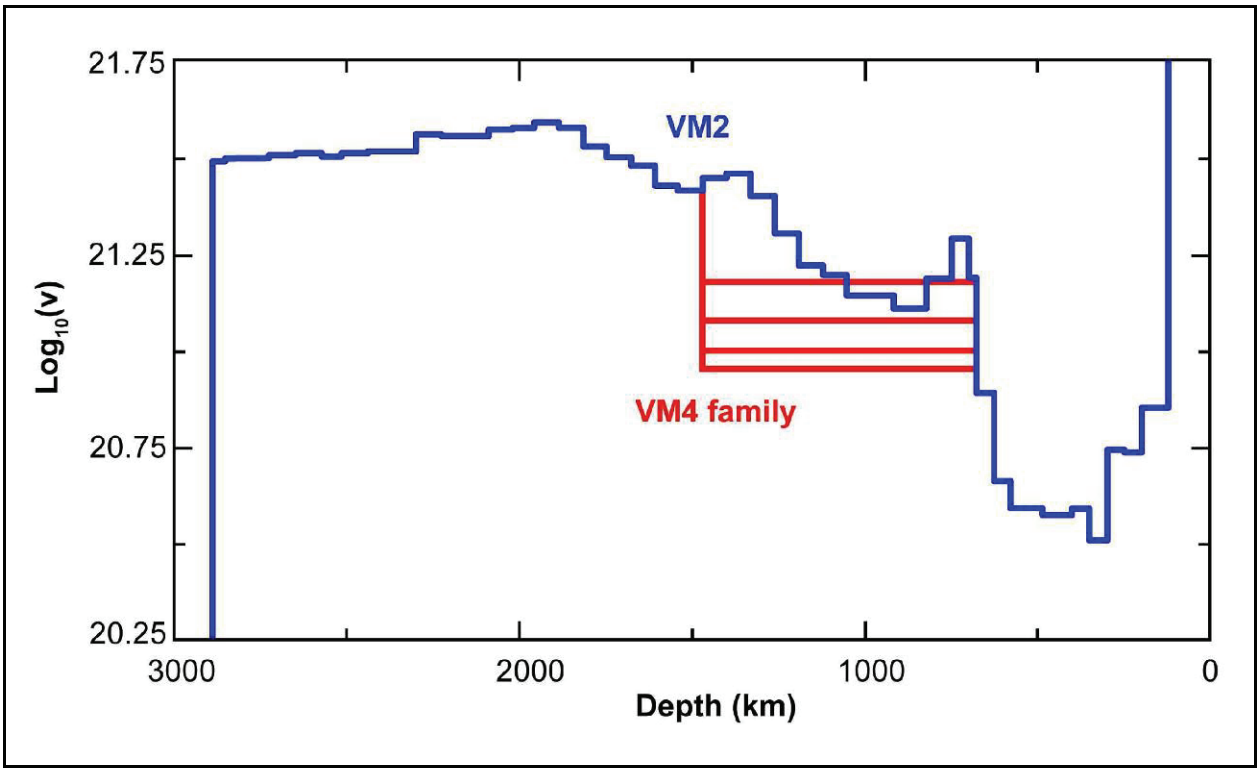

Figure 11. Inter-comparison between the radial viscosity structure of the VM2 model and other models, including those in the VM4 family. The VM4_1 model is the member of the latter family in which the viscosity in the upper part of the lower mantle is equal to 10^{21} Pa s.

The scoring of the fits to relative sea level and marine limit data is based upon summed mean square errors (taking into account the observational uncertainties). These misfits are also weighted by the inverse of the geographical data point density with additional weighting for the important south-east Hudson Bay location where the quality of the relative sea level data is especially high. The following are lists of selected aggregate misfit scores (smaller is better) for the set of numbered models for which detailed results are presented:

Main Aggregate Misfit score that isolates best models

9921 – 0.8782
9940 – 0.7946
9930 – 0.7158

Aggregate misfit scores when the weighting of the importance of RSL data is doubled:

9921 – 0.9546
9940 – 0.8386
9930 – 0.8141

This demonstrates that doubling the weighting on the RSL data leads to some degradation of the quality of the overall fit.

Aggregate misfit scores when the pre-LGM ice volume constraints are relaxed:

9857 – 1.0807
9904 – 1.0568
9921 – 0.9329
9834 – 0.8896
9940 – 0.8183
9930 – 0.7427
9829 – 0.7099
9880 – 0.7029

Aggregate scores when this set of models is re-run with double RSL weighting

9904 – 1.0765
9921 – 1.0005
9834 – 0.9823
0857 – 0.9447
9828 – 0.8586
9940 – 0.8503
9880 – 0.8471
9930 – 0.8284

This set demonstrates that the aggregate misfit is again degraded when additional weight is placed upon the relative sea level data.

4.2 Continental Scale Evolution of Selected Model Fields

In order to illustrate the predictions of representative models in this set from a continental scale perspective, two of the best models from the perspective of aggregate misfit will be compared, namely those numbered 9921 and 9930, both of which are based upon the assumption of the VM2 radial viscosity profile and both of which employ the highest resolution treatment of permafrost development. In this section, based upon graphics presented in Appendix A, brief description will be provided of the full glacial cycle evolution of ice-thickness, of surface temperature (relative to the pressure point in ice-covered regions), of permafrost depth, and of the change in basal surface elevation relative to the current height above sea level. Hereafter follow brief discussions of the continental scale data sets presented in Appendix A.

The continental scale ice thickness data sets demonstrate that large differences exist between models 9930 and 9921 at t = -110 kyr. Recall from Section 2 of this report that the most recent glaciation event began at approximately -116 kyr when the summertime seasonal insolation anomaly due to Earth's orbit was most strongly negative. At -110 kyr model 9930 has ice-cover that has already expanded across the Great Lakes region from the nucleation zone on the islands in the Queen Elizabeth archipelago and Baffin Island. On the other hand, the ice-cover in model 9921 at

the same time is considerably less extensive with the Cordilleran and Laurentide sheets still disconnected and the southern margin of the Laurentide sheet located well to the north of James Bay. South of this ice-margin there exists a sequence of well developed pro-glacial lakes. At t = -100 kyr the ice-cover in both models has retreated significantly to the north but model 9930 has a trapped pro-glacial lake that is separated from the sea that more than encompasses the current Hudson Bay. In model 9921, on the other hand, a similar region of water cover exists but this is connected to the ocean (note that in these graphics proglacial lakes are coloured light blue whereas regions covered by ocean water are coloured dark blue). By -90 kyr the ice-cover in both models has once more expanded to the south under the influence of the changing orbital insolation regime. Again model 9930 has more extensive ice-cover than model 9921 and the Laurentide and Cordilleran complexes are connected whereas in model 9921 they are not. By -60 kyr, however, the ice-covered area in the two models has converged although the thickness of the ice-cover in model 9921 is much greater than in model 9930 (note the numbers on the thickness isopachs). By -40 kyrs the models have again diverged with model 9930 having much more extensive ice cover than model 9921. By LGM at -20 ky when the ice-margin information from the compilation of A.S. Dyke first becomes available as a constraint, the ice-covered areas of the two models become essentially identical although the interior Keewatin Dome in model 9921 is somewhat greater in terms of ice-thickness than it is in model 9930 although the difference is slight. By -15 kyr, however, significant differences have developed with model 9921 having very distinct domes of ice in both the Keewatin sector of the Shield and over James Bay whereas neither of these features exist in model 9930. At -10 kyr, however, the Keewatin Dome has reappeared in model 9930. At this time both models have significant proglacial lakes along their southern margins.

The ice-sheet basal and land surface temperature data sets for these models reflect the significant differences between the evolution of their thickness histories. On each frame of the evolving basal temperature map the red line denotes the position of the instantaneous ice-margins. The important point to note on these maps is the dividing line at 0°C on the colour bar that distinguishes between temperature and frozen basal conditions. By inspection of the evolution of the basal (surface) temperature fields for these models, it will be clear that the surface of the Earth beneath the ice is often temperate whereas the surface to the south of the ice-covered region is often below freezing and therefore liable to be characterized by the existence of a finite thickness of permafrost. By LGM at -20 kyr both models have extensive regions within their southern margins in which the basal temperature is above freezing and in which free water is being generated by basal melting. These are the conditions during which eskers form by the flow of sub-glacial meltwater out from under the ice-sheet into the peripheral region. The surface temperature prediction for present day is consistent with that of the modern reanalysis data set and is identical for both models.

Inspection of the maps of permafrost depth provided in Appendix A, demonstrate very clearly the manner in which this important field tracks the evolution of surface temperature. The fit of these data to the known distribution of permafrost over the Canadian landscape at present is excellent, with the northwest to southeast trend of the southern boundary and the prediction of permafrost depths reaching 800 m in the high Arctic region.

The final set of maps provided in Appendix A is for the change in basal elevation with time beginning with the onset of glaciation at -116 kyr. By LGM at -20 kyr maximum surface depressions of the crust on the order of 1 km are achieved over the regions of heaviest ice-cover. That vertical crustal displacements on this order are to be expected follows immediately from the deflection that would be required in order that the Archimedes force of buoyancy be sufficient to balance the weight of the load. Given that the ratio of the density of ice to that of the Earth's crust is about 1/3 and that the maximum thickness of the ice that is reached by LGM

is approximately 3600 m (see the ice thickness maps discussed previously) a surface deflection of approximately 1 km is precisely what is expected on the simplest physical grounds.

4.3 Time Series Data Relevant to the Subsurface Hydrological Regime

The time series data to be presented in this section of the report for the eight (8) models that have been selected to illustrate the range of possibilities for the impact of a glacial cycle upon the location of a repository for L&ILW are for several different characteristics. These will include normal stress, basal (surface) temperature, permafrost depth, meltwater generation, depth of proglacial lakes, and the extent of crustal depression or uplift. As a first example of such time series, however, it is useful to consider a measure of the integrated mass of the entire ice-complex as it evolves through time. Figure 12 shows these time series for the eight models in our set in terms of the variation of eustatic (globally averaged) sea level to which their advance and retreat gives rise. Inspection of these results will demonstrate that, although there exist large differences between these models during the period prior to LGM at approximately -20 kyr, at LGM itself the mass of this reasonably successful set of glacial histories is equivalent to a drop in mean sea level of approximately 80-90 m, in accord with the requirements of the new Barbados data set of Peltier and Fairbanks (2006). Also evident from Figure 12 is that each evolutionary history of the North American ice-sheet complex is characterized by three (3) main phases of advance and retreats within the 100 kyr cycle, a characteristic due to the important role that orbital obliquity forcing plays in controlling the growth and decay of ice-cover (see Section 2 of this report for detailed discussion).

4.3.1 Normal Stress

The normal stress at the site due to the weight of the overlying ice-cover is shown for the eight (8) models on Figure 13. This is consistent with the general form of the integrated ice-volume curves in Figure 12 in the sense that they are each dominated by the existence of three phases during which the normal stress rises above zero due to the site being over ridden by an ice-sheet advance during these periods. By the time of greatest ice volume at LGM, the normal stress for most models has risen to a value of approximately 25 MPa as expected on the basis of the sample ice-thickness data provided in Appendix A at continental scale. Southern Ontario locations all lie within the southern boundary of ice-sheet extent when the ice-sheet is near its large volume limit. It is because of this location with respect to ice-margin that the processes that would be expected to occur in this area in the event of a renewed glaciation event are so strongly time dependent.

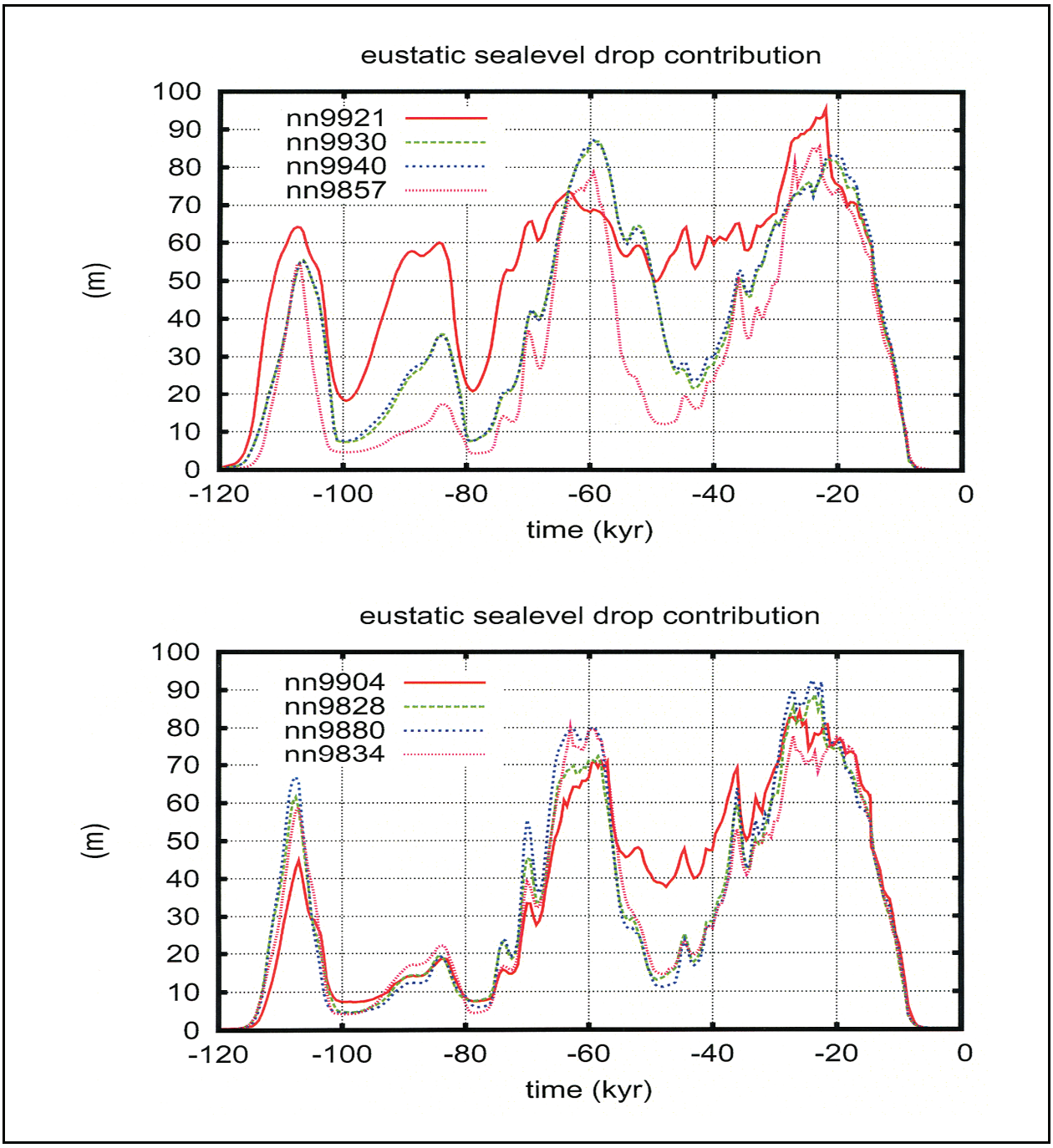

Figure 12. Eustatic sea level variations for the series of 8 models of the North American continental glaciation- deglaciation cycle on the basis of which predictions are made in this report of the local temporal histories of aspects of the ice-age cycle that would be expected to impact the performance of a repository for L&ILW. These time series describe the time dependent decrease of mean sea level that would be caused by the growth and decay of the ice-sheet in each of these simulations. Notable is the fact that the deglaciation phase of the cycle is much more highly constrained than is the glaciation phase.

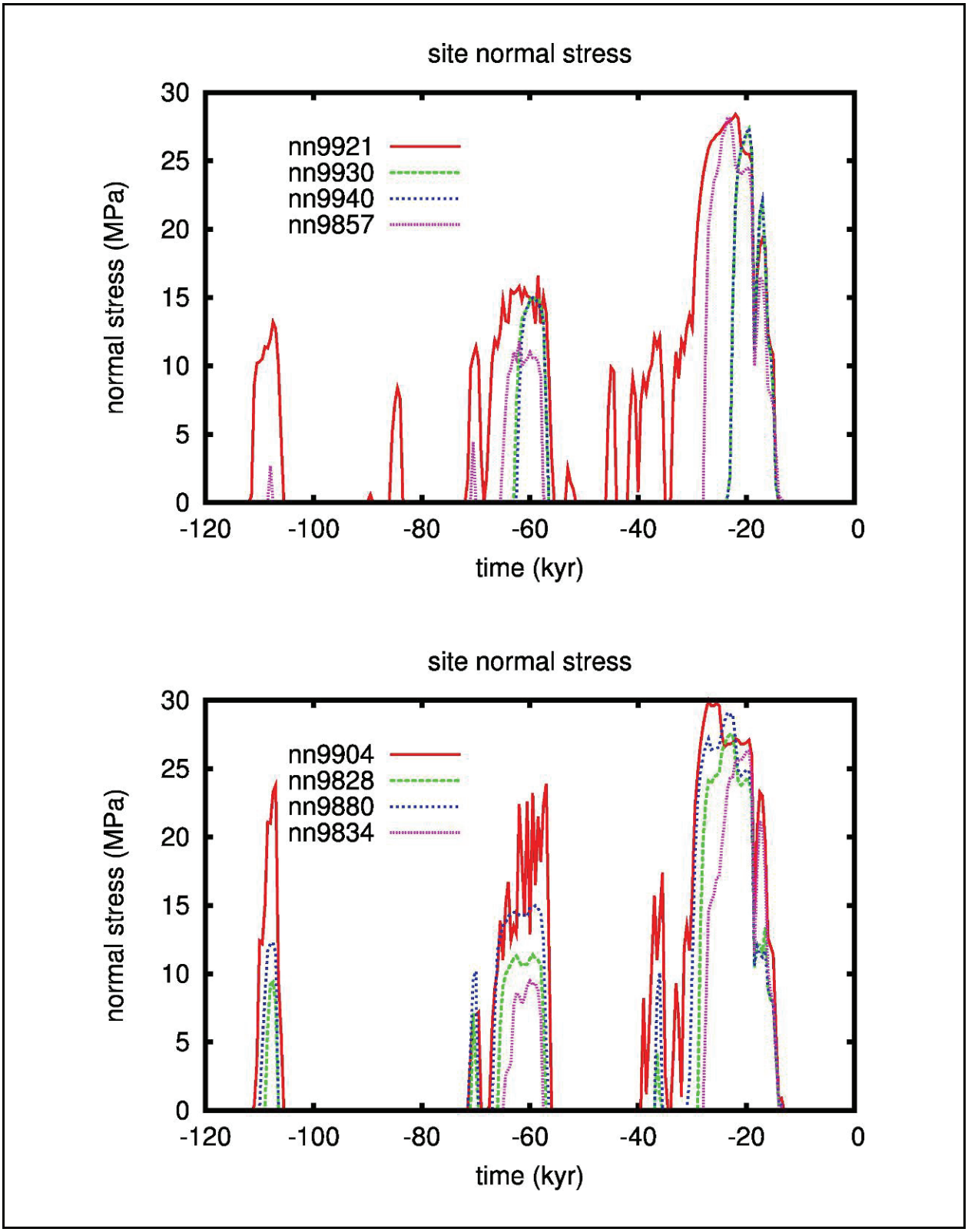

Figure 13. Normal stress at the surface of the Earth at the repository site.

4.3.2 Basal (Surface) Temperature

The time series results for basal (surface) temperature are shown on Figure 14 for the set of eight (8) illustrative and representative models. Immediately evident by inspection of this figure is the fact that the temperature at the site falls dramatically during the first expansion phase of the continental ice-sheet. After this initial decrease the temperature remains low for the majority of the 100 kyr cycle, rising to modern levels only following the final deglaciation phase of the cycle. By comparing the results for normal stress with these results for surface temperature, it will be clear that only for relatively short intervals of time at this site do temperate conditions exist beneath the ice-sheet when it covers the region. These times are marked by periods when the temperature is precisely equal to zero degrees Centigrade because during these periods all of the heat that continues to enter the base of the ice-sheet is expended in melting ice.

4.3.3 Permafrost Depth

The variations of permafrost depth through time for the eight (8) illustrative models are displayed on Figure 15. Comparison of these data with those for site normal stress will demonstrate that this field is much more strongly time dependent than that determined by the weight of the overlying ice. Furthermore, the depth to which permafrost extends is predicted to very seldom exceed a few tens of metres. Also notable is the fact that permafrost is effectively absent at the I&ILW site during the LGM epoch when the ice-cover is thickest and basal meltwater production at its greatest.

4.3.4 Meltwater Generation

Basal meltwater production rates for the eight (8) models are graphically displayed on Figure 16. As with the permafrost data, the meltwater production data are highly time dependent with intervals of production interspersed with intervals in which no melting is occurring. Careful intercomparisons of these data with those for permafrost depth will demonstrate, as is required on physical grounds, that permafrost is absent when meltwater is being produced and vice-versa.

4.3.5 Depth of Pro-Glacial Lakes

Pro-glacial lake depth at the site for each of the eight (8) illustrative models is presented on Figure 17. Most notable by examination of these data for most models is that subsequent to LGM, during the phase of ice-sheet retreat, the site becomes entirely inundated by a pro-glacial lake whose depth may exceed 400 m at sites in Manitoba within the glacial Lake Agassiz region. This is entirely unsurprising as the thickness of the ice-cover is such as to have depressed the crust locally by an amount of the same order. As the rebound of the crust proceeds following removal of the ice-load the water recedes into the depressions that hold the present Great Lakes. This clearly constitutes a profound, if transient, modification of the surface hydrological regime. As discussed in Tarasov and Peltier (2006), the depths of the lakes predicted by these analyses fit well with those inferred on the basis of geological inferences.

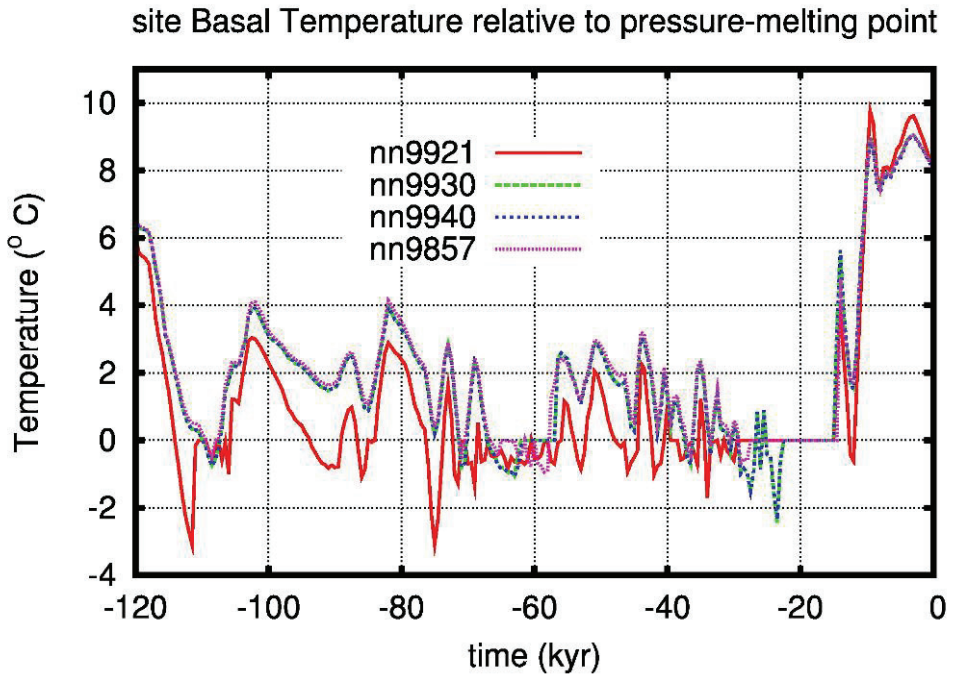

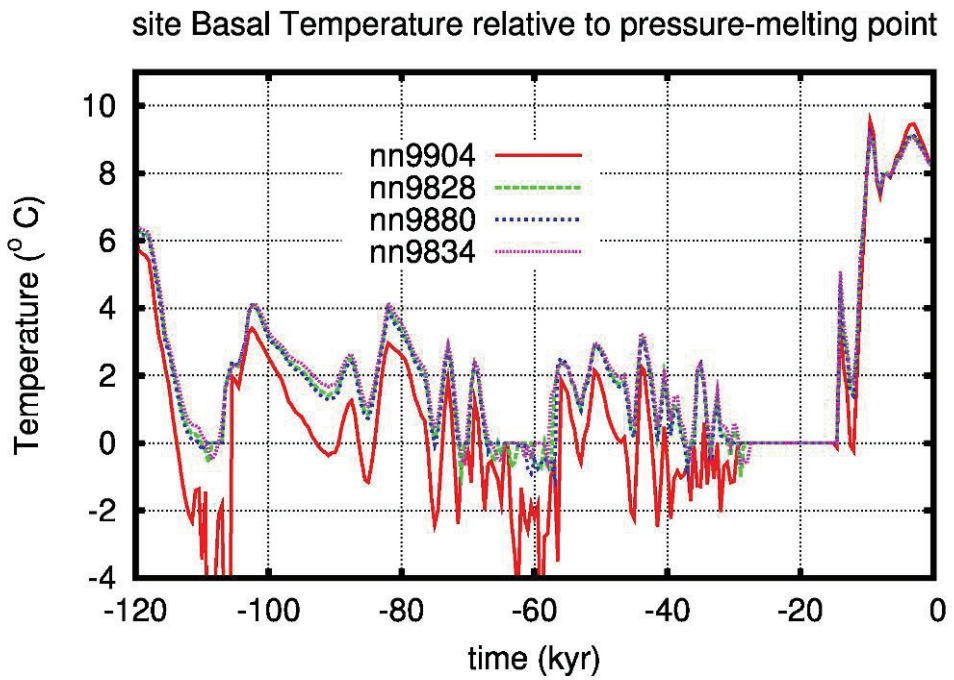

Figure 14. Basal temperature relative to the pressure melting point at the surface of the solid Earth at the repository site.

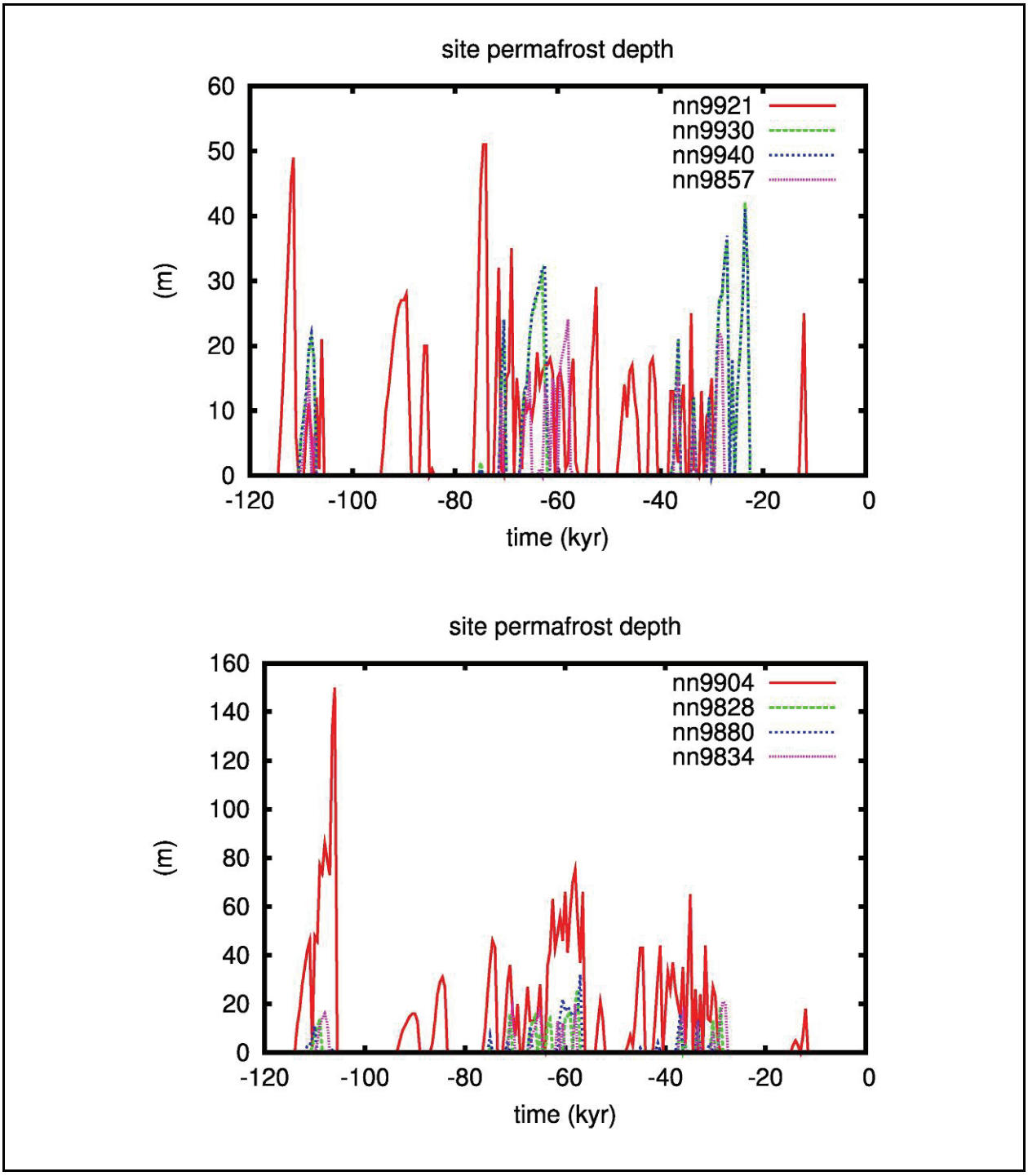

Figure 15. Permafrost depth at the site through the ice-age cycle at the repository location. Note that there are occasions during which a lens of permafrost becomes trapped at depth in some of these models at certain times. This effect is captured in the numerical data sets provided in the accompanying Bruce data set where depths computed from above and from below are provided. When the latter is not equal to the former a trapped lens is present.

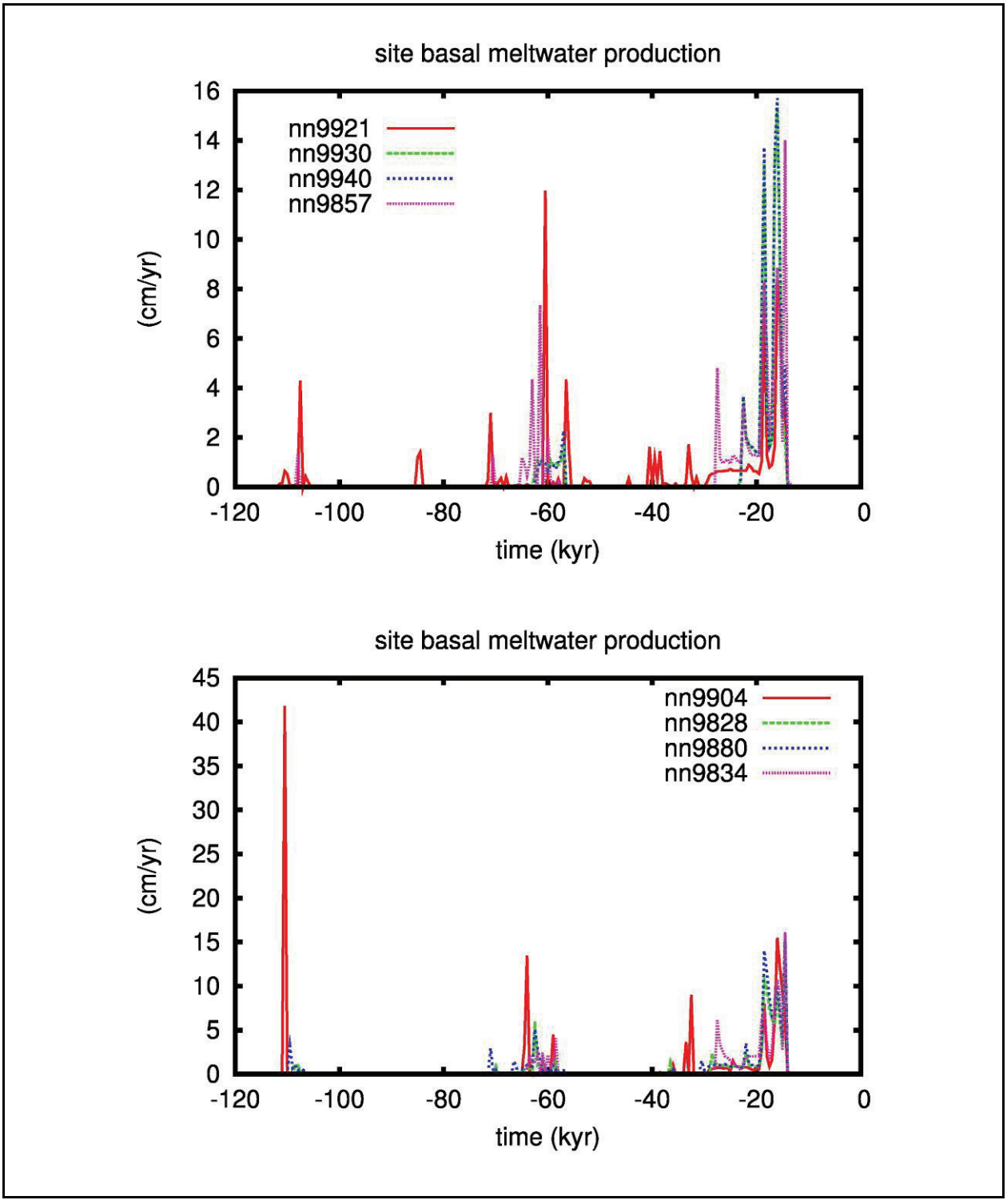

Figure 16. Basal meltwater production at the site as a function of time through the ice-age cycle.

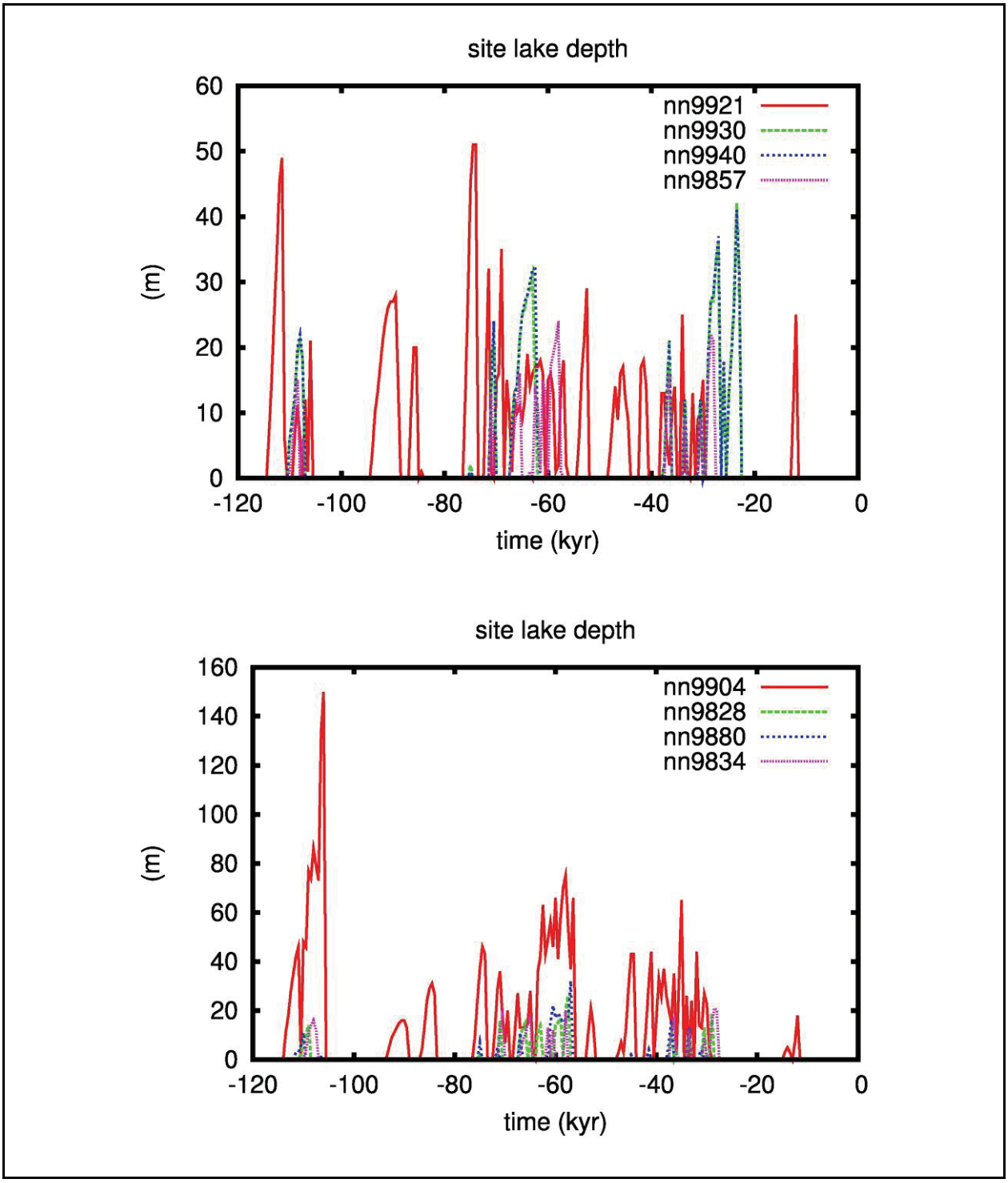

Figure 17. Proglacial lake depth at the site as a function of time through the glacial cycle.

4.3.6 Crustal Depression and Uplift

Time series data for the changing elevation of the surface at the site relative to present day sea level are presented in Figure 18. Comparing these time series with those for normal stress will show that all models are characterized by three significant episodes of crustal depression that coincide with the epochs of high normal stress when the ice-cover at the site is most significant. Maximum crustal depressions from the equilibrium level occur at LGM and reach values in excess of 500 m. This is consistent with the development of proglacial lake depths of order 300-400 m at the site following deglaciation as discussed above.

5. SUMMARY

The purposes of this report have been to review the current state of understanding of the processes of Long Term Climate Change related to glaciation processes on the one hand, and to employ a state-of-the-art model of continental scale glaciation to make specific predictions of what such an event would imply for the safety of a repository for L&ILW on the other. In Section 2 of the report, the current literature on the related issues of Long Term Climate Change and glaciation was reviewed. It was pointed out therein that the explanation of the recurrent sequence of glaciation events during the Late Quaternary period is now widely understood to be caused by the so-called “Milankovitch effect”. Small changes in effective solar insolation caused by the changing geometry of Earth’s orbit around the Sun are highly significant and have been such as to induced new continental scale glaciation events to recur on a timescale of approximately 100,000 years. In each such glacial cycle the glaciation phase has lasted approximately 90,000 years and the deglaciation phase approximately 10,000 years.

If a reglaciation of the Canadian land mass should occur again in the future, such an event is most likely to begin in approximately 60,000 years from present. If at that time the concentration of carbon dioxide and other greenhouse gases in the atmosphere were similar to the present concentration, however, it is unlikely that a renewed episode of glaciation could occur as the increased surface warmth would mitigate against it. Since our ability to predict the CO_2 level that will exist at a time so far into the future is negligible, we cannot discount this possibility and must therefore take it into account when developing the safety case for an L&ILW repository. The analyses presented in this report have included detailed predictions of the boundary conditions that such a repository would be subjected to as a consequence of such an event.

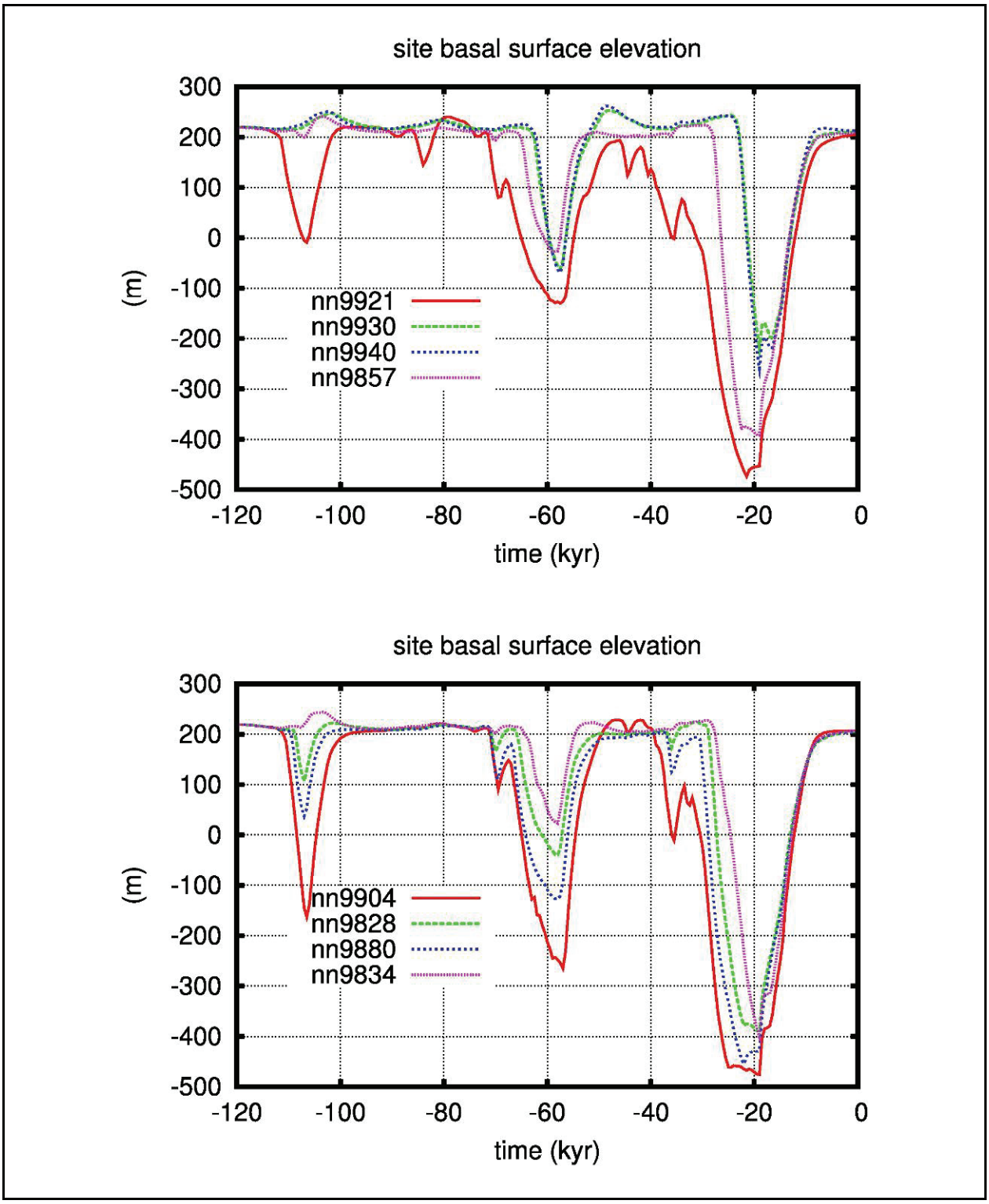

Figure 18. Deflection of the surface of the solid Earth below its equilibrium level at the site during the glacial cycle in each of the 8 representative models.

6. REFERENCES

Baksi, A.K. 1992. $^{40}Ar/^{39}Ar$ dating of the Brunhes-Matuyama geomagnetic field reversal. Science 256, 356-359.

Bauder, A., D.M. Michelson and S.J. Marshall. 2005. Numerical modeling investigations of the sub-glacial conditions of the southern Laurentide ice sheet. Ann. Glaciol. 40, 219-224.

Braithwaite, R.J. 1995. Positive degree-day factors for ablation on the Greenland ice sheet studied by energy-balance modeling. J. Glaciol. 41 (137), 153-160.

Clark, P.U. 1994. Unstable behaviour of the Laurentide Ice Sheet over deforming sediment and its implications for climate change. Quat. Res. 41, 19-25.

Deblonde, G. and W.R. Peltier. 1991. Simulations of continental ice-sheet growth over the last glacial-interglacial cycle: Experiments with a one-level energy balance model including realistic geography. J. Geophys. Res. 96, 9189-9215.

Deblonde, G. and W.R. Peltier. 1993. Late Pleistocene ice-age scenarios based upon observational evidence. J. Climate 6, 709-727.

Deblonde, G., W.R. Peltier and W.T. Hyde. 1993. Simulations of continental ice sheet growth over the last glacial-interglacial cycle: Experiments with a one level seasonal energy balance model including seasonal ice albedo feedback. Glob. And Planet. Change 98, 37-55.

Dyke, A.S. and V.K. Prest. 1987. Late Wisconsinan and Holocene history of the Laurentide Ice Sheet. Geogr. Phys. Quat. 41, 237-264.

Dyke, A.S., J.T. Andrews, P.U. Clark, J.H. England, G.H. Miller, J. Shaw and J. Veillette. 2002. The Laurentide and Innuitian ice sheets during the Last Glacial Maximum. Quat. Sci. Rev. 21, 9-31.

Dyke, A.S., A. Moore and L. Robertson. 2003. Deglaciation of North America. Tech. Rep. Open File 1574, Geological Survey of Canada, thirty-two maps at 1:7 000 000 scale with accompanying digital chronological database and one poster (in two sheets) with full map series.

Dziewonski, A.M. and D.L. Anderson. 1981. Preliminary reference Earth model (PREM). Phys. Earth Planet. Int. 25, 297-356.

Fairbanks, R.G. 1989. A 17,000-year glacio-eustatic sea level record: influence of glacial melting rates on the Younger Dryas event and deep-ocean circulation. Nature 342, 637-641.

Hays, J.D., J. Imbrie and N.J. Shackleton. 1976. Variations in the Earth's orbit: Pacemaker of the ice ages. Science 194, 1121-1132.

Huybrechts, P. 1986. A Three Dimensional Time-Dependent Numerical Model for Polar Ice-Sheets: Some Basic Testing With a Stable And Efficient Finite Difference Scheme. Report 86-1.Geografisch Instituut, Vrije Universiteit Brussel, Pleinlaan 2, B-1050 Brussel, Belgium.

Hyde, W.T. and W.R. Peltier. 1985. Sensitivity experiments with a model of the ice-age cycle: the response to harmonic forcing, J. Atmos. Sci. 42, 2170-2188.

Janssens, I. and P. Huybrechts. 2000. The treatment of meltwater retention in mass-balance parameterizations of the Greenland ice sheet. Ann. Glaciol. 31, 133-140.

Jenson, J.W., D.R. MacAyeal, P.U. Clark, C.L. Ho and J.C. Vela. 1996. Numerical modeling of subglacial sediment deformation: implications for the behaviour of the Lake Michigan Lobe, Laurentide Ice Sheet. J. Geophys. Res. 101 (B4), 8717-8728.

Kalnay, E. et al. 1996. The NCEP/NCAR 40-year reanalysis project. Bull. Amer. Met. Soc. 77, 437-471.

Lambeck, K. and J. Chappell. 2001. Sea level change through the last glacial cycle. Science 292, 679-686.

Lambert, A., N. Courtier, G.S. Sasegawa, F. Klopping, D. Winester, T. James and J.O. Liard. 2001. New constraints on Laurentide postglacial rebound from absolute gravity measurements. Geophys. Res. Lett. 28, 2109-2112.

Laske, G. and G. Masters. 1997. A global digital map of sediment thickness. EOS Trans. 78, F483.

Legates, D.R. and C.J. Willmott. 1990. Mean seasonal and spatial variability in gauge-corrected global precipitation. Int. J. Climatol. 10 (2), 111-127.

Licciardi, J.M., P.U. Clark, J.W. Jenson and D.R. MacAyeal. 1998. Deglaciation of a soft-bedded Laurentide Ice Sheet, Quat. Sci. Rev. 17, 429-448.

Ling, F. and T. Zhang. 2004. A numerical model for surface energy balance and thermal regime of the active layer and permafrost containing unfrozen water. Cold Reg. Sci. and Tech. 38, 1-15.

Marshall, S.J. and P.U. Clark. 2002. Basal temperature evolution of North American ice sheets and implications for the 100-kyr cycle. Geophys. Res. Lett. 29, 2214, doi:10.1029/2002 GL015, 192.

Marshall, S.J., L. Tarasov, G.K.C. Clarke and W.R. Peltier. 2000. Glaciology of Ice Age cycles: Physical processes and modelling challenges. Can. J. Earth Sci. 37, 769-793.

Milankovitch, M. 1920. Théorie mathématique des phénomènes thermique produits par la radiation solaire (Mathematical Theory of the Heat Phenomena Produced by Solar Radiation), Gauthier-villar, Paris.

Mottaghy, D. and V. Rath. 2006. Latent heat effects in subsurface heat transport modelling and their impact on palaeo temperature reconstructions. Geophys. J. Int. 164, 236-245.

Payne, A.J., et al. 2000. Results from the EISMINT model intercomparisons: the effects of thermomechanical coupling. J. Glaciol. 46 (153), 227-238.

Peltier, W.R. 1974. The impulse response of a Maxwell Earth. Rev. Geophys. 12, 649-669.

Peltier, W.R. 1976. Glacial isostatic adjustment II: The inverse problem. Geophys. J.R. astr. Soc. 46, 669-706.

Peltier, W.R. 1994. Ice age paleotopography. Science 265, 195-201.

Peltier, W.R. 1996. Mantle viscosity and ice age ice sheet topography. Science 273, 1359-1364.

Peltier, W.R. 1998. Postglacial variations in the level of the sea: implications for climate dynamics and solid-earth geophysics. Rev. Geophys. 36, 603-689.

Peltier, W.R. 2002a. Global glacial isostatic adjustment: Paleo-geodetic and space-geodetic tests of the ICE-4G (VM2) model. J. Quat. Sci. 17 (5-6), 491-510.

Peltier, W.R. 2002b. On eustatic sea level history, Last Glacial Maximum to Holocene. Quat. Sci. Rev. 21, 377-396.

Peltier, W.R. 2002c. A Design Basis Glacier Scenario. Report Number 06819-REP-01200-10069-R01. Ontario Power Generation Inc.

Peltier, W.R. 2005. On the hemispheric origins of the meltwater pulse 1a: Quat. Sci. Rev., Quat. Sci. Rev. 24, 1655-1671.

Peltier, W.R. 2004. Global glacial isostasy and the surface of the ice-age Earth: The ICE-5G (VM2) model and GRACE. Ann. Rev. Earth Planet. Science 32, 111-149.

Peltier, W.R. and R.G. Fairbanks. 2006. Global glacial ice-volume, and Last Glacial Maximum duration, from an extended Barbados sea level record. Quat. Sci. Rev. 25, 3322-3337.

Peltier, W.R., G. Vettoretti and M. Stastna. 2006. Atlantic meriodional overturning and climate response to Arctic Ocean freshening. Geophys. Res. Lett. 38, L06713, doi:10,1029/ 2005GL025251.

Peltier, W.R. 2007. History of Earth rotation. In Chapter 10 of Volume 9 (Earth Evolution), of the Treatise on Geophysics, David Stevenson ed., pp. 243-293. Elsevier Press, Oxford, UK.

Pinot, S., G. Ramstein, S.P. Harrison, I.C. Prentice, J. Guiot, M. Stute, S. Joussaume and PMIP collaborating groups. 1999. Tropical paleo-climates at the Last Glacial Maximum: Comparison of Paleo-climate Modeling Inter-comparison Project (PMIP) simulations and paleo-data. Climate Dyn. 15, 857-874.

Piotrowski, J.A., D.M. Mickelson, S. Tulaczyk, D. Krzyszkiwski and F.W. Junge. 2002. Reply to the comments by G.S. Boulton, K.E. Dobbie, S. Zatsepin on: Deforming soft beds under ice sheets: how extensive were they? Quat. Int. 97-98, 173-177.

Pollack, H.N., S.J. Hurter and J.R. Johnson. 1993. Heat flow from the Earth's interior: Analysis of the global data set. Rev. Geophys. 31, 267-280.

Shackleton, N.J. 1967. Oxygen isotope analysis and Pleistocene temperatures re-addressed. Nature 215, 15-17.

Shackleton, N.J. 2000. The 100,000 year ice-age cycle identified and found to lag temperature, carbon dioxide, and orbital eccentricity. Science 289, 1897-1902.

Smith, M.W. and Riceborough. 2002. Climate and the limits of permafrost: A zonal analysis. Permafrost Periglac. Process. 13, 1-15.

Stokes, C.R. and C.D. Clark. 2001. Paleo-ice streams. Quat. Sci. Rev. 20, 1437-1457.

Tarasov, L. and W.R. Peltier. 1997. Terminating the 100 kyr ice age cycle. J. Geophys. Res. 102 (D18), 21665-21693.

Tarasov, L. and W.R. Peltier. 1999. Impact of thermo-mechanical ice sheet coupling on a model of the 100 kyr ice age cycle. J. Geophys. Res. 104, 9517-9545.

Tarasov, L. and W.R. Peltier. 2002. Greenland glacial history and local geodynamic consequences. Geophys. J. Int. 150, 198-229.

Tarasov, L. and W.R. Peltier. 2003. Greenland glacial history, borehole constraints and Eemian extent. J. Geophys. Res., 108, No. B3, 2143, doi:10.1029/2001JB001731.

Tarasov, L. and W.R. Peltier. 2004. A geophysically constrained large ensemble analysis of the deglacial history of the North American ice sheet complex. *Quat. Sci. Rev.*, 23,359-388.

Tarasov, L. and W.R. Peltier. 2005. Arctic freshwater forcing of the Younger-Dryas cold reversal. Nature 435, 662-665.

Tarasov, L. and W.R. Peltier 2006. A calibrated deglacial chronology for the North American continent: Evidence of an Arctic trigger for the Younger-Dryas event. Quat. Sci. Rev. 25, 659-688.

Tarasov, L. and W.R. Peltier. 2007. The co-evolution of continental ice-cover and permafrost extent over the last glacial-interglacial cycle in North America. J. Geophys. Res.-Surface Processes, vol. 112, P02808, doi:10.1029/2006 JF000681.

Van der Veen, C.J. 2002. Calving glaciers. Prog. Geog. 26 (1), 96-122.

Vettoretti, G. and W.R. Peltier. 2003a. On post Eemian glacial inception I: the influence of summer seasonal temperature bias. *J. Climate* 16, 889-911.

Vettoretti, G. and W.R. Peltier. 2003b. On post Eemian glacial inception II: elements of a cryospheric moisture pump. *J. Climate* 16, 912-927.

Vettoretti, G. and W.R. Peltier. 2004. Orbital insolation and carbon dioxide concentration effects on the process of glacial inception. Quat. Sci. Rev. 23, 499-519.

Vieli, A., M. Funk and H. Blatter. 2001. Flow dynamics of tidewater glaciers: a numerical modelling approach. J. Glaciol. 47 (595-606).

Waelbroeck, C., L. Labyrie, E. Michel, J.-C. Duplessy, J.F. McManus, K. Lambeck, E. Balbon and M. Labrackerie. 2002. Sea-level and deep water temperature changes derived from benthic foraminifera isotopic records. Quat. Sci. Rev. 21, 295-305.

Weertman, J. 1957. On the sliding of glaciers. J. Glaciol. 3, 33-38.

Appendix A

This Appendix contains continental scale graphics describing the evolution of several of the field variables of the University of Toronto Glacial Systems Model (UofT GSM) through a complete 100,000 year glacial-interglacial cycle. The field variables include the following:

1. Ice thickness
2. Basal (surface) temperature
3. Permafrost depth
4. Deflection of the surface of the Earth below its equilibrium level.

These fields are shown for two of the models for which time series data are provided for the Bruce Penninsula, Ontario location in Section 4 of this report. These models are those numbered nn9921 and nn9930. It is important to note that even though these models have similarly low misfit scores, meaning that they provide fits to the available constraints of similar quality, they nevertheless differ from one-another significantly through the glacial cycle.

Appendix A1. Ice Thickness

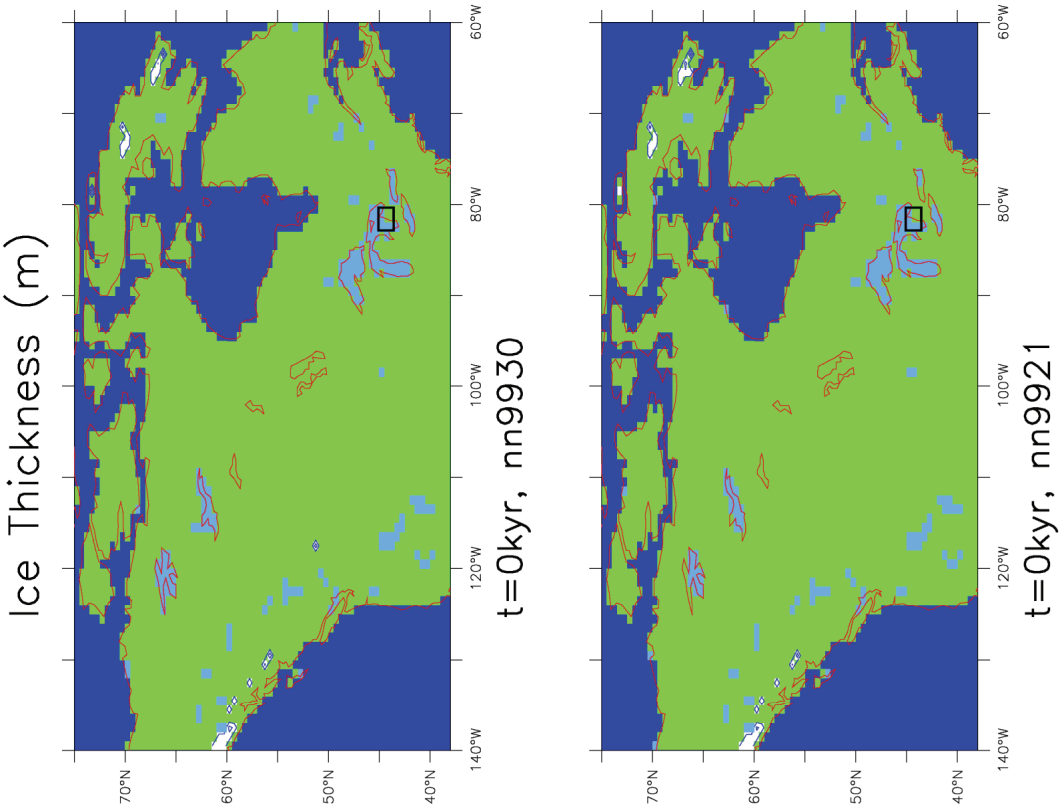
Ice Thickness (m)
t=0kyr, nn9930
t=0kyr, nn9921
70°N
60°N
50°N
40°N
140°W
120°W
100°W
80°W
60°W

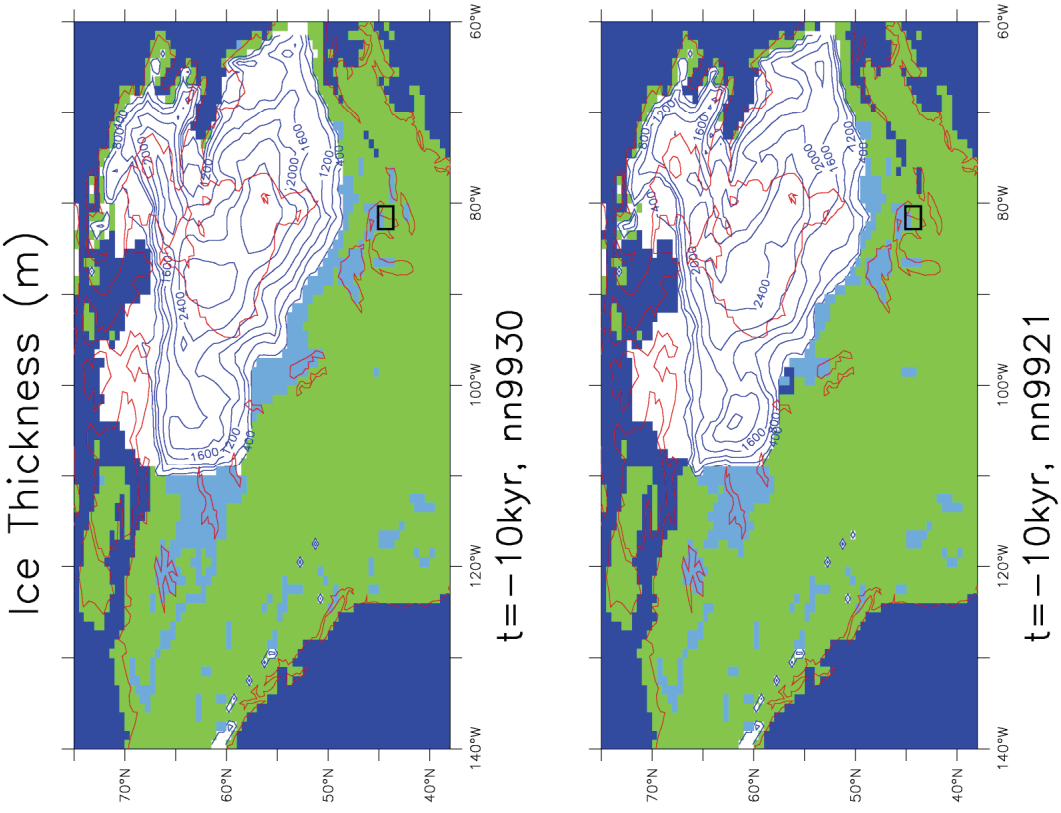
Ice Thickness (m)
t=−10kyr, nn9930
t=−10kyr, nn9921
70°N
60°N
50°N
40°N
140°W
120°W
100°W
80°W
60°W

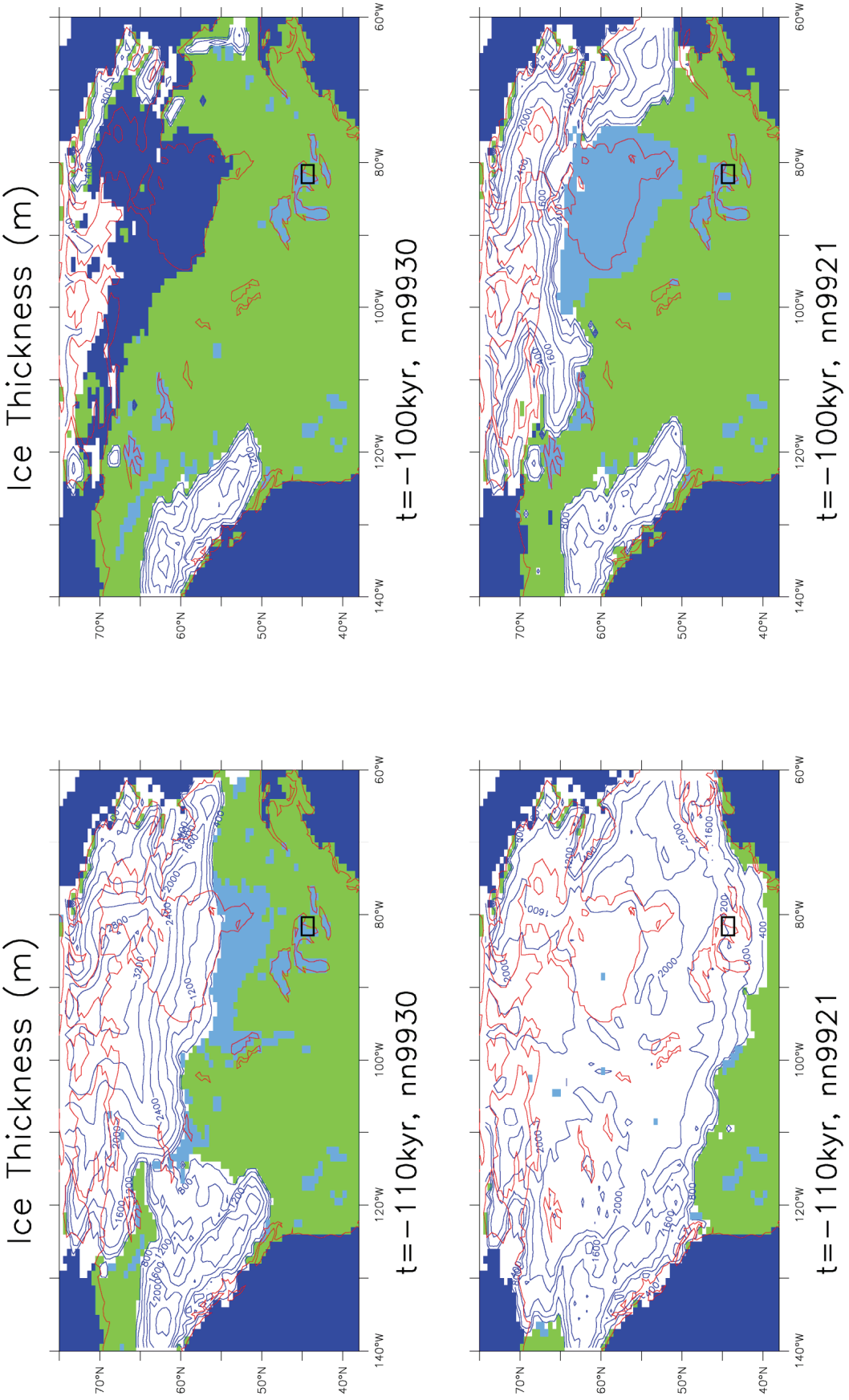
Ice Thickness (m)
t=−100kyr, nn9930
t=−100kyr, nn9921
t=−110kyr, nn9930
t=−110kyr, nn9921
70°N
60°N
50°N
40°N
140°W
120°W
100°W
80°W
60°W

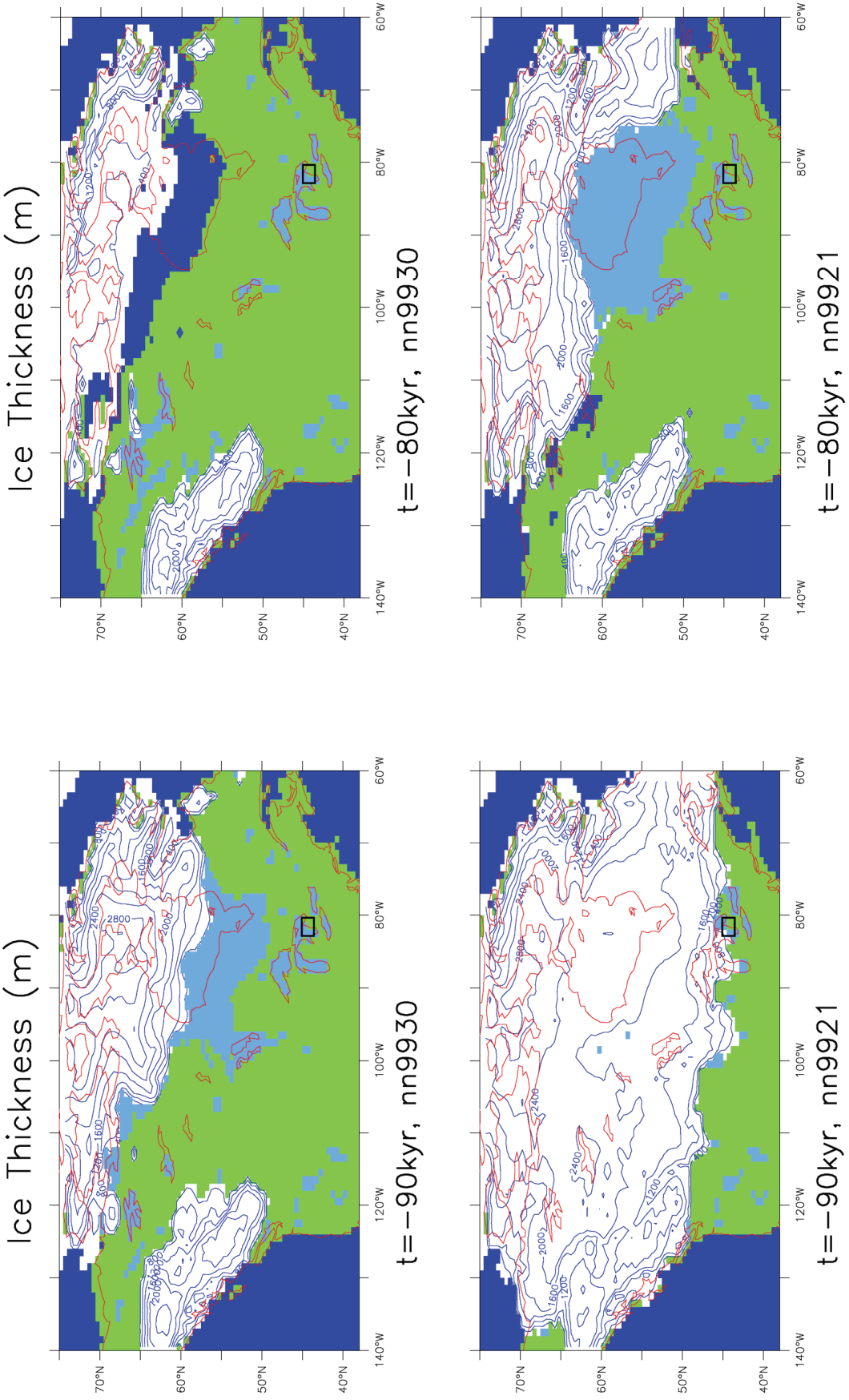
Ice Thickness (m)
t=−80kyr, nn9930
t=−80kyr, nn9921
t=−90kyr, nn9930
t=−90kyr, nn9921
70°N
60°N
50°N
40°N
140°W
120°W
100°W
80°W
60°W

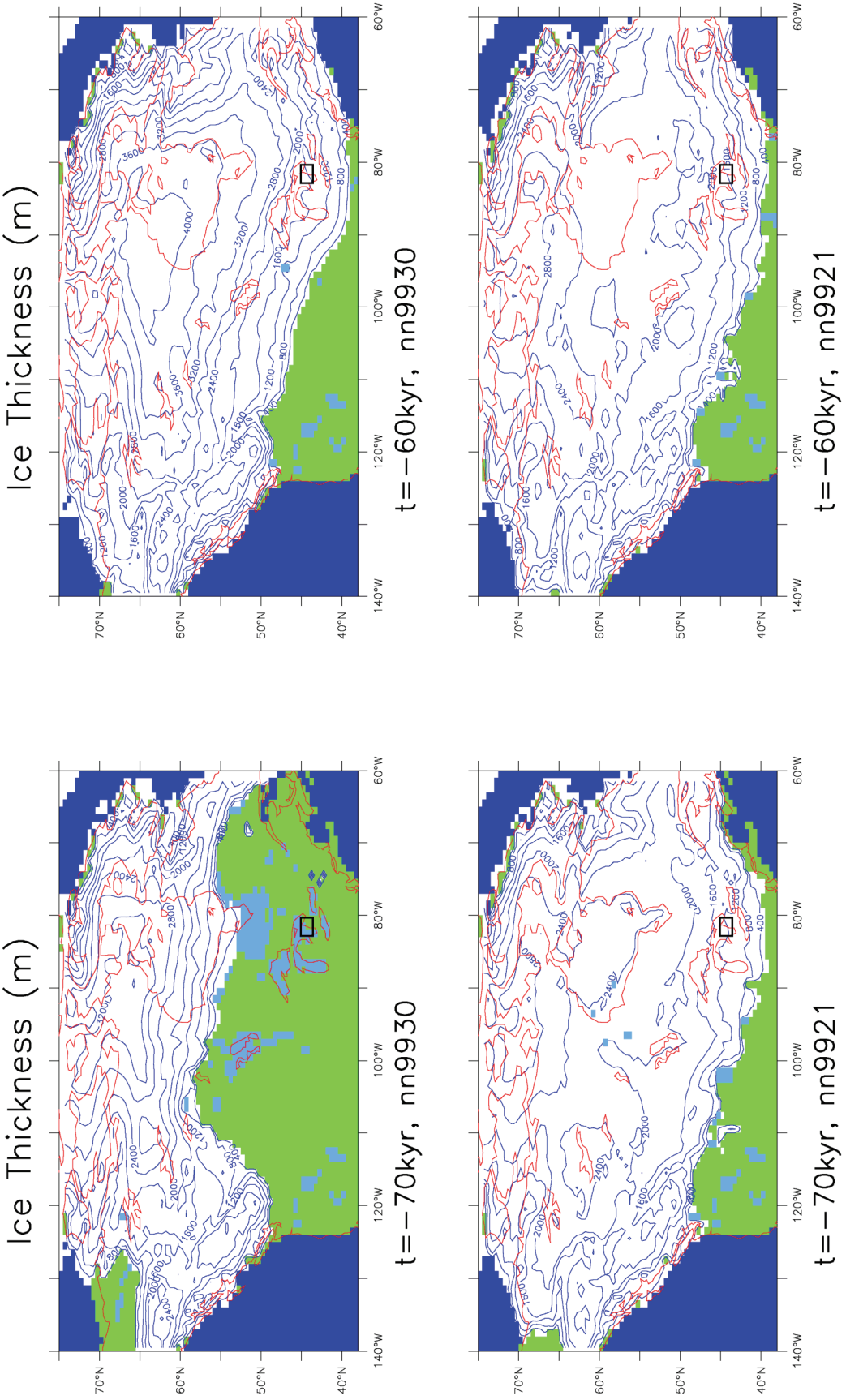
Ice Thickness (m)
t=−60kyr, nn9930
t=−60kyr, nn9921
t=−70kyr, nn9930
t=−70kyr, nn9921
70°N
60°N
50°N
40°N
140°W
120°W
100°W
80°W
60°W

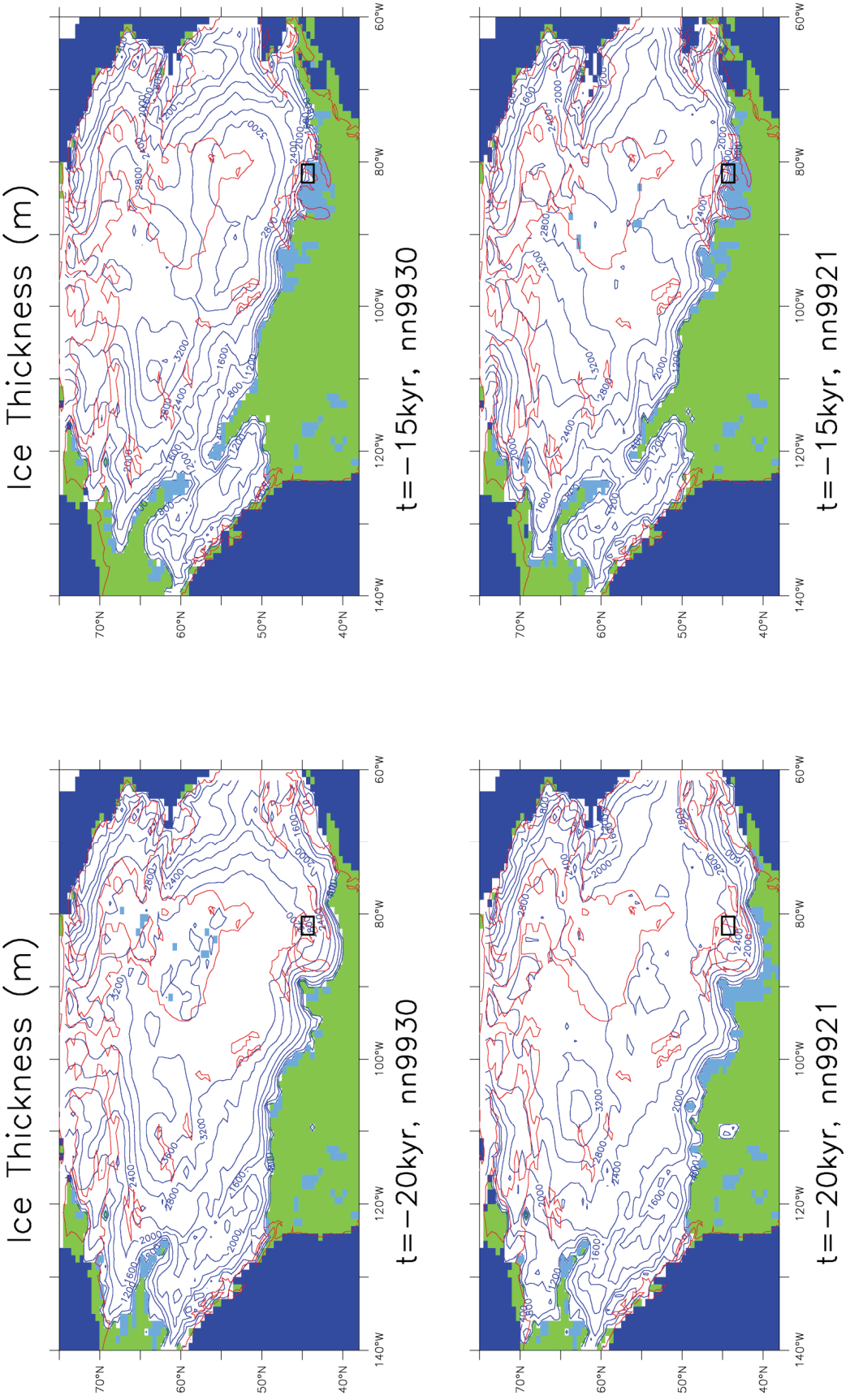
Ice Thickness (m)
t=−15kyr, nn9930
t=−15kyr, nn9921
t=−20kyr, nn9930
t=−20kyr, nn9921
70°N
60°N
50°N
40°N
140°W
120°W
100°W
80°W
60°W

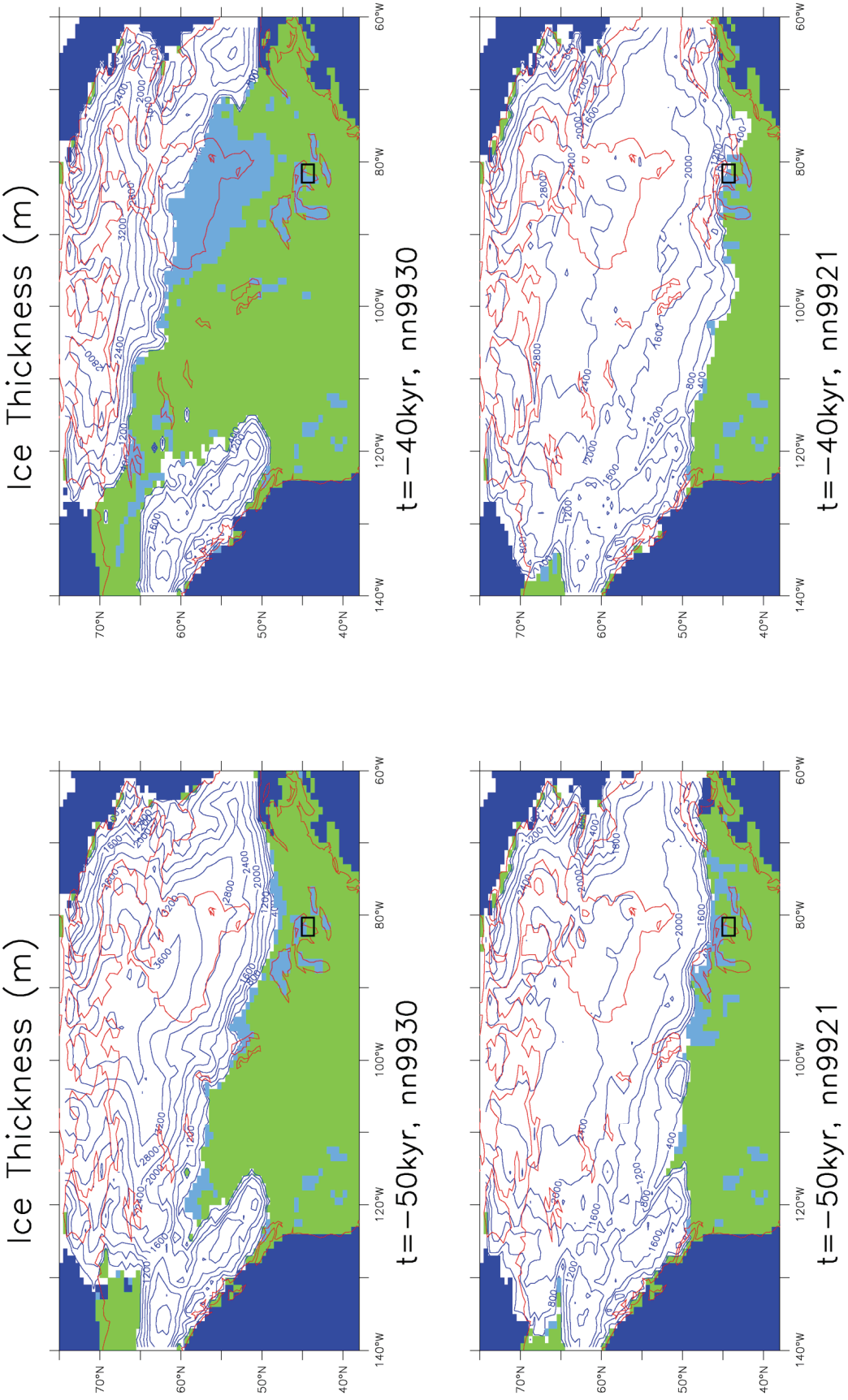
Ice Thickness (m)
t=−40kyr, nn9930
t=−40kyr, nn9921
t=−50kyr, nn9930
t=−50kyr, nn9921
70°N
60°N
50°N
40°N
140°W
120°W
100°W
80°W
60°W

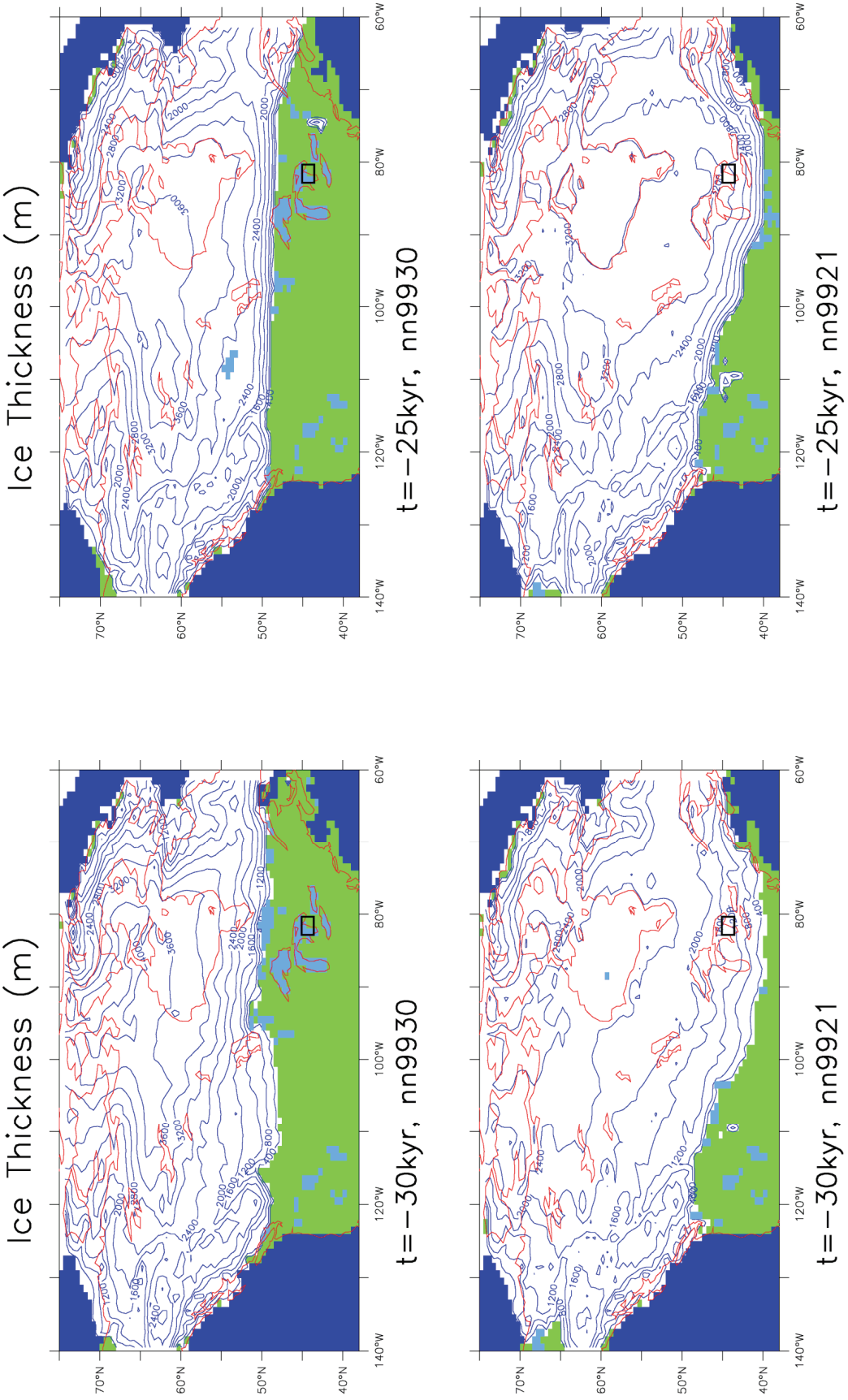
Ice Thickness (m)
t=−25kyr, nn9930
t=−25kyr, nn9921
t=−30kyr, nn9930
t=−30kyr, nn9921
70°N
60°N
50°N
40°N
140°W
120°W
100°W
80°W
60°W

Appendix A2: Basal (Surface) Temperature

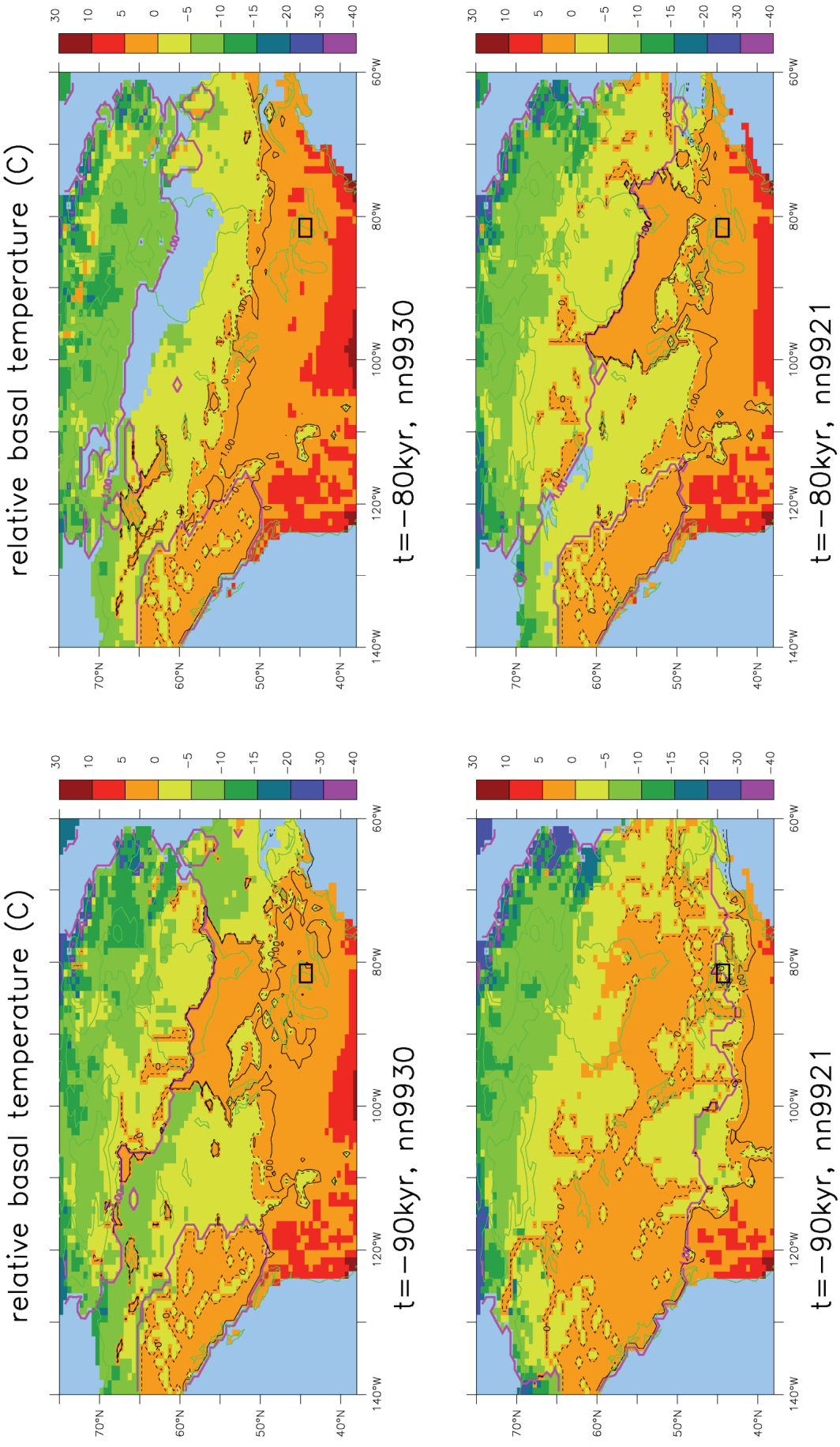
relative basal temperature (C)
t=−80kyr, nn9930
t=−80kyr, nn9921
t=−90kyr, nn9930
t=−90kyr, nn9921
30
10
5
0
−5
−10
−15
−20
−30
−40
70°N
60°N
50°N
40°N
60°W
80°W
100°W
120°W
140°W

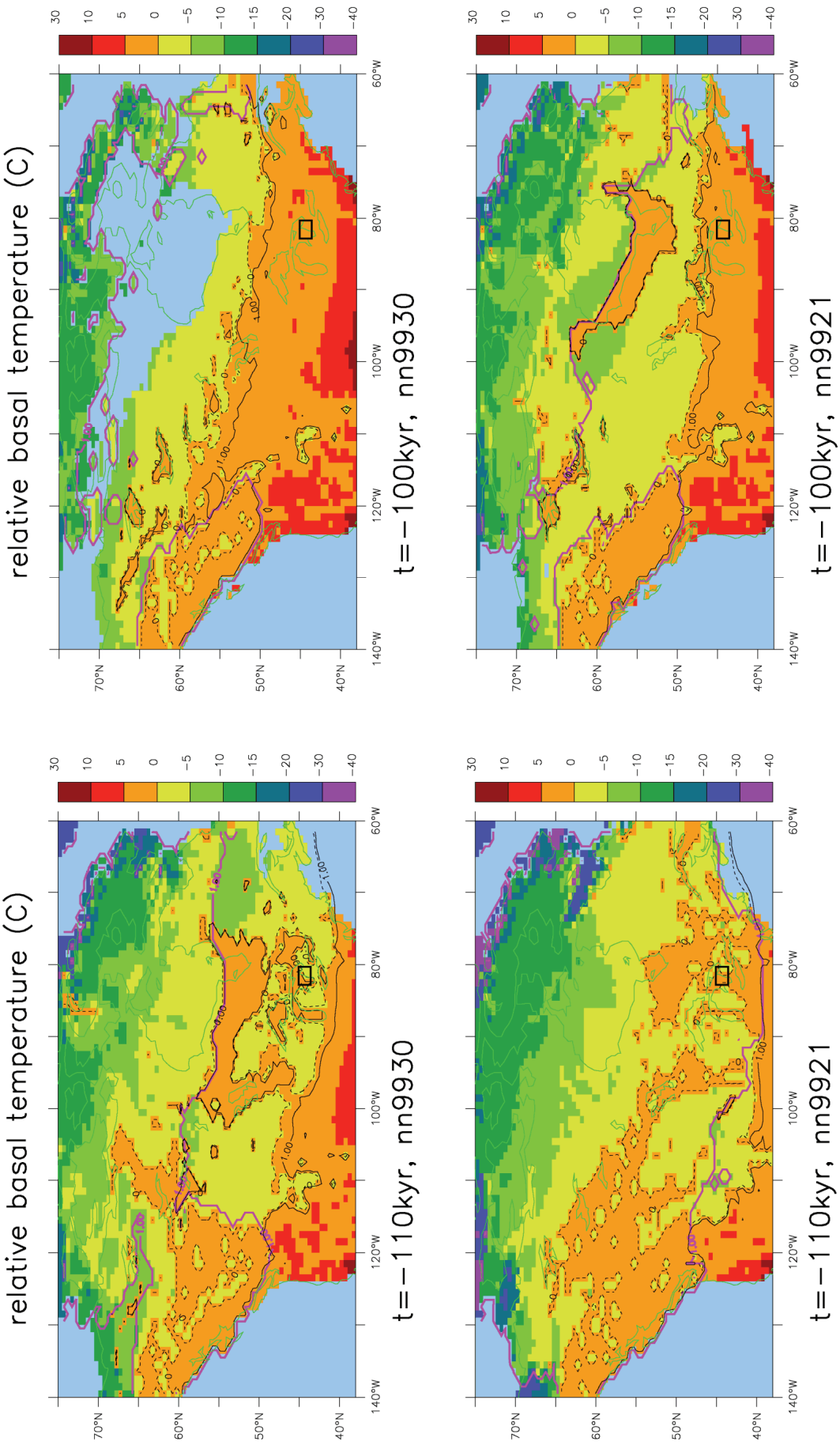
relative basal temperature (C)
t=−100kyr, nn9930
t=−100kyr, nn9921
t=−110kyr, nn9930
t=−110kyr, nn9921
30
10
5
0
−5
−10
−15
−20
−30
−40
70°N
60°N
50°N
40°N
140°W
120°W
100°W
80°W
60°W

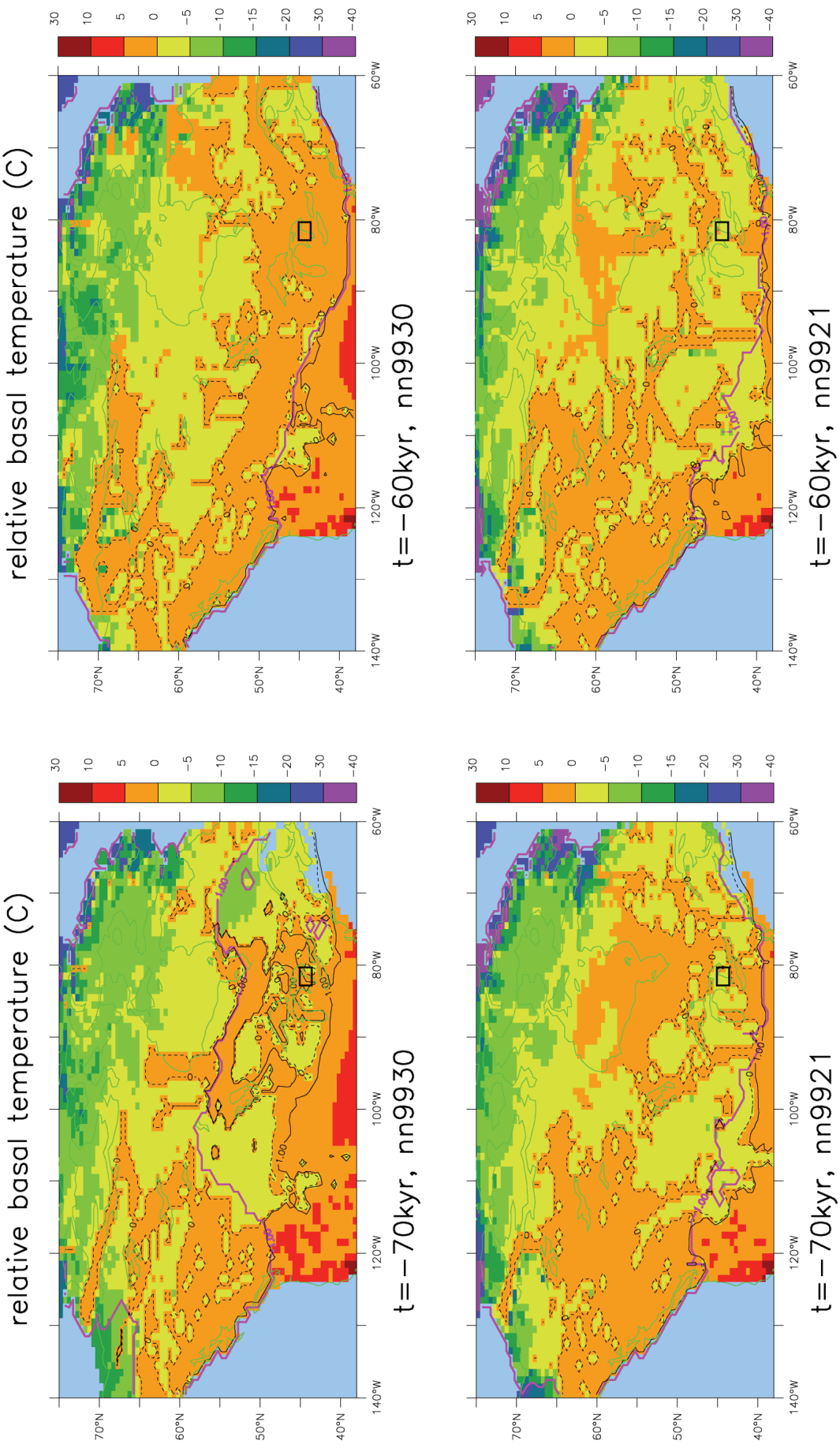
relative basal temperature (C)
t=−60kyr, nn9930
t=−60kyr, nn9921
t=−70kyr, nn9930
t=−70kyr, nn9921
30
10
5
0
−5
−10
−15
−20
−30
−40
70°N
60°N
50°N
40°N
140°W
120°W
100°W
80°W
60°W

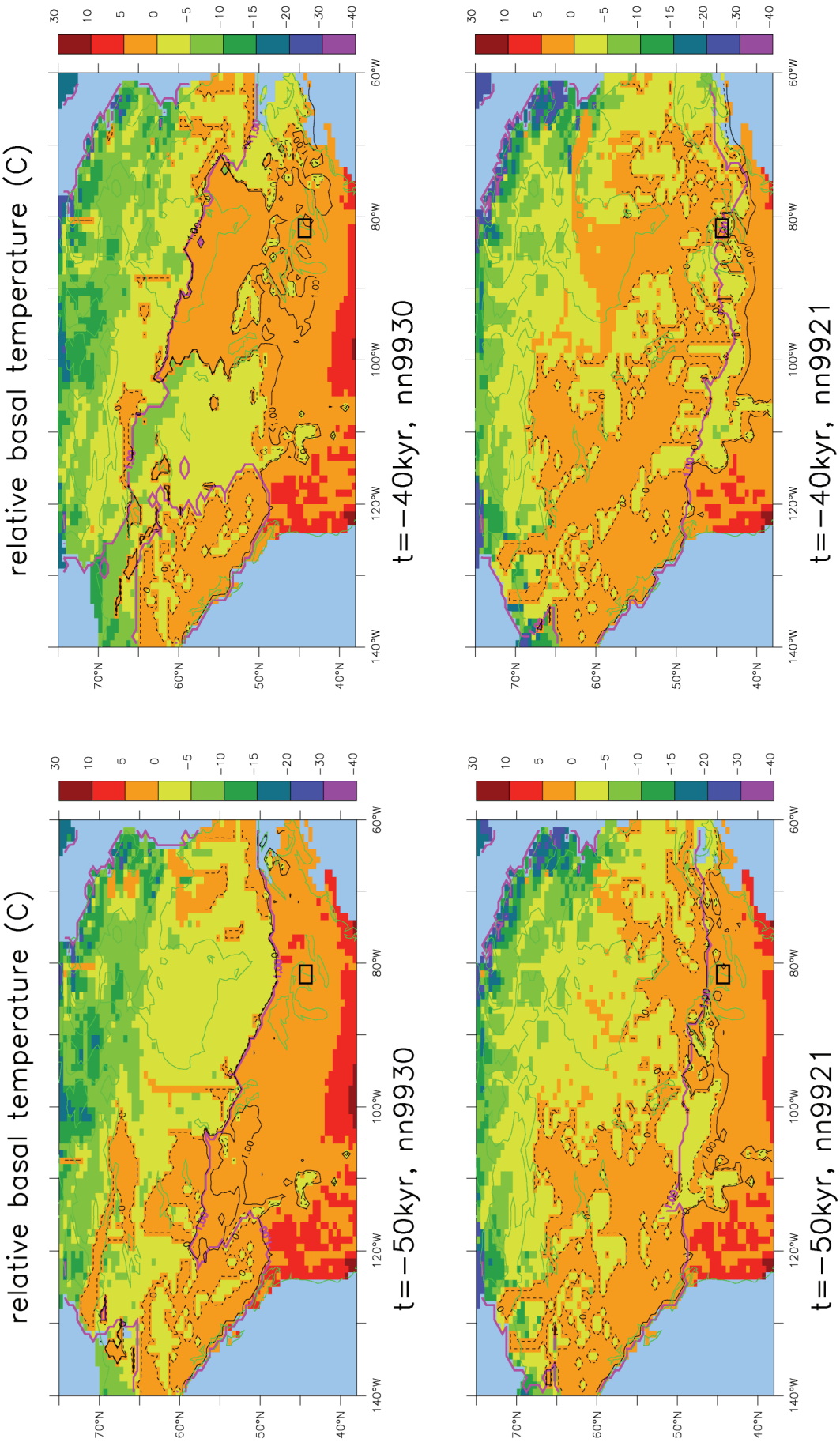
relative basal temperature (C)
t=−40kyr, nn9930
t=−40kyr, nn9921
t=−50kyr, nn9930
t=−50kyr, nn9921
30
10
5
0
−5
−10
−15
−20
−30
−40
70°N
60°N
50°N
40°N
140°W
120°W
100°W
80°W
60°W

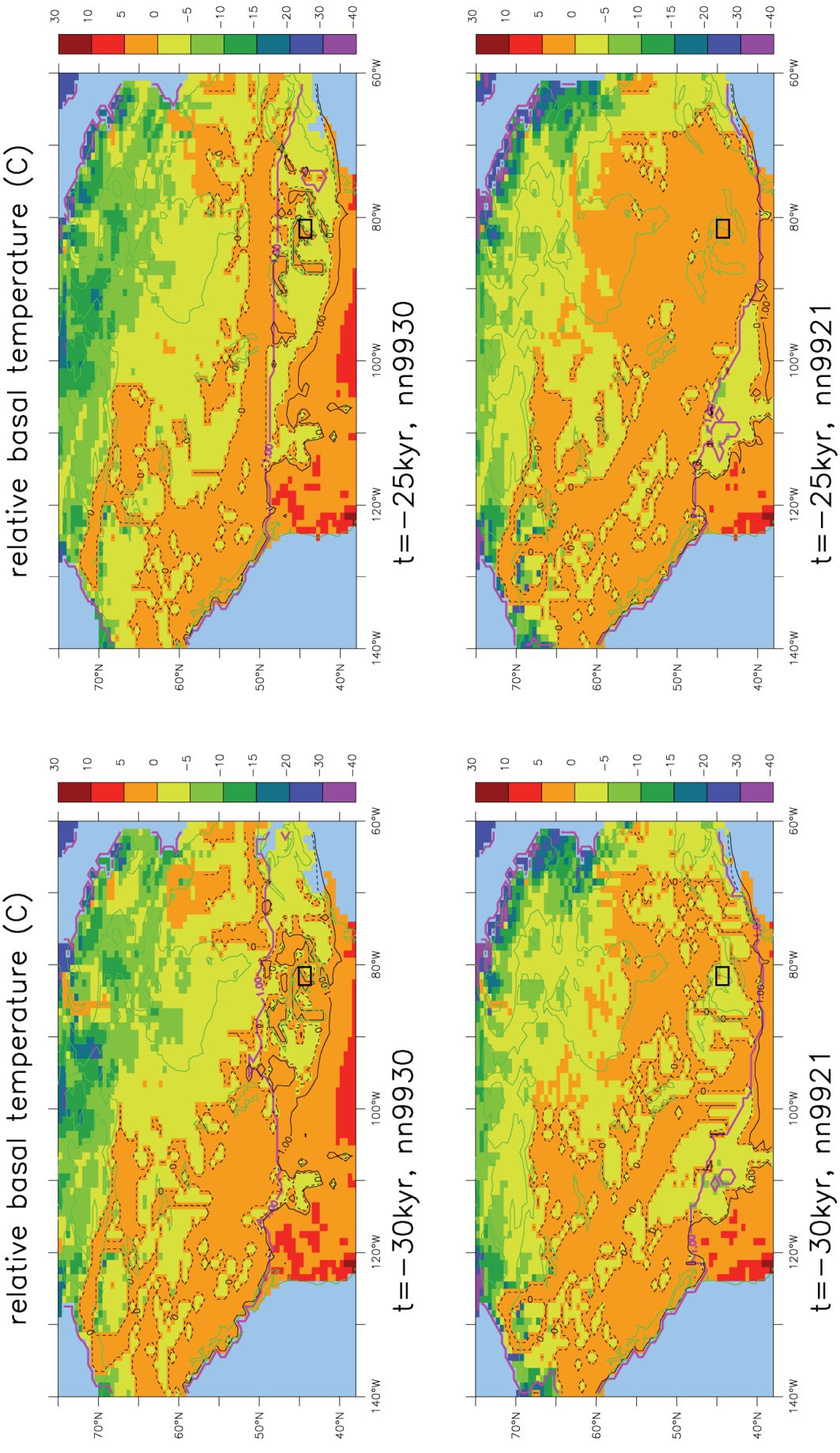
relative basal temperature (C)
t=−25kyr, nn9930
t=−25kyr, nn9921
t=−30kyr, nn9930
t=−30kyr, nn9921
30
10
5
0
−5
−10
−15
−20
−30
−40
70°N
60°N
50°N
40°N
140°W
120°W
100°W
80°W
60°W

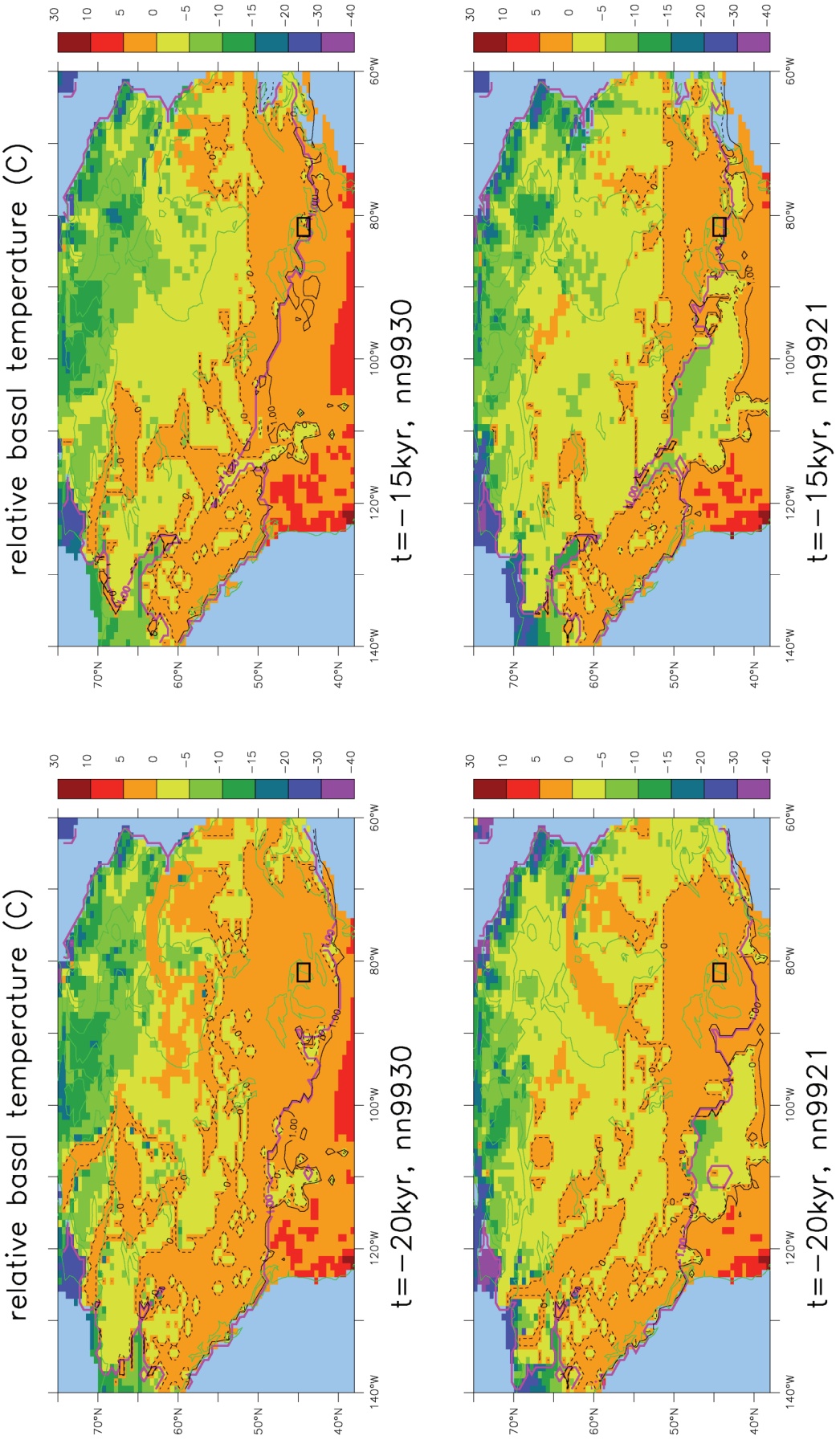
relative basal temperature (C)
t=−15kyr, nn9930
t=−15kyr, nn9921
t=−20kyr, nn9930
t=−20kyr, nn9921
30
10
5
0
−5
−10
−15
−20
−30
−40
60°W
80°W
100°W
120°W
140°W
70°N
60°N
50°N
40°N

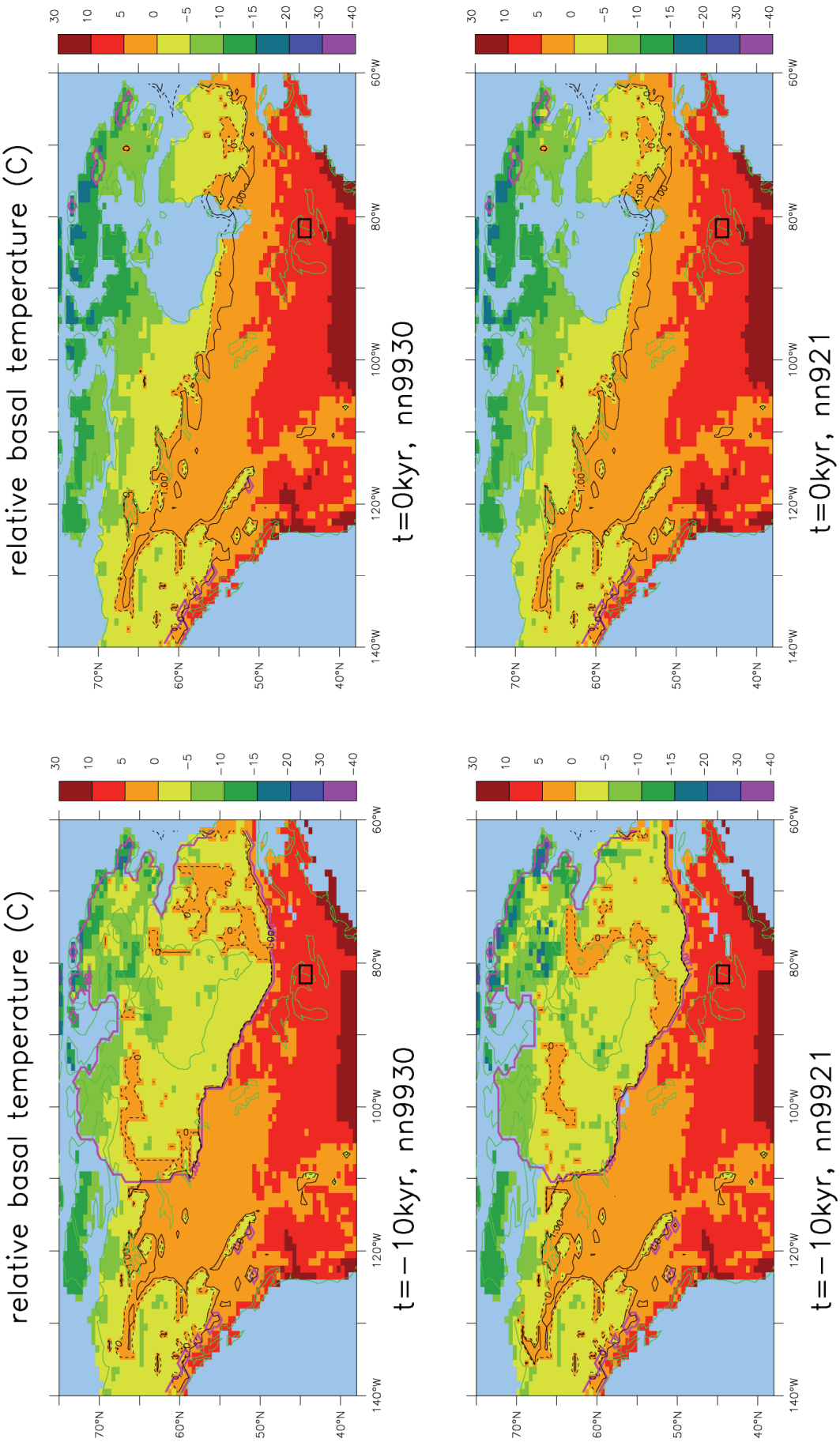
relative basal temperature (C)
t=0kyr, nn9930
t=0kyr, nn921
t=−10kyr, nn9930
t=−10kyr, nn9921
30
10
5
0
−5
−10
−15
−20
−30
−40
70°N
60°N
50°N
40°N
140°W
120°W
100°W
80°W
60°W

Appendix A3: Permafrost Depth

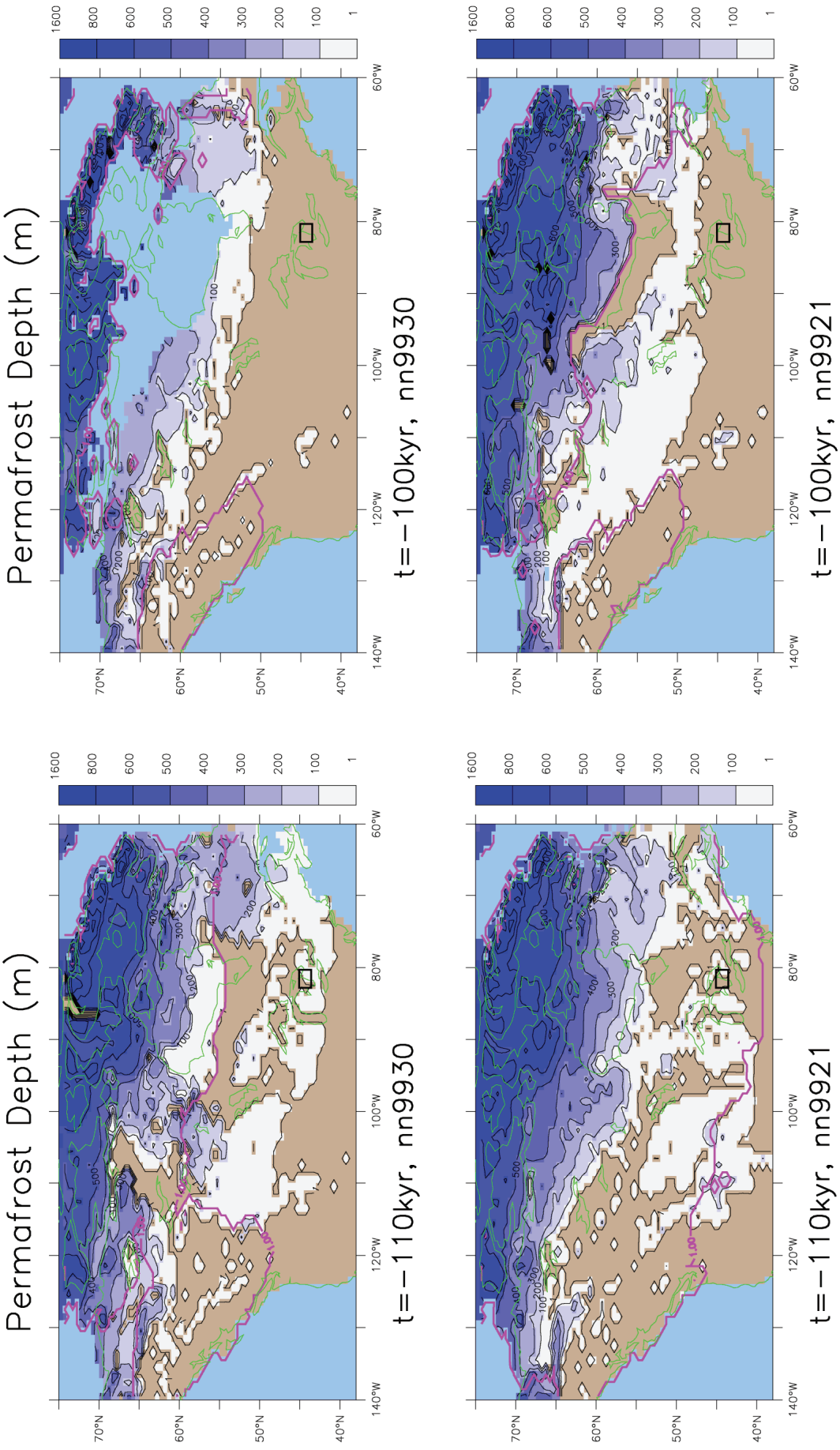
Permafrost Depth (m)
t=-100kyr, nn9930
t=-100kyr, nn9921
t=-110kyr, nn9930
t=-110kyr, nn9921
1600
800
600
500
400
300
200
100
1
70°N
60°N
50°N
40°N
140°W
120°W
100°W
80°W
60°W

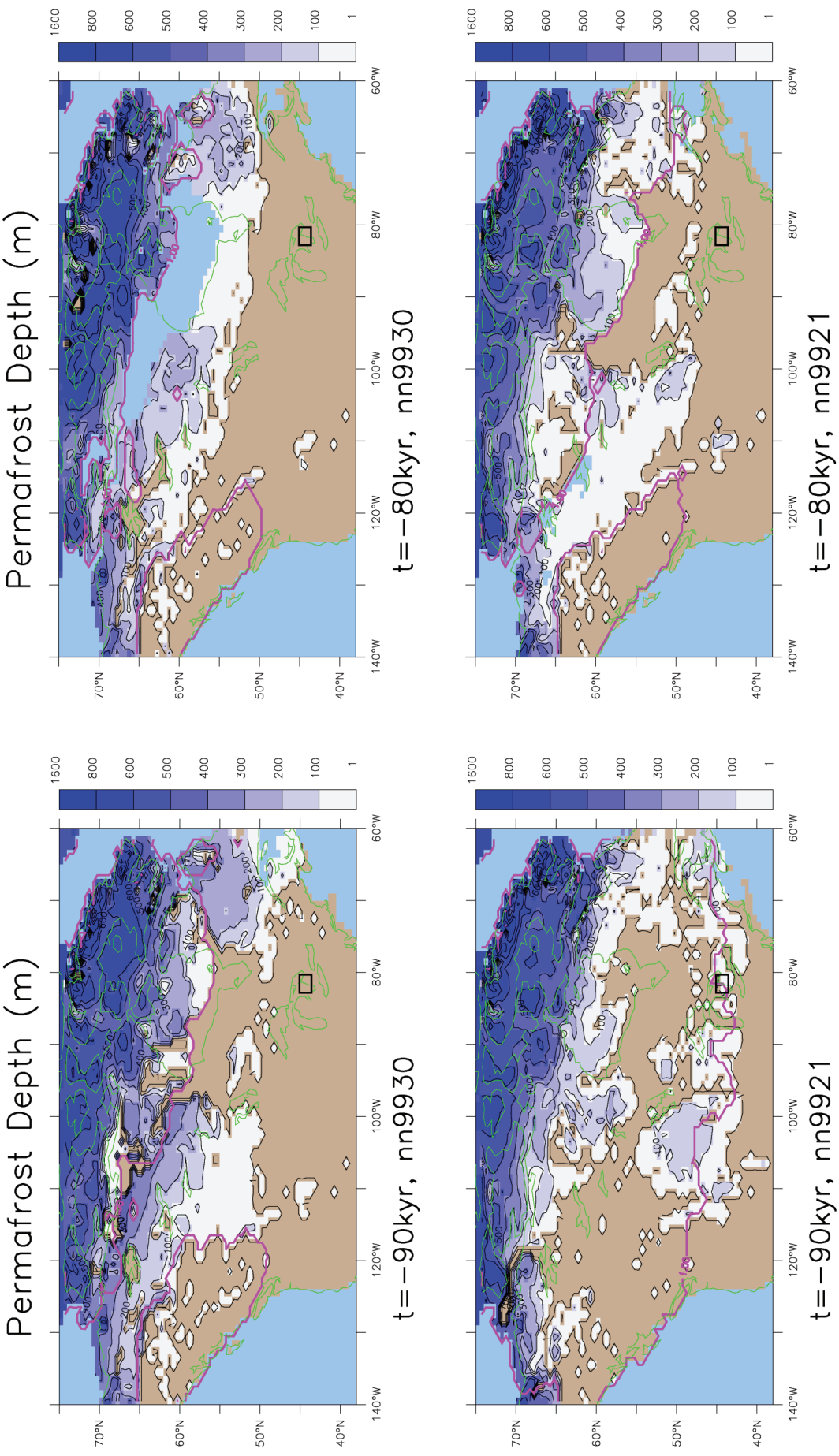
Permafrost Depth (m)
t=−80kyr, nn9930
t=−80kyr, nn9921
t=−90kyr, nn9930
t=−90kyr, nn9921
1600
800
600
500
400
300
200
100
1
70°N
60°N
50°N
40°N
140°W
120°W
100°W
80°W
60°W

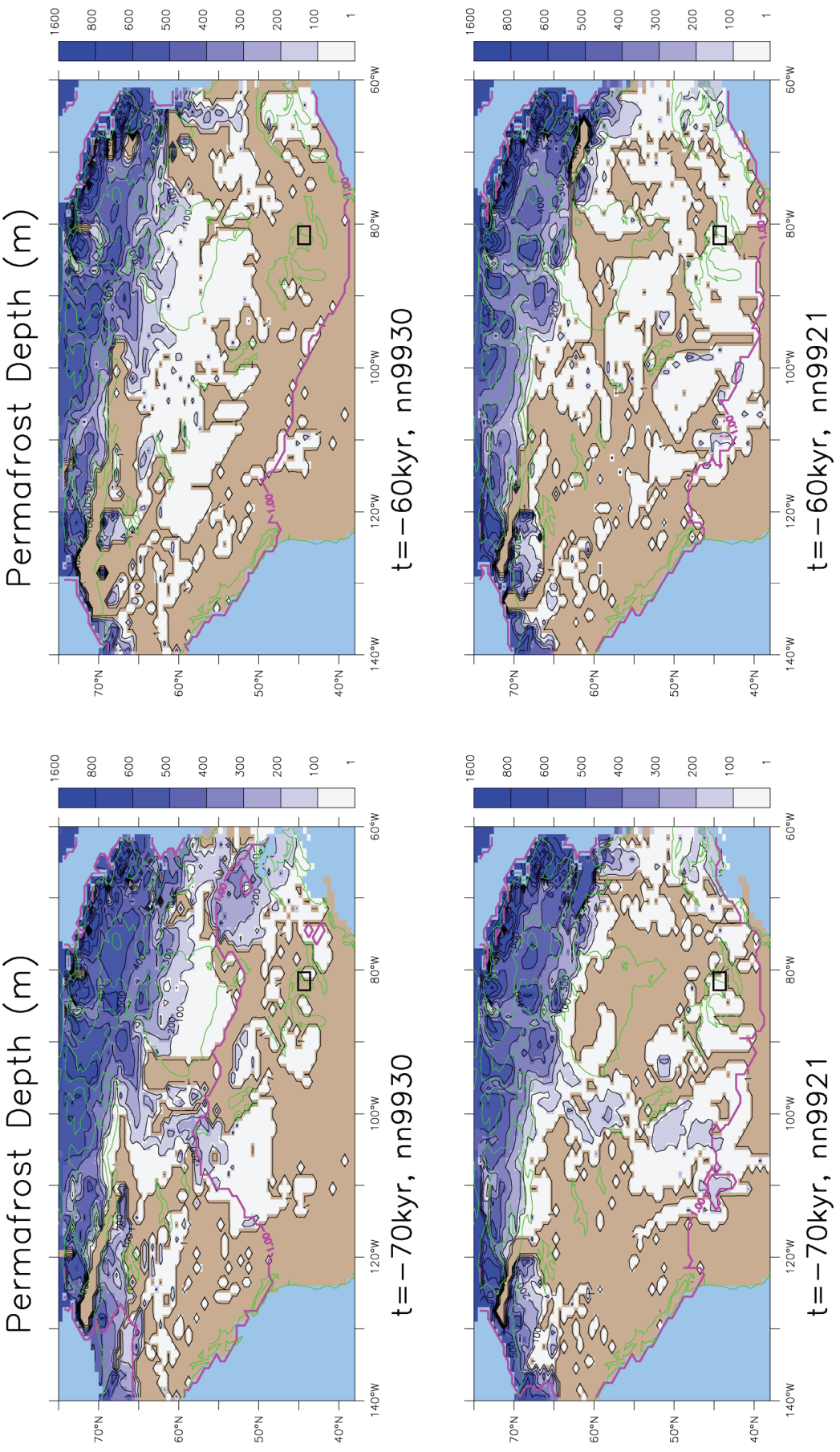
Permafrost Depth (m)
t=−60kyr, nn9930
t=−60kyr, nn9921
t=−70kyr, nn9930
t=−70kyr, nn9921
1600
800
600
500
400
300
200
100
1
70°N
60°N
50°N
40°N
60°W
80°W
100°W
120°W
140°W

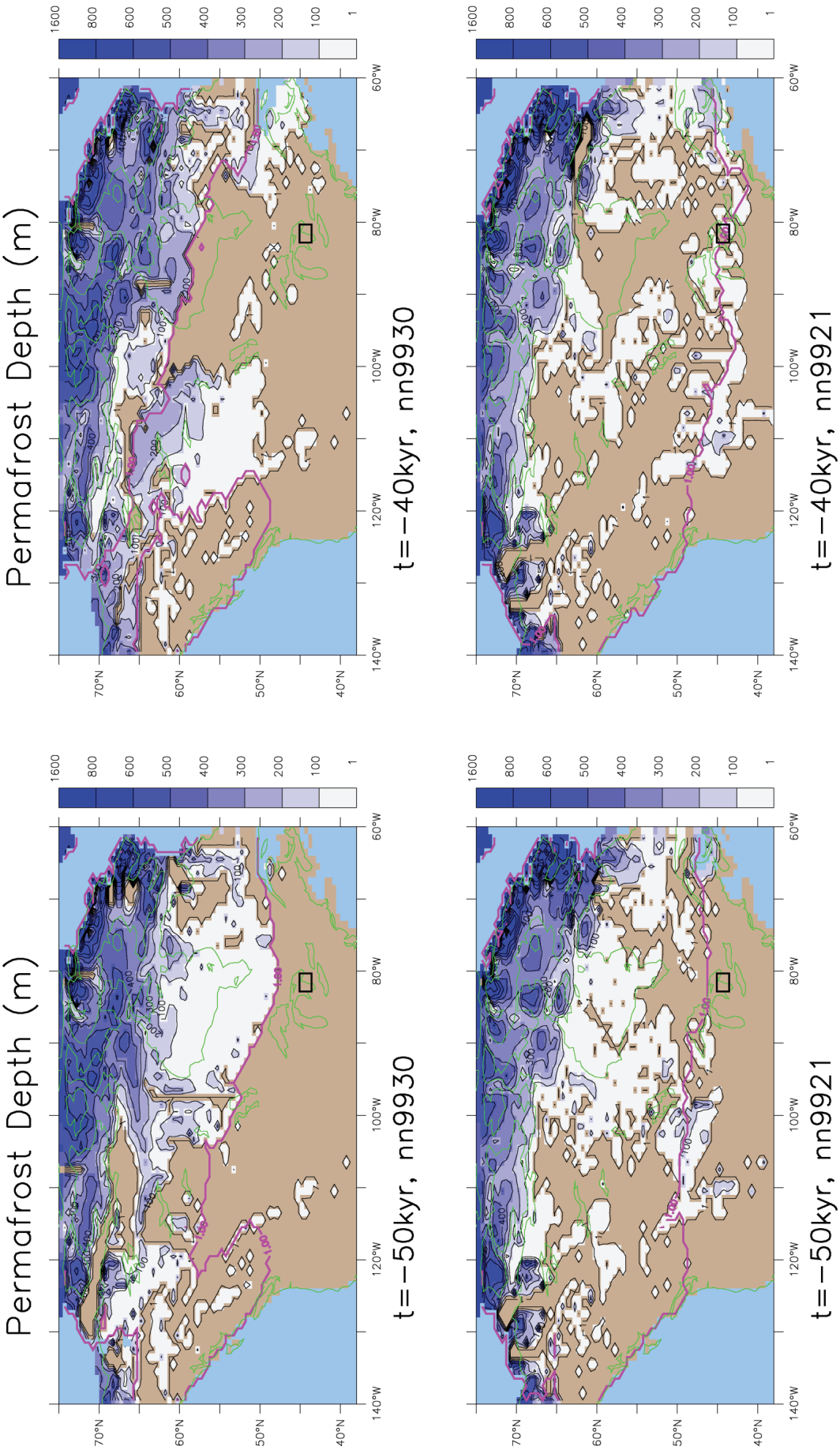
Permafrost Depth (m)
1600
800
600
500
400
300
200
100
1
70°N
60°N
50°N
40°N
60°W
80°W
100°W
120°W
140°W
t=−40kyr, nn9930
t=−40kyr, nn9921
t=−50kyr, nn9930
t=−50kyr, nn9921

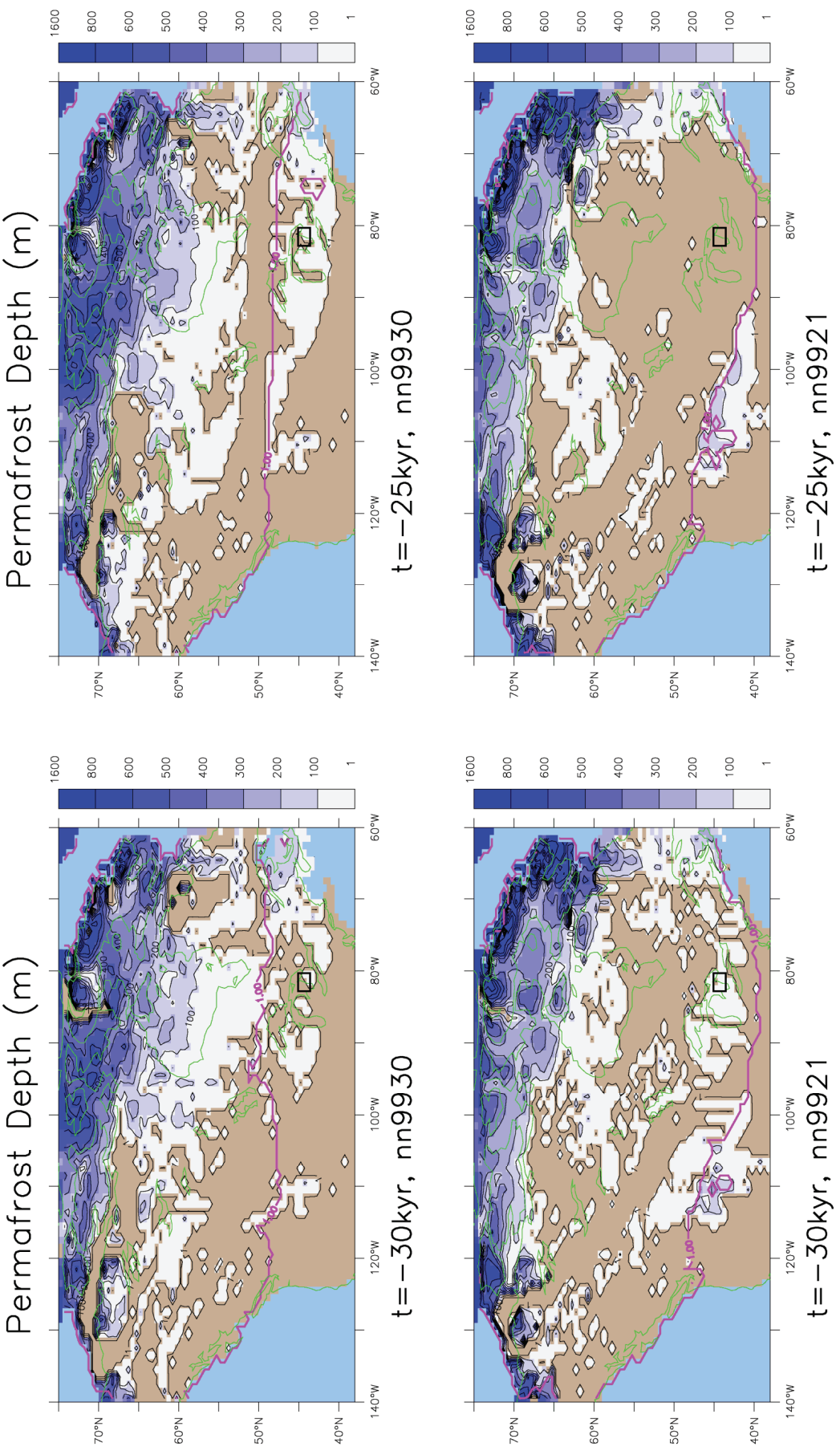
Permafrost Depth (m)
t=−25kyr, nn9930
t=−25kyr, nn9921
t=−30kyr, nn9930
t=−30kyr, nn9921
1600
800
600
500
400
300
200
100
1
70°N
60°N
50°N
40°N
60°W
80°W
100°W
120°W
140°W

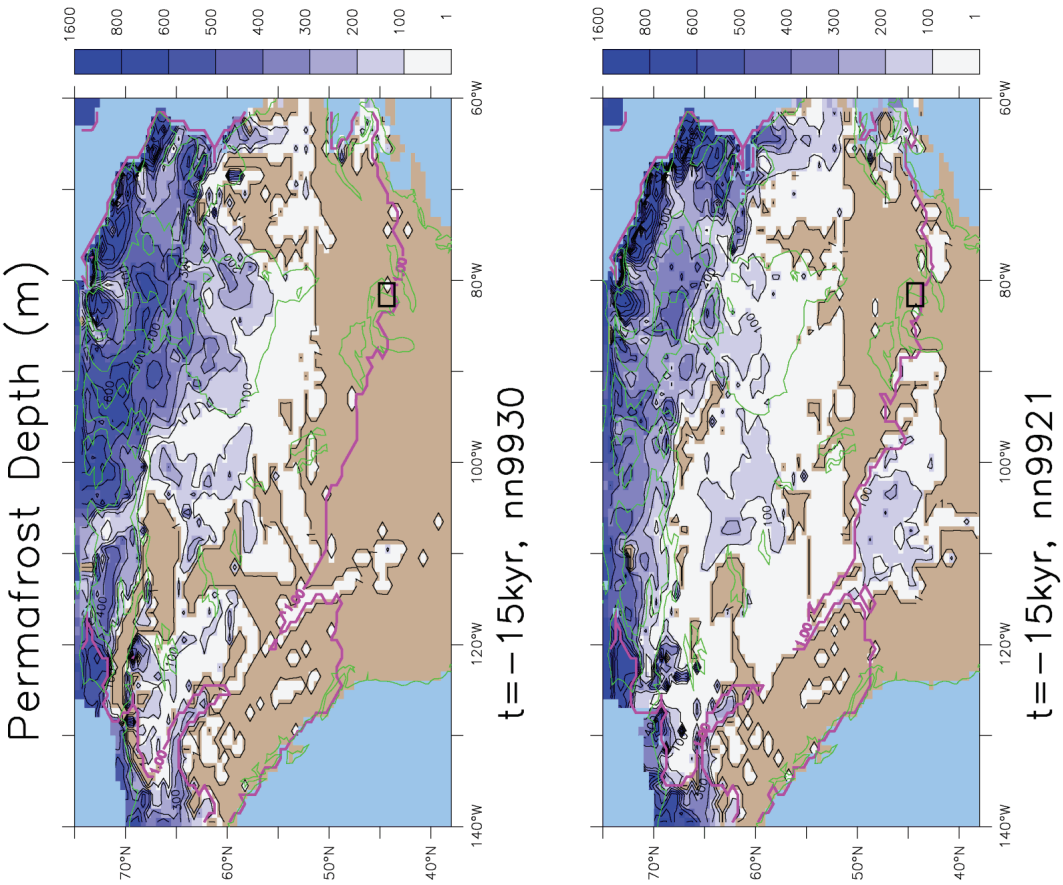
Permafrost Depth (m)
1600
800
600
500
400
300
200
100
1
70°N
60°N
50°N
40°N
140°W
120°W
100°W
80°W
60°W
t=−15kyr, nn9930
t=−15kyr, nn9921

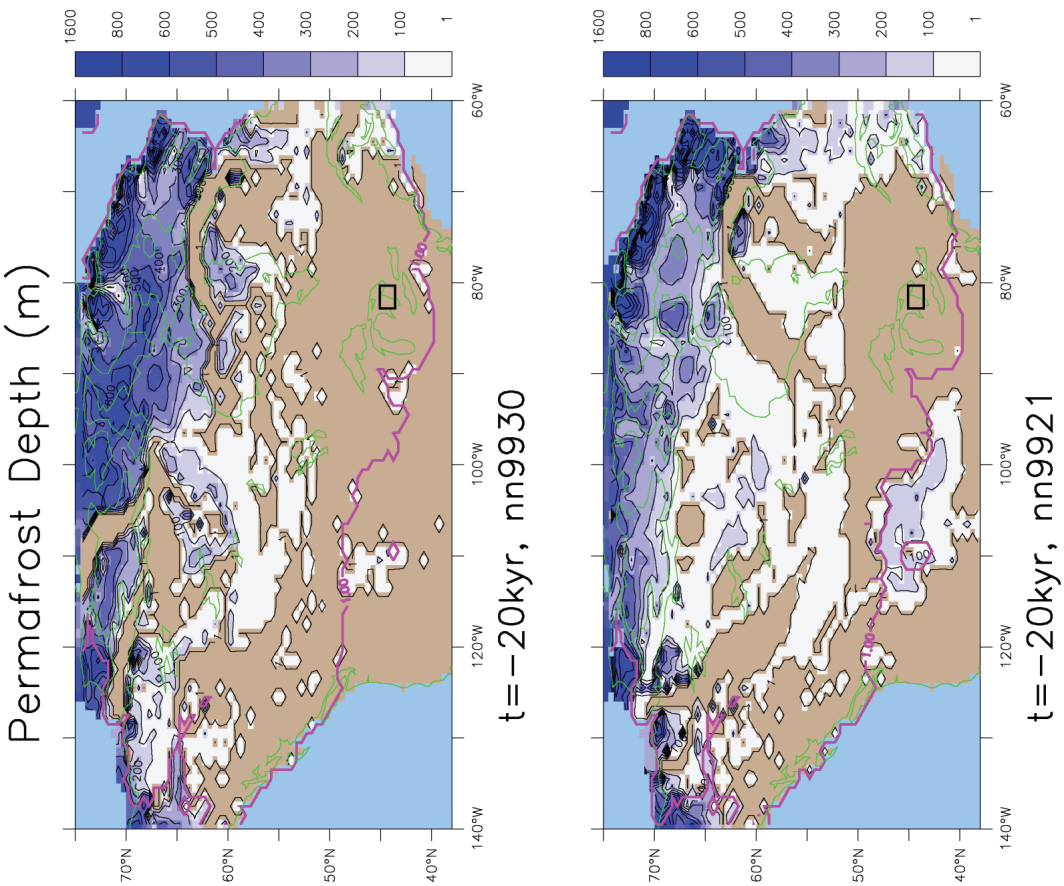
Permafrost Depth (m)
1600
800
600
500
400
300
200
100
1
70°N
60°N
50°N
40°N
140°W
120°W
100°W
80°W
60°W
t=−20kyr, nn9930
t=−20kyr, nn9921

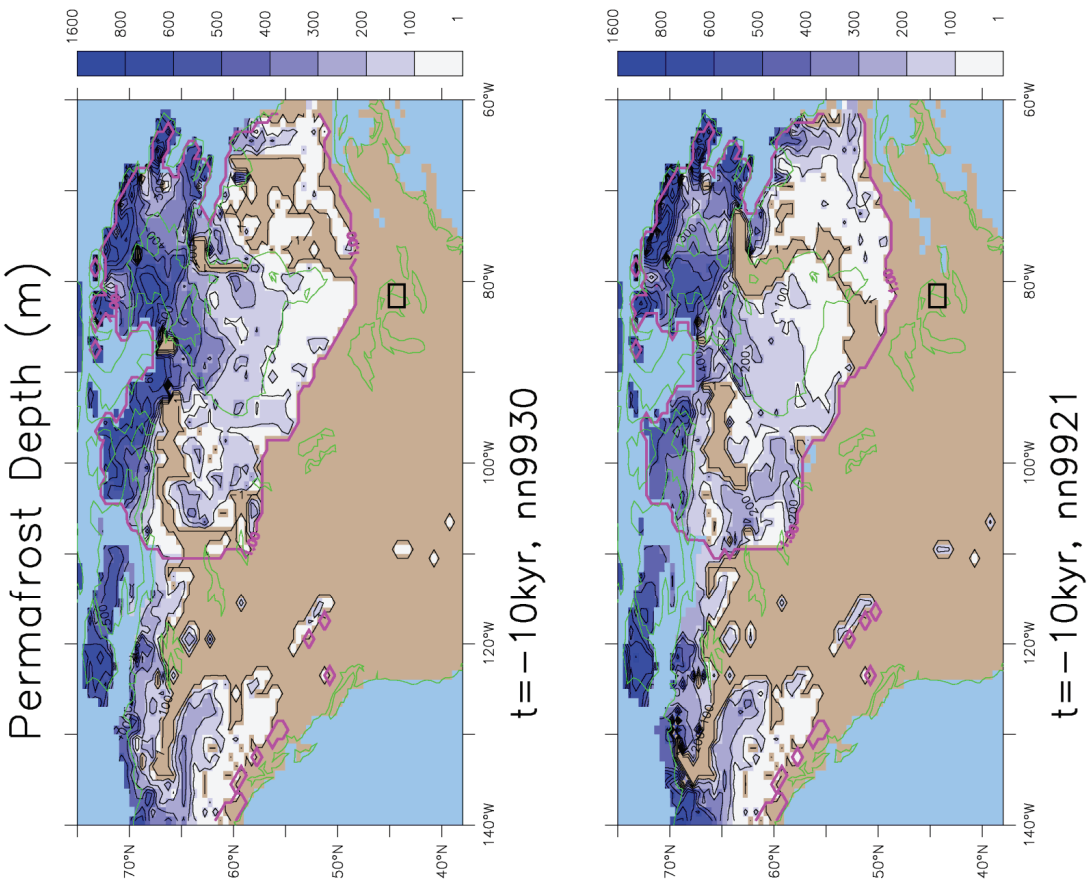
Permafrost Depth (m)
1600
800
600
500
400
300
200
100
1
60°W
80°W
100°W
120°W
140°W
70°N
60°N
50°N
40°N
t=−10kyr, nn9930
t=−10kyr, nn9921

Appendix A4: Deflection of the Surface of the Solid Earth Below its Equilibrium Level

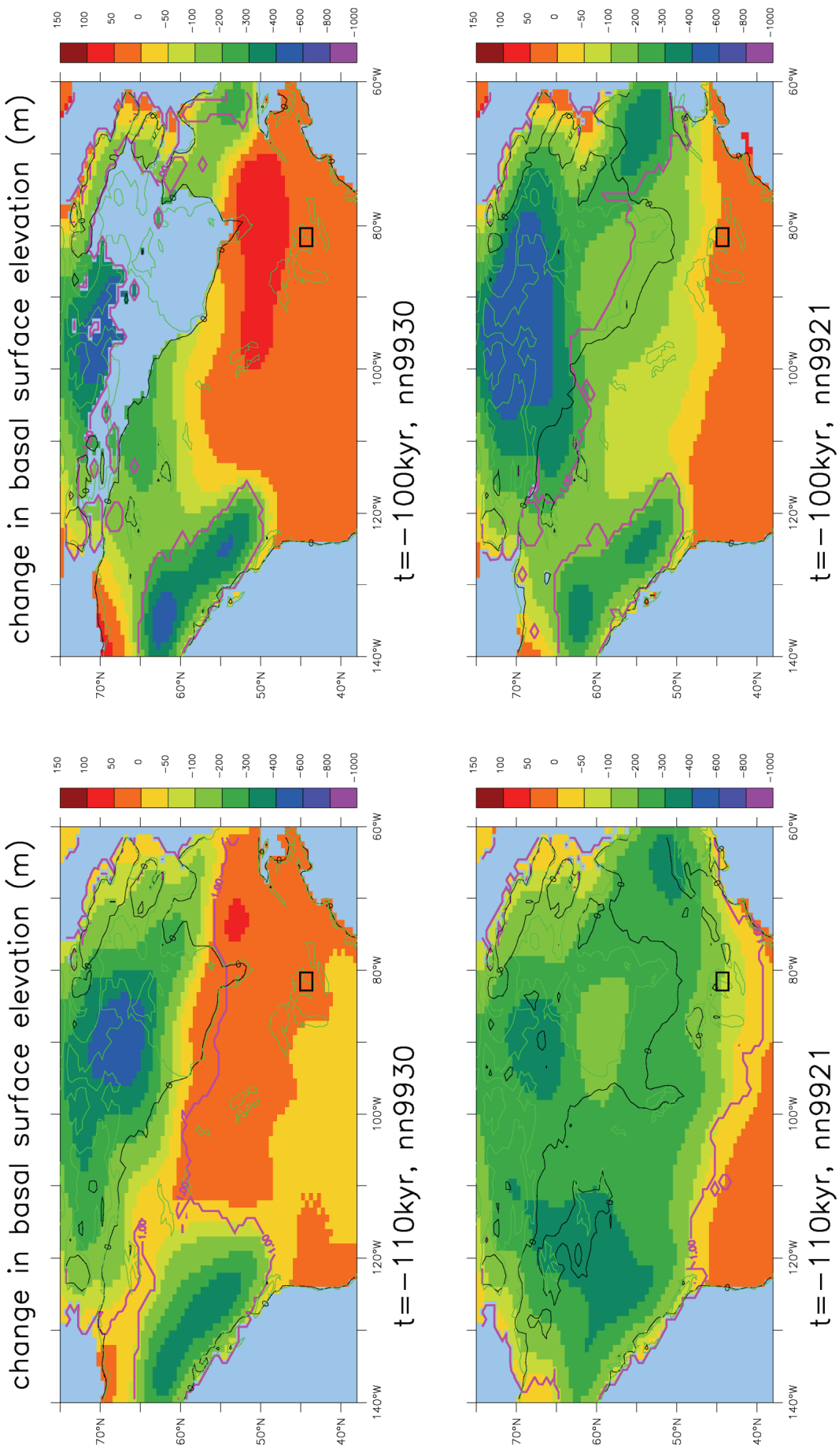
change in basal surface elevation (m)
150
100
50
0
−50
−100
−200
−300
−400
−600
−800
−1000
70°N
60°N
50°N
40°N
140°W
120°W
100°W
80°W
60°W
t=−100kyr, nn9930
t=−100kyr, nn9921
t=−110kyr, nn9930
t=−110kyr, nn9921

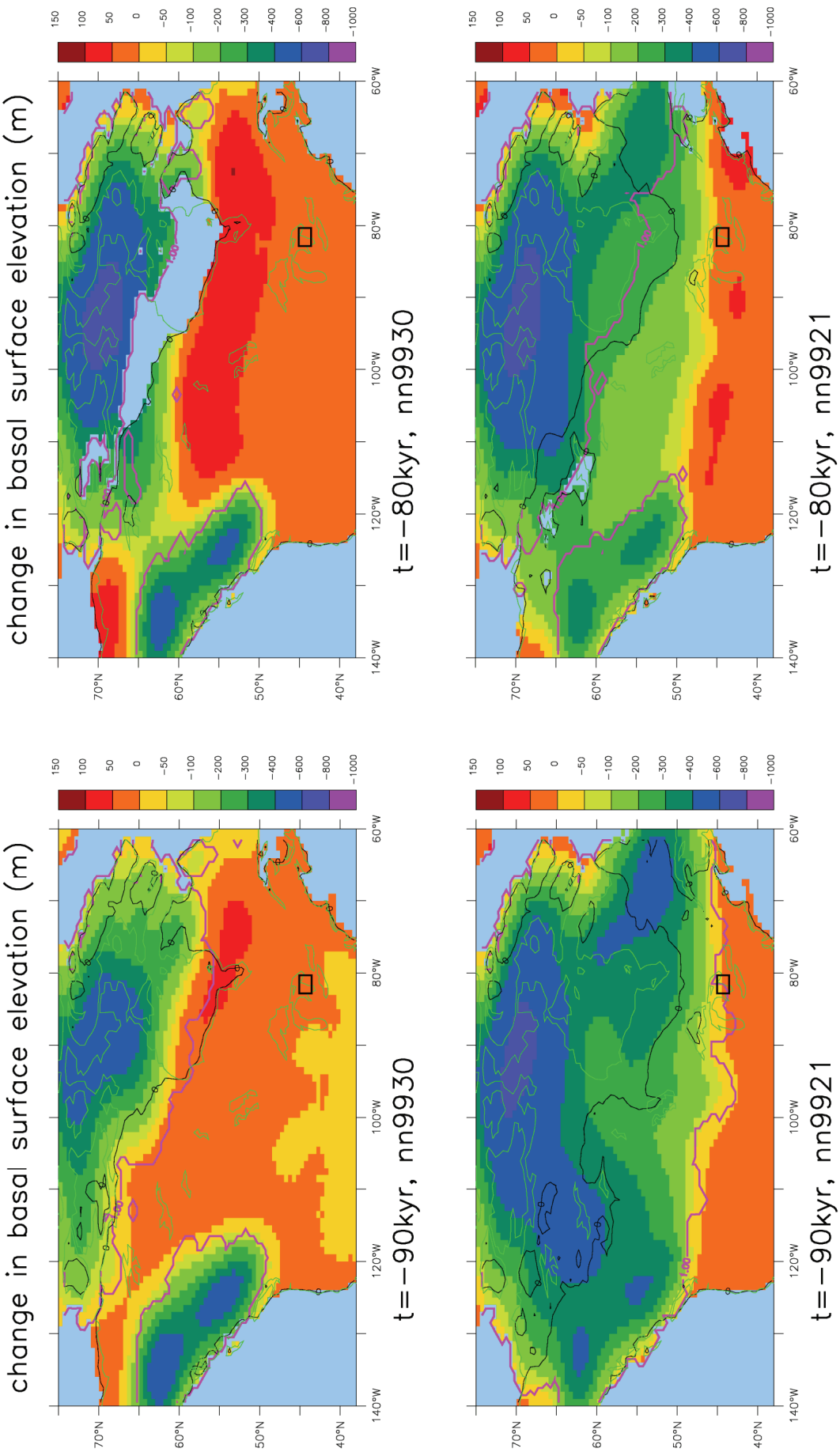
change in basal surface elevation (m)
150
100
50
0
−50
−100
−200
−300
−400
−600
−800
−1000
70°N
60°N
50°N
40°N
140°W
120°W
100°W
80°W
60°W
t=−80kyr, nn9930
t=−80kyr, nn9921
t=−90kyr, nn9930
t=−90kyr, nn9921

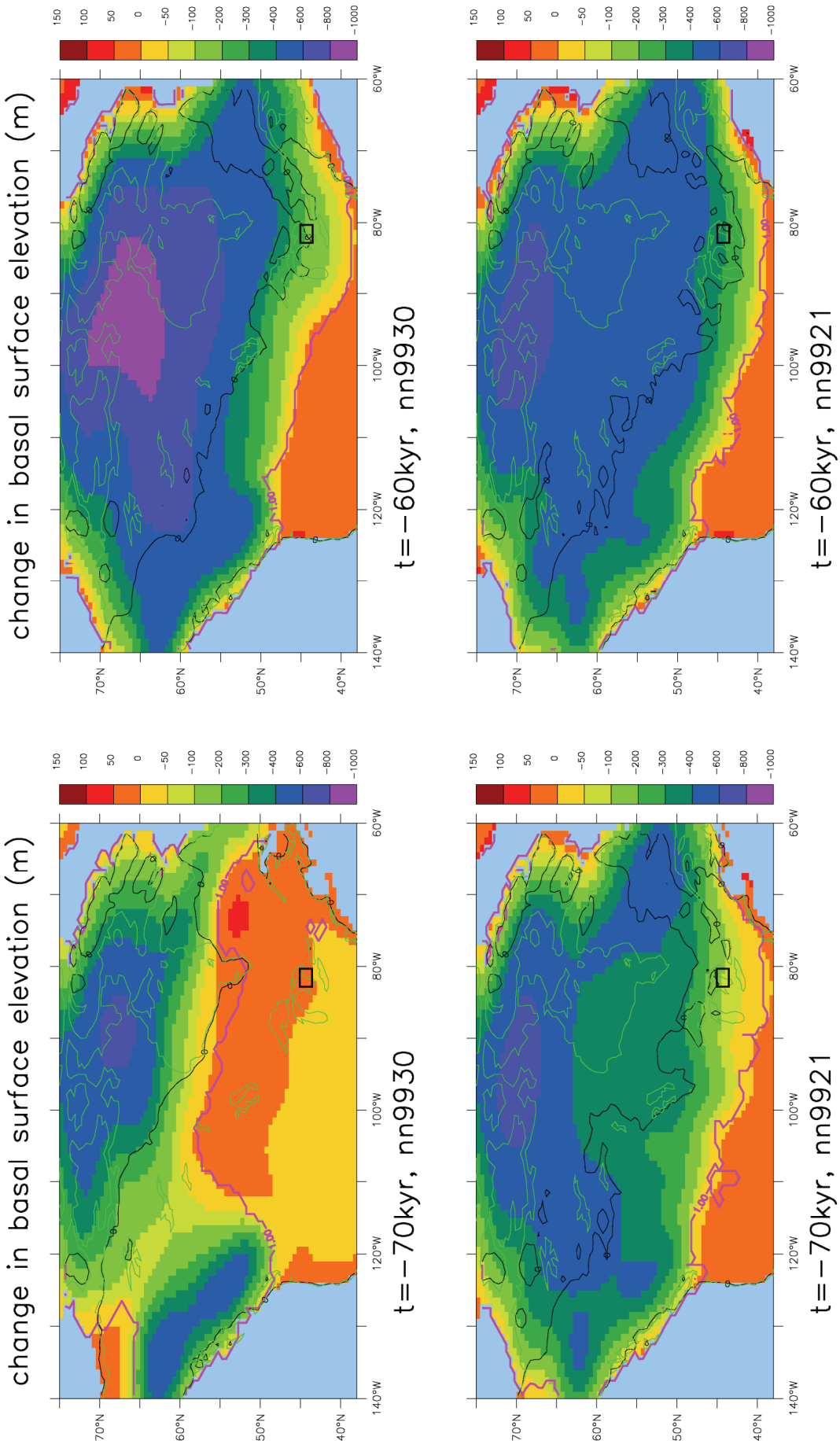
change in basal surface elevation (m)
150
100
50
0
−50
−100
−200
−300
−400
−600
−800
−1000
70°N
60°N
50°N
40°N
140°W
120°W
100°W
80°W
60°W
t=−60kyr, nn9930
t=−60kyr, nn9921
t=−70kyr, nn9930
t=−70kyr, nn9921

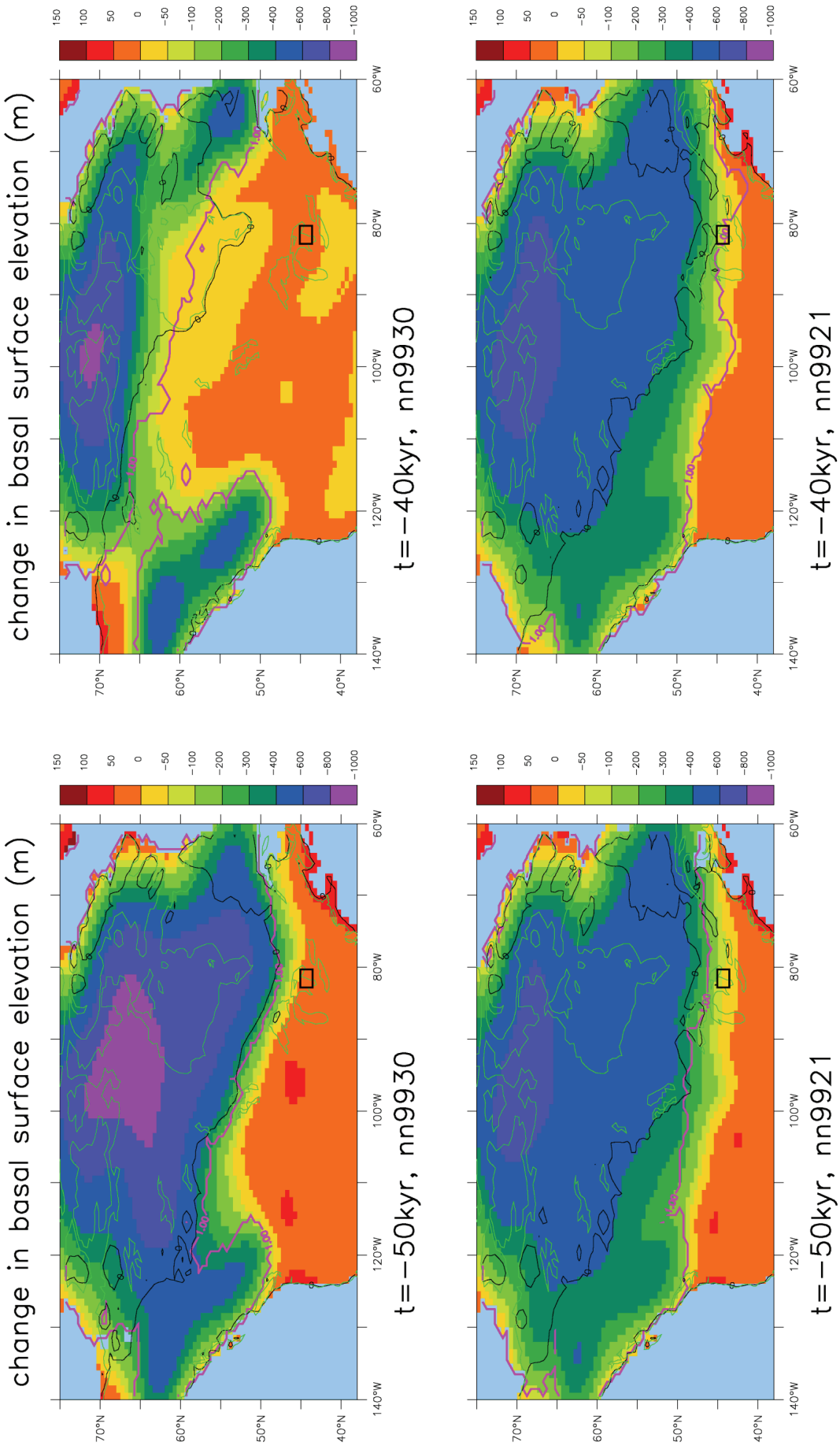
change in basal surface elevation (m)
150
100
50
0
−50
−100
−200
−300
−400
−600
−800
−1000
70°N
60°N
50°N
40°N
140°W
120°W
100°W
80°W
60°W
t=−40kyr, nn9930
t=−40kyr, nn9921
t=−50kyr, nn9930
t=−50kyr, nn9921

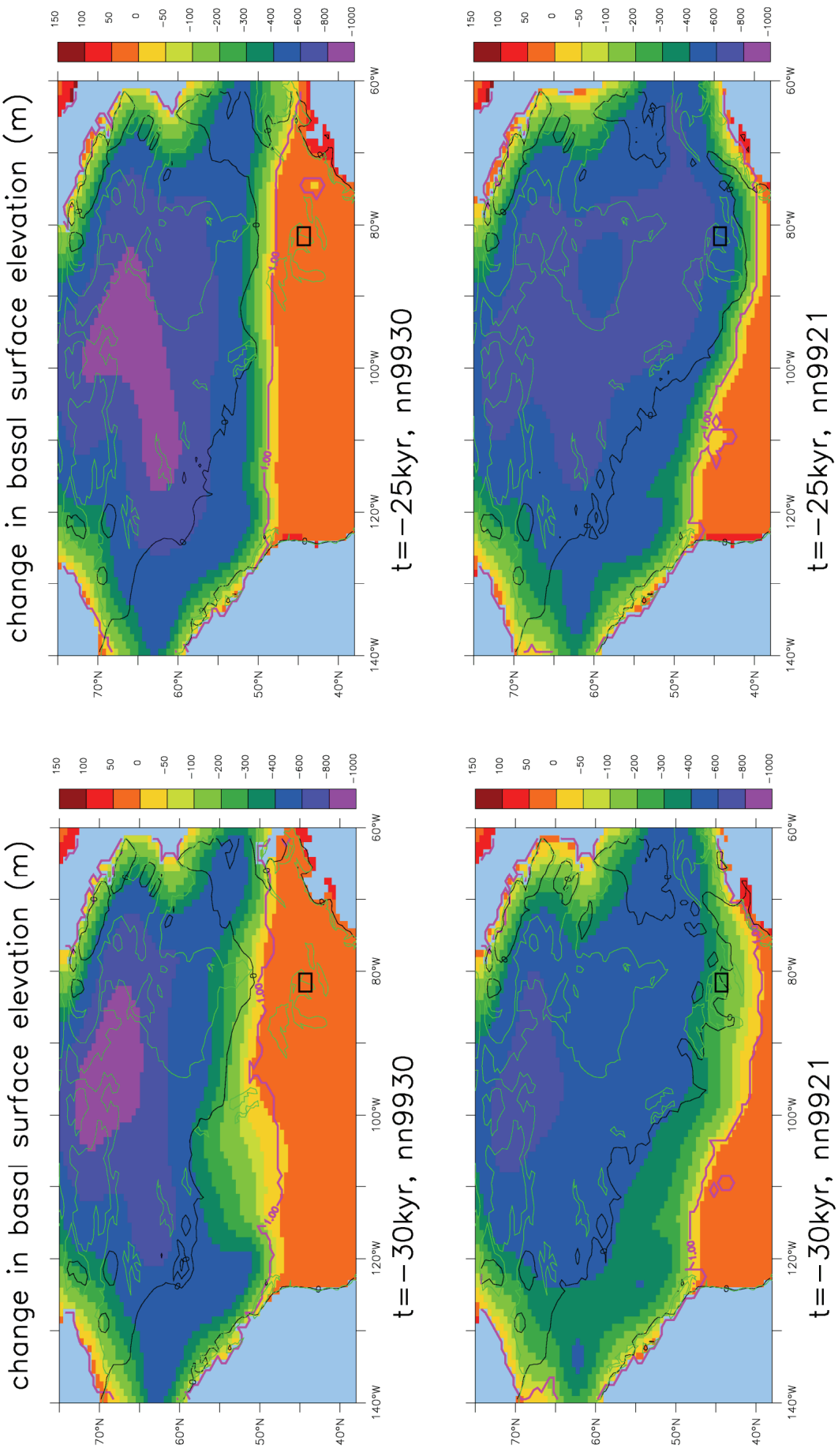
change in basal surface elevation (m)
150
100
50
0
−50
−100
−200
−300
−400
−600
−800
−1000
70°N
60°N
50°N
40°N
140°W
120°W
100°W
80°W
60°W
1.00
t=−25kyr, nn9930
t=−25kyr, nn9921
t=−30kyr, nn9930
t=−30kyr, nn9921

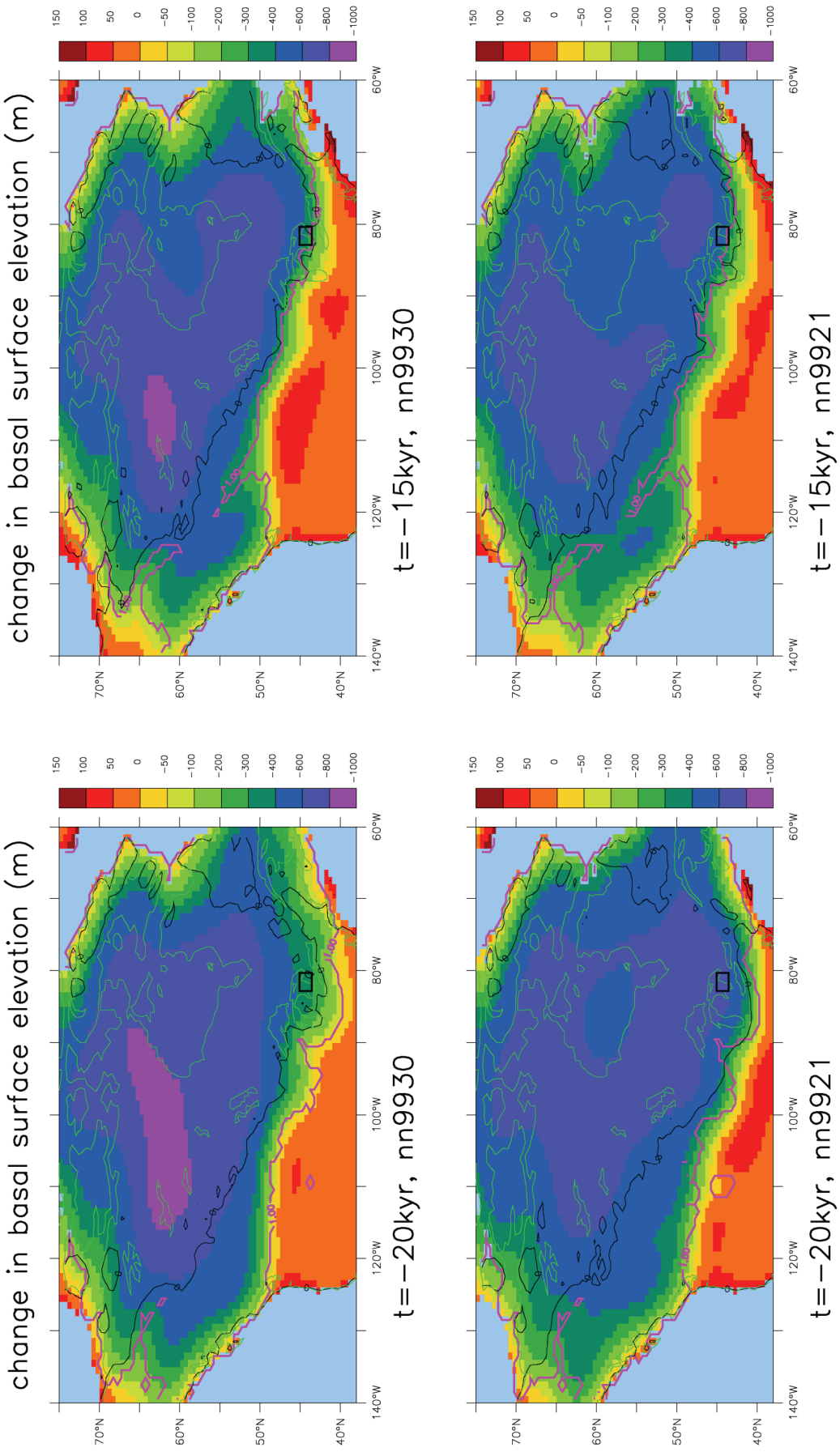
change in basal surface elevation (m)
150
100
50
0
−50
−100
−200
−300
−400
−600
−800
−1000
60°W
80°W
100°W
120°W
140°W
70°N
60°N
50°N
40°N
1.00
t=−15kyr, nn9930
t=−15kyr, nn9921
t=−20kyr, nn9930
t=−20kyr, nn9921

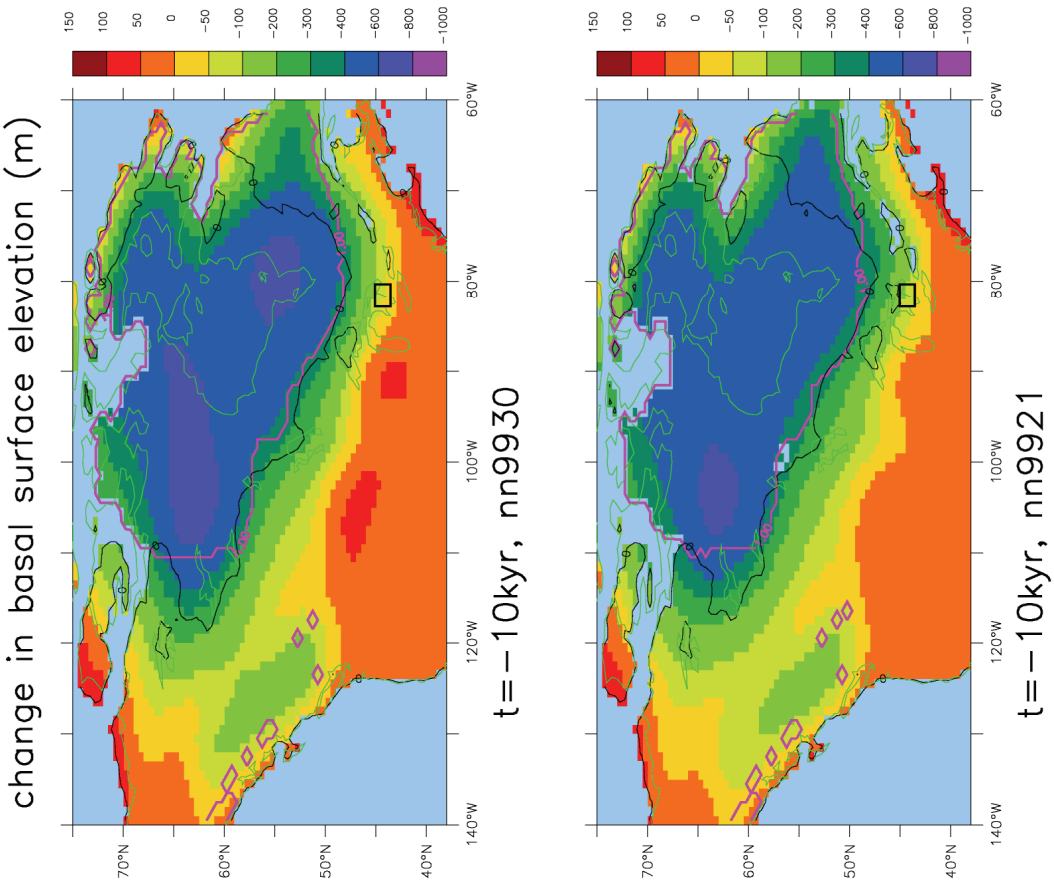
change in basal surface elevation (m)
150
100
50
0
−50
−100
−200
−300
−400
−600
−800
−1000
70°N
60°N
50°N
40°N
140°W
120°W
100°W
80°W
60°W
t=−10kyr, nn9930
t=−10kyr, nn9921

Appendix B. CD Archive of Time Series